DEVELOPMENT OF MICRO-PATTERN GAS DETECTOR FOR PHYSICS AND OTHER APPLICATIONS

By

Arnab Banerjee

Enrollment No. PHYS04200904006

Variable Energy Cyclotron Centre, Kolkata

A Thesis submitted to

The Board of Studies in Physical Sciences

In partial fulfillment of requirements for the Degree of

DOCTOR OF PHILOSOPHY

of

HOMI BHABHA NATIONAL INSTITUTE

December,2015

Homi Bhabha National Institute[1]

Recommendations of the Viva Voce Board

As members of the Viva Voce Board, we certify that we have read the dissertation prepared by Arnab Banerjee entitled "Development of micro-pattern gas detector for Physics and other applications" and recommend that it may be accepted as fulfilling the thesis requirement for the of Degree of Doctor of Philosophy.

Alok Chakrabarti

Chairman – Dr. Alok Chakrabarti　　　Date: 26.08.2016

Guide / Convener – Dr. Subhasis Chatopadhyay　　　Date: 26.08.2016

Examiner – Prof J. B. Singh　　　J.B. Singh　　　Date: 26.08.2016

Member 1- Dr. S. R. Banerjee　　　Date: 26.08.2016

Member 2- Prof. Satyajit Saha　　　Satyajit Saha　　　Date: 26.08.2016

Member 3- Dr. Sarbajit Pal　　　Sarbajit Pal.　　　Date: 26.08.2016

Final approval and acceptance of this thesis is contingent upon the candidate's submission of the final copies of the thesis to HBNI.

I hereby certify that I have read this thesis prepared under my direction and recommend that it may be accepted as fulfilling the thesis requirement.

Date: 26.08.2016

Place: VECC, Kolkata.

Guide

---

1 This page is to be included only for final submission after successful completion of viva voce.

STATEMENT BY AUTHOR

This dissertation has been submitted in partial fulfillment of requirements for an advanced degree at Homi Bhabha National Institute (HBNI) and is deposited in the Library to be made available to borrowers under rules of the HBNI.

Brief quotations from this dissertation are allowable without special permission, provided that accurate acknowledgement of source is made. Requests for permission for extended quotation from or reproduction of this manuscript in whole or in part may be granted by the Competent Authority of HBNI when in his or her judgment the proposed use of the material is in the interests of scholarship. In all other instances, however, permission must be obtained from the author.

Arnab Banerjee

ARNAB BANERJEE

DECLARATION

I, hereby declare that the investigation presented in the thesis has been carried out by me. The work is original and has not been submitted earlier as a whole or in part for a degree / diploma at this or any other Institution / University.

Arnab Banerjee

ARNAB BANERJEE

Dedicated to

My Parents

List of Publications arising from the thesis

Journal

1. ***Development of Multi-gap Resistive Plate Chamber(MRPC) for medical imaging***

A. Banerjee, A.Roy, S.Biswas, S.Chattopadhyay, G.Das, S.Pal

Nuclear Instruments and Methods in Physics Research A 718 (2013) 138139

2. ***Measurement of electrical properties of electrode materials for the bakelite Resistive Plate Chambers***

K.K. Meghna, **A. Banerjee**, S. Biswasc, S. Bhattacharya, S. Bose, S. Chattopadhyay, G. Das, C. Marick, S. Sahab and Y.P. Viyogi

2012 JINST 7 P10003

3. ***Performance simulation of a MRPC-based PET imaging system***

A. Roy, **A. Banerjee**, S. Biswas, S. Chattopadhyay, G. Das and S. Saha

2014 JINST 9 C10030

Conferences

1. ***Development of multigap RPC***

A. Banerjee, A .M. Ghosh, S. Biswas, S. Bhattacharya, S. Bose, S. Chattopadhyay, M. R. Dutta Majumdar, S. Saha, and Y.P. Viyogi

Proceedings of the International Symposium on Nuclear Physics (2009) 662

Arnab Banerjee.

2. ***Development of glass multigap RPC for PET Imaging***

A. Banerjee, S. Biswas, S. Chattopadhyay, G. Das, M. R. Dutta Majumdar, and Y. P. Viyogi

Proceedings of DAE Symposium on Nuclear Physics (2010) 672

3. ***Detection of Gamma rays with Multigap Resistive Plate Chamber***

A. Roy, **A. Banerjee**, S. Biswas, S. Chattopadhyay, G. Das, and S. Saha

Proceedings of the DAE Symp. on Nucl. Phys. 59 (2014) 946

Other

Publication as a co-author in the STAR collaboration:

Calibration and performance of the STAR Muon Telescope Detector using cosmic rays

C. Yang, et. al.

Nuclear Instruments and Methods in Physics Research A 762 (2014) 16

Arnab Banerjee

ACKNOWLEDGEMENTS

Exploration of this thesis entitled ‘Development of Micro-pattern Gas detectors for Physics and Other Applications’ was commenced from September, 2009 under the supervision of Dr. Subhashis Chattopadhyay. A brief description of the nature of the work has been outlined in the synopsis section.

First of all I would like to utter my profound gratitude to my valued teacher and proficient guide, **Dr. Subhashis Chattopadhyay**, without whose active help, ample support and apt guidance, it would not have been possible for me to achieve this work. Dr. Chattopadhyay was there at all times supporting me. I feel contented to have him for his constructive and priceless suggestions, active teamwork and unvarying back-up all the way through the exploration.

I am also gratified to **Prof. Satyajit Saha**, Saha Institute of Nuclear Physics, Kolkata for his valuable suggestions during the completion of this work. Without his support and guidance the work could not be performed at all. Also I want to thank Prof. Saha for allowing me to utilize the valuable resources and instruments of the department.

I am very much indebted to **Dr. Saikat Biswas** without whose help the work could not be completed. I want to thank him for his constant support and valuable suggestions. He constantly motivated me to learn the different procedures and development needed for completion of this thesis work.

I would like to thank **Mr. Ganesh Das** of VECC to help me in almost all of my work during this period. I am thankful to him for constant inspiration for developing hardwares and fabrications of all the detector modules needed for testing as a part of this thesis work.

I am also thankful to **Dr. Y. P. Viyogi**, former Head of Experimental High Energy Physics and Application Group, VECC for his encouragement, support and constant motivation in this develomental work and also for providing his precious time for purchasing different equipments needed to complete this thesis.

I am grateful to **Dr. Tapan Nayek** and **Dr. Bedanga Mohanty** for their help and valuable discussions at different stages during my stay at VECC.

I am also thankful to **Dr. Tapasi Ghosh** for her valuable suggestions regarding simulation works. Without her help regarding HEED and GARFIELD simulation it is impossible to complete this thesis work.

I want to give regards to **Dr. S. Ramanarayana** and **Mr. Kaushik Banerjee** of VECC for providing some electronics modules in due course of this thesis work and also for providing suggestions regarding different electronics related issues during this thesis period.

I would also like to aknowledge my junior **Mr. Arindam Roy** for his support and valuable discussions during this period. I was very much benifited from Mr. Roy for different suggestions regarding modules tesing as well as simulation work. I also want to thank him not only for his support in professional ground but also for constant mental support and other helps in time to time.

I am thankful to VECC workshop and VECC HEP workshop for making different components of detectors and related equipments. In this regard I want to thank **Mr. Tushar Das**, **Mr. Jatant Kumar**, **Mr. Nabarun Chowdhury**, **Mr. Santu Karmakar**, **Mr. Dipankar Bapari**, **Mr. Sukumar Mondal**, **Mr. Khokan Mondal**, **Mr. Tirthankar Paik**, **Mr. Anjan Naskar**, **Mr. Amit Mondal**, **Mr. Kamal Mondal**, **Mr. Prince Jana**, **Mr. Sanat Mondal**, **Mr. Bhaskar Mondal**, **Mr. Kamal Mondal Jr.** of PMD laboratory of VECC, **Ms. Nilima Mondal** for their help time to time.

I want to thank my fellow researchers Dr. Somenath De, Dr. Nihar Ranjan Sahoo, Dr. Younus, Dr. Sudipan De and Dr. Manish Gohil for their constant support and providing different valuable suggestions during this period.

I want to thank many of my senior research scholars like Rupa-di, Mriganka-da, Sidharth-da, Prasun-da, Amlan-da and also my juniors Sumit, Rajesh, Subikash for their support and help in different stages of this thesis work.

I would like to thank Dr. Partha Pratim Bhaduri, Dr. Prithwish Tribedy, Dr. Sanjib Muhuri and many others for their voluntary help and cooperation. I have learnt a lot from them both academic and otherwise.

I am grateful to different members of VECC such as Mr. Sujit De of Director's office, Mr. S.B. Bose, Mr. K. Gopalakrishnan, Mr. Debjit Gupta, Mr. Arup Bandopadhyay, Mr. Sujit Saha, Mr. Jayanta Kr. Sur of adminstration Mr. S. Sambath, Mr. Pradip Pramanick, Mr. S.K. Majumdar, Mr. Ashis Kr. Biswas, Mr. Asish Kr. Dey, Mr. Novel Chandra Yadav of accounts, Mr. T.K. Mahapatra, Mr. Arnab Das of computer section for their help.

For financial support during the execution of the works I am grateful to the Department of Atomic Energy, India for providing me fellowship and other financial support for the completion of this thesis.

I am also thankful to Dr. D. K. Srivastava, Director, VECC for their continuous support to continue my work.

I must mention here the name of **Dr. Nirmalya Sankar Das** of Jadavpur University. He is not just a friend of mine, but in one word I should say he is like a mentor to me in all respect. I am debtful for his friendship and his continuous support in every aspect. Also I am thankful to him and the Department of Nano Science and Technology, Jadavpur University for helping in material study which is a small part of this thesis work.

Among others I must mention the names of Dr. Arunava Jha, Mr. Debmalya Dey, Mrs. Rakhi Majumdar Dey, Mr. Anirban Gandhi, Mrs. Bipasa Gandhi, Mrs. Smita Ash, Mr. and Mrs. Ayon Bose, Mr. Subhajyoti Das, Mr. Utsab Dey, Mr. Sumit Mondal, Mr. Subhadeep Mondal for their continuous support and inspiration to complete the thesis work.

I would also like to thank **Mrs. Sukanya Banerjee**, my beloved wife for her mental support in last few months.

Last of all, my thanks must go to all my well-wishers, friends and teachers, whom I shall always keep in mind to remember throughout my life.

To conclude, I dedicate tis thesis to the honor of my beloved parents.

SYNOPSIS

High resolution gaseous detectors are being used in high energy physics experiments for the measurement of position and time of the particles produced in high energy collisions. Dedicated R&Ds have been performed to develop large area detectors giving very good position and timing resolution. Notable experiments of such gaseous detectors are RPC at CMS,ALICE experiments, GEM at CMS experiments among others. Capability of handling high particle rate and of large acceptance make these detectors suitable candidates in the field of medical imaging. In this thesis, work has been performed on the development and testing of a specialized gaseous detector called Multi-Gap Resistive Plate Chamber (MRPC) that has found appropriate candidate on a high energy physics physics experiment, Solenoidal Tracker At RHIC (STAR), Brookhaven National Laboratory, USA and as a prototype candidate for Time of Flight (TOF) Positron Emission Tomography (PET).

In high-energy heavy ion collision experiments, leptons are believed to be one of the most reliable probes for studying the creation of a deconfined state of stongly interacting matter called Quark Gluon Plasma (QGP). The STAR experiment taking data at Relativistic Heavy Ion Collider (RHIC) does not have any provision to detect di-muons, the decay product of charmonia. As an upgrade of STAR, the Muon Telescope Detector (MTD) has been built using a set of Multi-gap Resistive Plate Chambers (MRPCs). Detailed simulations have been performed to arrive at the design parameters of MTD. The MTD has been taking data since 2012. MRPCs built with glass as electrodes showed required performance for MTD at STAR when tested with cosmic rays.

Apart from the high energy physics aspect, the MRPCs can be a good substitute as a detector in the field of nuclear medicine, specially in PET. In PET imaging system, two back-to-back 511 keV photons originating from e^+e^- are detected. In conventional PET scanners scintillators are used for the detection of photon pairs and the process of detecting scintillation light using

Photo-Multiplier Tube (PMT) and associated electronics result in a large dead time. These systems, due to large dead times can only handle low rate applications, requiring large dose for obtaining good quality image. In addition to that, the scanners suffer from the limitations of a short Field of View (FOV) because of the small size of the scintillating crystals. Moreover, it is till now a big challenge to make a large size scintillator detector because of the unavailability of the crystal and the cost needed for such a system. MRPCs, on the other hand, can be built in large size and with its layered structure can interact with the gamma rays and can be made efficient for detecting photon pairs in PET imaging system. Also very good timing resolution of MRPCs enables it for the precise measurement of the location of annihilation by the measurement of the time of flight of the photon pairs, making it a suitable less expensive candidate for TOF-PET.

The development of MRPCs for the use in STAR-MTD and as a proof of principle for their use in TOF-PET imaging has been discussed in this thesis. The brief description is demonstrated as follows -

Development of MRPCs as the STAR-MTD detector module

The Muon Telescope Detector (MTD) at mid-rapidity in STAR experiment plays an important role in for developing our knowledge of QGP formation and its properties. Since muons do not participate in strong interactions, they provide penetrating probes for the strongly interacting QGP. A large area detector identifying muons with momentum of a few GeV/c at mid-rapidity allows the detection of di-muon pairs from QGP as thermal radiation, from the decay of quarkonia, of light vector mesons, and possible correlations of quarks and gluons as resonances in the QGP. Also, electron-muon correlations can be used to distinguish between lepton pair production and heavy quark decays ($c+\bar{c} \rightarrow e+\mu(e), B \rightarrow e(\mu)+c \rightarrow e+\mu(e)$). In addition muons are less affected by Bremsstrahlung radiation energy loss in the detector material than electrons, thus providing excellent mass resolution of vector mesons and quarkonia.

The MRPC module, as a detector for MTD, consists of five 250 μm gaps, which are defined by a stack of float glass plates separated by nylon fishing lines. The inner and outer glass plates are of 0.7 mm and 1.1 mm thickness respectively. The volume resistivity of the glass plates has been measured to be about $10^{12} \sim 10^{13}\Omega$cm satisfying the condition for use in MRPC as electrodes. The high voltages are applied on cathode and anode made of coating of colloidal graphite paint on the external surface of the outer glass plates. The graphite painted electrode has a surface resistivity of the order of 5 M$\Omega/\square$. High voltage is applied to the electrodes via a 10 mm wide and 800 mm long pieces of copper tape pasted to the long edges of the painted electrodes. The active area of the module is 52 cm$\times$ 90 cm. Twelve pairs of strips each of 3.8 cm wide and 90 cm long with 0.6 cm intervals between the strips etched on printed circuit boards (PCBs) above and below the inner glass stack pick up the signals. Mylar sheets of 0.18 mm thickness are placed between the graphite paint and the printed circuit boards with the read-out strips to electrically insulate the HV electrodes and the read-out strips. Fiberglass-reinforced honeycomb plates are used on the top and bottom surfaces to keep the device rigid.

MTD use 120 MRPC modules to cover the full acceptance. The details of the fabrication procedure of a number of modules at VECC has been discussed in the thesis. After the fabrication and thorough testing, all the modules were sent to UT, Austin for further study before the installation in STAR. All the modules were tested thoroughly at UT, Austin and were reported to work in good condition at STAR. Also the detector modules had been tested with cosmic ray after installation in STAR. The results are also part of the thesis work.

Fabrication of MRPCs for PET imaging

For several years different scientific groups across the world have been trying to build MRPC-based PET imaging systems with a varying number of gaps. The conversion efficiency up to 20-25% has been obtained by optimization study using the combined layers of lead as converters and glass as MRPC electrodes. In the thesis the process of optimization of MRPC as a suitable TOF-PET detector has been discussed. A two-staged simulation is performed to optimize the set-up. At first, GEANT4 has been used to simulate the conversion of the incident photons and secondly the electrons obtained by photon conversion are considered to be the particles ionizing the gas. The processes from ionization to signal generation have been implemented as another Monte Carlo (MC) process, as the final step.

A prototype set-up of MRPC-based PET imaging system has been built at VECC and tested with photon pairs emitting from ^{22}Na source. The efficiency of the detection of photon pairs have been studied using a combination of a scintillator and a MRPC module. The location of the source has been varied to study the sensitivity of the set-up for measurement of the location of the source by TOF method.

The experiments performed on the set-up can mainly be divided into two categories - the performance of bakelite-based MRPC and the performance of glass-based MRPC. The details procedure of the fabrication, development, tests under different conditions and the results obtained has been thoroughly discussed in the thesis.

Contents

SYNOPSIS xi

List of Figures **xxii**

List of Tables **xxiii**

1 Detectors for experimental high energy physics **1**

1.1 Introduction 1

1.2 Development of detectors for high energy physics experiments 3

1.3 Photon Detectors 5

1.3.1 Vacuum Photo-Detectors 6

1.3.1.1 Photomultiplier Tubes 7

1.3.1.2 Microchannel Plates 7

1.3.1.3 Hybrid Photon Detectors 8

1.3.2 Gaseous Photon Detectors 8

1.3.3 Solid-state photon detectors 8

1.4 Organic scintillators 9

1.5 Inorganic scintillators 10

1.6 Gas Filled Radiation Detectors : Basic Working Principle 11

1.7 Geiger-Müller Counter 16

1.8 Proportional Gas Detectors 16

1.9 MWPC 18

1.10 TPC 20

1.11 GEM 21

1.12 Resistive Plate Chambers 23
1.13 Semiconductor Detectors 26
1.14 Summary 26

2 MRPC and its applicaions 27

2.1 Introduction 27
2.2 Wide gap RPC 28
2.3 Multi-gap Resistive Plate Chamber (MRPC) 28
2.4 Dependence of voltage with gap size 32
2.5 Dependence of temperature and pressure 32
2.6 Application of MRPC 32
2.6.1 MRPC in LHCb Muon System 33
2.6.2 The TOF detector in ALICE experiment 34
2.6.3 TOF detector in CBM expeiment 35
2.6.4 MRPC as a Neutron Detector in NeuLAND Experiment 37
2.7 Summary 39

3 MRPC as a Medical Imaging Detector 40

3.1 Introduction 40
3.2 Nuclear Medicine 41
3.3 Positron Emission Tomography 41
3.4 MRPC as TOF-PET Detector 43
3.4.1 Simulation Procedure 44
3.4.1.1 Conversion procedure of 511 keV gamma within the MRPC detector 44
3.4.1.2 Monte Carlo study for response of MRPC 45
3.4.2 Simulation Results 48
3.4.2.1 Photon conversion efficiency 48
3.4.2.2 MRPC time response 49
3.4.2.3 Estimation of position resolution for an extended source of photon pairs 51

3.5 Fabrication of the detector modules . . . 52
3.5.1 Bakelite-based MRPC . . . 52
3.5.1.1 Two-Gap MRPC : Construction . . . 53
3.5.1.2 Four-Gap MRPC : Construction . . . 54
3.5.2 Glass-based MRPC . . . 54
3.6 Testing of the detector modules . . . 57
3.6.1 Bakelite based MRPC . . . 59
3.6.1.1 Two-Gap MRPC . . . 59
3.6.1.2 Four-Gap MRPC . . . 62
3.6.2 Glass based MRPC . . . 65
3.6.2.1 Six gap MRPC . . . 65
3.6.3 A feasibility study of the glass-based six-gap MRPC as a probable detector for PET imaging . . . 67
3.7 Summary . . . 71

4 Application in High Energy Physics: STAR Muon Telescope Detector (MTD) 73
4.1 Heavy Ion Collision . . . 73
4.2 Quark Gluon Plasma(QGP) . . . 74
4.3 STAR Detector . . . 76
4.3.1 Time Projection Chamber . . . 76
4.3.2 Time of Flight Detector . . . 77
4.3.3 Electromagnetic Calorimeter . . . 77
4.3.4 Photon Multiplicity Detector . . . 77
4.4 Muon Telescope Detector(MTD) . . . 78
4.4.1 Physical Processes . . . 81
4.4.1.1 Quarkonium Dissociation at high p_T . . . 81
4.4.1.2 Dissociation of Υ states . . . 83
4.4.1.3 Physics aspects with full coverage of MTD . . . 83
4.4.2 Detector Configuration . . . 85

4.4.3 Module Structure 86
4.4.4 Construction and Testing of the module 88
4.5 Performance of MRPC in Cosmic Ray Test setup 94
4.6 Summary 97

5 Summary **99**

List of Figures

1.1 Classification of radiation detectors 4
1.2 Photograph of Wilson Chamber 5
1.3 Basic working principle of gas detector 12
1.4 Diffusion of electrons through gas without electric field 13
1.5 Variation of drift velocity in different gases 14
1.6 Formation of an avalanche 15
1.7 Variation of number of pair as a function of high voltage 15
1.8 Schematic of proportional gas detector 17
1.9 Avalanche formation in proportional gas detector 17
1.10 Scematic of multi-wire proportional chamber 19
1.11 Spilt Field Magnet Detector at CERN 19
1.12 Schematic of Time Projection Chamber 20
1.13 Cross-sectional view of GEM detector 22
1.14 Electric field lines through GEM 22
1.15 Schematic of Resistive Plate Chamber 24

2.1 Schematic of working principle of MRPC 29
2.2 Equi-potential surfaces of MRPC 31
2.3 Schematic of the MRPC in LHCb experiment 33
2.4 Schematic of the MRPC in ALICE experiment 35
2.5 Schematic of the MRPC in CBM experiment 36
2.6 Beam test set-up of the MRPC in CBM experiment 36
2.7 Experimental set-up of the MRPC in NeuLAND experiment 37

2.8 Schematic of the MRPC prototype in NeuLAND experiment 38

3.1 Schematic diagram of the detector configuration for simulation 44
3.2 Variation of Townsend and attachment coefficient with the electric field 46
3.3 Variation of drift velocity with the electric field 46
3.4 Variation of conversion efficiency with number of layers for different converter thickness 49
3.5 Variation of conversion efficiency with number of layers for different material . . 50
3.6 Time response of single MRPC detector 50
3.7 Pair time resolution of back-to-back MRPC detectors 51
3.8 Position estimation for a MRPC detectors 52
3.9 (Left:) Two-gap bakelite-based MRPC (Right:) Heat treatment to the detector after Silicone coating 54
3.10 Construction of two-gap MRPC 54
3.11 Construction of Four-gap Bakelite-based MRPC 55
3.12 Construction of a six-gap glass based MRPC 55
3.13 A schematic representation of the construction procedure of the detector modules 56
3.14 Schematic diagram of trigger used for Cosmic ray testing 57
3.15 An electrical equivalent circuit for RPC 59
3.16 For two-gap MRPC (a) Current versus High Voltage (b) Efficiency versus High Voltage 60
3.17 For two-gap MRPC (a) Count Rate High Voltage (b) Time spectrum of the detector 61
3.18 Time resolution (FWHM) and time delay versus High Voltage for two-gap MRPC 62
3.19 Signal from the Four-gap Bakelite-based MRPC($\sim$50 mV after using threshold) 62
3.20 For four-gap MRPC (a) Current vs. HV (b) Efficiency vs. HV 63
3.21 For four-gap MRPC (a) Count rate vs. HV (b) Histogram for time difference . . 63
3.22 FWHM and time delay as a function of high voltage for four-gap MRPC 64
3.23 Variation of leakage current as a function of High Voltage for six-gap MRPC . . 65
3.24 Variation of (a) counting rate and (b) efficiency as a function of threshold for six-gap MRPC 66

3.25 (a) Charge spectrum (b) Variation of charge as a function of High Voltage for six-gap MRPC 66

3.26 Time distribution as obtained for six gap glass MRPC 67

3.27 For six-gap MRPC (a) Time resolution vs. high voltage (b) Time delay vs. high voltage 68

3.28 Experimental set-up for annihilating photon pair detection efficiency 69

3.29 Coincidence count rate vs. high voltage 69

3.30 Efficiency rate vs. high voltage 70

3.31 Time difference spectrum as obtained by shifting the source positions ; (a) source at 34.5 cm, (b) source at 37.4 cm, (c) source at 41 cm, (d) source at 41.5 cm . . 71

3.32 Time difference as a function of source distance 72

4.1 Schematic of heavy ion collision, a figure by S. Bass 73

4.2 Proposed schematic of the QCD phase diagram, left figure shows theoretical predictions and right figure shows the trajectories of heavy ion collisions. 75

4.3 Schematic view of the STAR detector. 76

4.4 A full HIJING central Au+Au collisions simulated in STAR 79

4.5 The efficiency for muons (top panel) and misidentification probabilities of pions, kaons, and protons (bottom panel) at $|y| < 0.5$ 80

4.6 The arrangement of MTD trays on the outside of STAR 81

4.7 J/ψ R_{AA} vs. p_T. 82

4.8 The J/ψ efficiency as a function of p_T. 84

4.9 The simulated invariant mass of $\mu^+\mu^-$ distribution from j/ψ and background in d+Au collisions (top panel); the invariant mass distribution of dimuon decayed from Υ at 0< p_T <5 GeV/c (bottom panel). 85

4.10 A beam's eye view of STAR. The MTD system is attached to the PMT HV boxes. 86

4.11 Schematic of the detector module 87

4.12 Fabrication procedures of MTD MRPC detector modules 88

4.13 Left panel: the photograph of the pick-up strips for the MTD modules; Right panel: the phtograph of the fishing lines used to maintain the constant gas gap of the modules 89

4.14 Cross-sectional view of a typical MTD MRPC detector module showing the gas gaps maintained by the fishing lines 89

4.15 Completely assembled MTD module before the gas flow 90

4.16 Left panel: The gas connection applied to the MTD molecules; Right panel: the MFC-based gas mixing system 91

4.17 Schematic layout of the cosmic ray test setup of the MTD modules 92

4.18 A typical test result of one of the MTD modules : Left panel - the noise rate for different pick-up channels; right panel - time over threshold plot used for slewing correction 93

4.19 Correlation plot of diffrent pick-up strips as obtained for one of the MTD modules 94

4.20 Schematic view of the cosmic test setup in STAR 95

4.21 Left: The momentum distribution of cosmic ray muons for $p_T > 2$ GeV; Right: The relative momentum resolution distribution of the two tracks from one cosmic ray muon 96

4.22 ΔZ and $\Delta\phi$ resolution for the TPC reconstructed tracks 96

4.23 Time resolution for the TPC reconstructed tracks by MTD detectors 97

List of Tables

2.1 MRPC as a particle detector in different high energy experiments 39

3.1 Different Scanners used in Medical Imaging 42
3.2 A comparative study of the different design parameters of the detector modules 57
3.3 Different electronics components used for the testing of the detectors 58

4.1 Quarkonium dissociation temperatures 83
4.2 Summary of the layout of a module 87
4.3 High Voltage and threshold configuration for cosmic test 92

Chapter 1

Detectors for experimental high energy physics

1.1 Introduction

High-energy physics is a way to study of the smallest components of matter and how they interact. In studying these particles, which actually create the whole world, high-energy physics is a tool to learn what our world is made of, how it is put together, and how it works.

Eventually, study of this inner space of our material world also reveal much about outer space. Approximately 15 billion years ago, right after the Big Bang, our universe was a chaotic, undifferentiated mix of fundamental particles. Galaxies, stars, planets - all emerged from these primary ingredients. When high-energy physicists create fundamental particles in the laboratory, they actually try to replicate the conditions that existed billions of years ago in order to study how our universe began, how it has evolved, and even how it might end.

Finding out what matter is made of is not an easy task. The only way to disassemble matter is to hurl one particle into another and to examine the mangled fragments. The only way it can be done is by propelling the particles at high speeds and high energies and slammed them into one another to break them apart and sometimes to create new ones via the instrument called 'particle accelerators'. The higher the energy, the deeper it is possible to probe into natures smallest constituents.

Through such experiments, high-energy physicists have pieced together a theory of the basic structure of matter and its forces. According to this theory, called the **Standard Model**, the tremendous complexity of our world is built up from a remarkably small number of elementary particles. The experiments revealed that the atom itself is made of electrons and a nucleus containing protons and neutrons - and that protons and neutrons themselves break down into fundamental particles called quarks. According to the Standard Model, all matter is composed of two categories of elementary particles: quarks and leptons, six kinds of each. These particles of matter interact through four fundamental forces of nature : gravity, electromagnetism, the strong force (which holds together the nucleus), and the weak force (which governs certain kinds of radioactive decay). These forces are also composed of particles, called gauge bosons. One of these, the photon, transmits electromagnetism. The W and Z particles carry the weak force. The gluon is responsible for the strong force. The graviton is presumed to carry gravity, but this particle has not yet been found and is not incorporated into the current theory.

In the field of high-energy physics experimental data, along with strong theoretical work, all suggest a new insight that will take the modern concepts well beyond today's Standard Model.

To study the fundamental particles of the physical world, high-energy physics is dependent on two sources: nature itself, and the laboratory. Many experiments study naturally occurring particles, such as cosmic rays, a steady rain of high-energy particles originating in outer space, or neutrinos produced in nuclear reactions in the Sun. e.g., the Super-Kamiokande experiment in Japan or INO experiment in INDIA.

The high-energy accelerators, on the other hand, direct opposing beams of charged particles into head-on collisions to produce the desired fundamental particles. Powerful electrical fields inject energy into the beams, accelerating them until they are traveling almost as fast as light. Magnetic fields, created by standard and superconducting magnets, steer the beams and keep them tightly focused. The only tool that is needed to observe the newly created particles, is the huge detectors with multiple layers of complex electronics.

In this chapter, mainly the uses of different types of detectors along with their properties that are used in modern scientific particle physics and high energy physics experiments will be discussed.

1.2 Development of detectors for high energy physics experiments

Any charged particle which can interact with matter always lose its energy, that can be seen as either

1. **Excitation**: After the interaction with the matter particles the charged particle can excite the atom or molecule to a higher energy level, which is capable of emission of low energy photons due to de-excitation.

2. **Ionization**: An electron is ejected from the material due to the interaction of the charged particle.

3. **Cherenkov or Transition radiation**: Instead of ionization or excitation, a real photon can be produced under certain conditions.

In experimental and applied particle physics, nuclear physics, and nuclear engineering, a particle detector, also known as a radiation detector, is a device used to detect, track, and/or identify high-energy particles, such as those produced by nuclear decay, cosmic radiation, or reactions in a particle accelerator. In short, the detectors are the main tool for a scientist to look into the subatomic world. The recent progress in accelerator technology and the availability of variety of beams of high energetic particles had led to several new demands on the detector systems. Several special types of radiation detectors are also needed in the application of nuclear techniques in other areas of science, technology and medicine. Modern detectors are also used as calorimeters to measure the energy of the detected radiation. They may also be used to measure other attributes such as momentum, spin, charge etc. of the particles.

In the following Figure 1.1 a broad classification of radiation detectors has been depicted.

The particle tracking detector, called Wilson Chamber, was developed in 1911 by Charles, where water is allowed to evaporate in an enclosed chamber to the point of saturation and then the pressure is lowered, which in turn produce an over-saturated volume of air within the chamber. Any passage of charged particle under this condition through this chamber condense

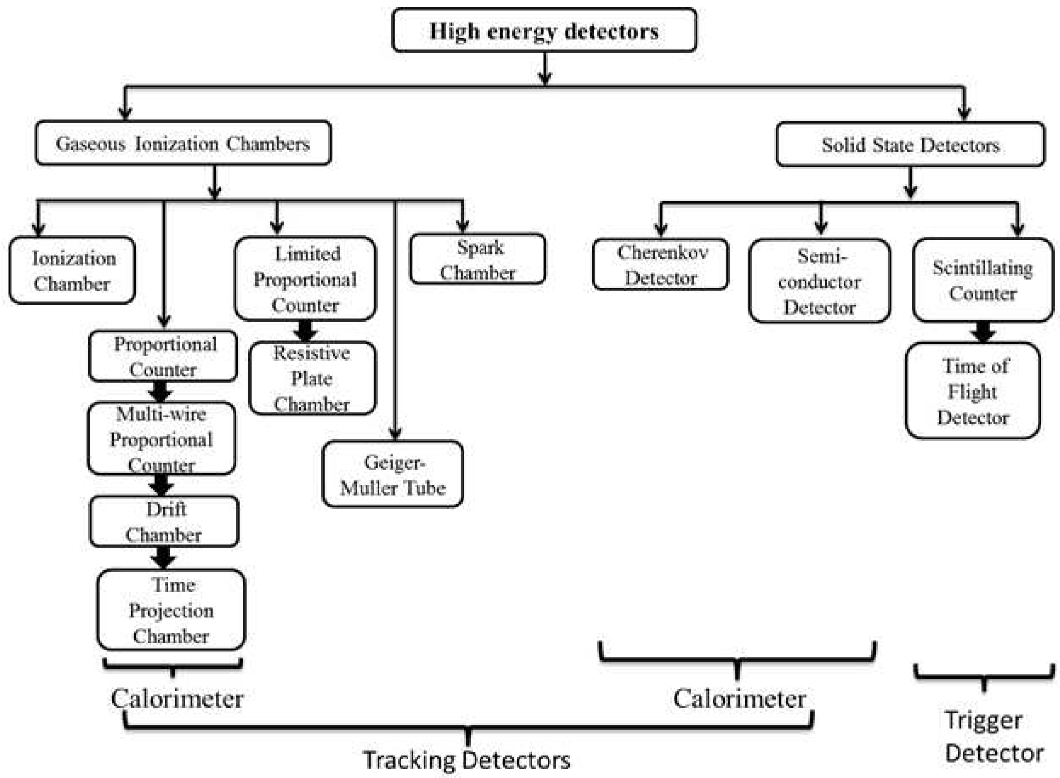

Figure 1.1: Classification of radiation detectors

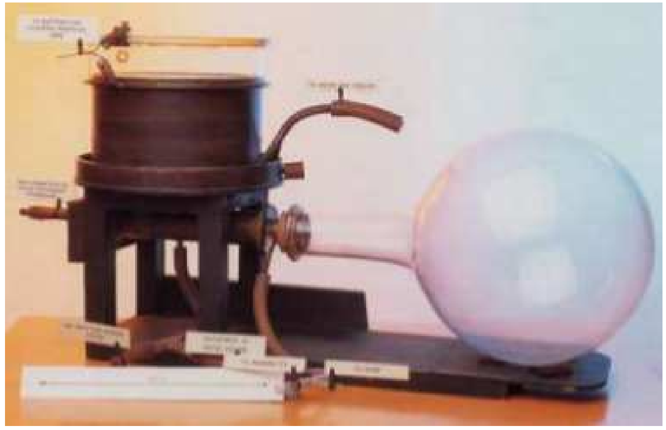

Figure 1.2: Photograph of Wilson Chamber

the vapour into tiny droplets, marking the particle's path. A schematic of such a detector can be seen in the Figure 1.2.

Another important particle tracking detector was discovered in 1952 by Donald Glaser, called the Bubble chamber. The principle of this detector is similar to Wilson Chamber, except instead of supersaturated vapour, liquid hydrogen is "superheated" and a charged particle passing through the medium leaves a trail of ions along its path and the "superheated" liquid forms gas bubbles around ions. The main advantage of this detector is that within this detector liquid hydrogen is used as both detector medium and target. Also the detector has very high tracking precision of 5 μm.

1.3 Photon Detectors

Many of the detectors in high-energy, nuclear, and astrophysics rely on the detection of photons in or near the visible range, 100 nm $\leq \lambda \leq$ 1000 nm, or energy of the order of a few eV.

Detection of photon is generally done by generating a detectable electrical signal proportional to very small number of incident photons. The process can be described in three distinct steps:

1. Generation of a primary photo-electron from an incident photon by the photoelectric or photo-conductive effect.

2. Amplification of the photo-electron signal to detectable levels by an avalanche process.

3. Collection of the secondary electrons to form the electrical signal.

The photo-detectors can be characterized by the following parameters -

a) Quantum Efficiency : the number of primary photoelectrons generated per incident photon

b) Collection Efficiency : the overall acceptance factor other than the generation of photoelectrons

c) Gain : the number of electrons collected for each photo-electron generated

d) Dark Current : the electrical signal when there is no photon

e) Dynamic Range : the maximum signal available from the detector

f) Rate Capability : the time needed, after the arrival of one photon, to get ready to receive the next.

Optimization of the factors are highly application-specific, which include the photon flux and wavelength range, the total area to be covered and the efficiency required, the volume available to accommodate the detectors, characteristics of the environment such as chemical composition, temperature, magnetic field, ambient background, as well as ambient radiation of different types and, mode of operation, high-voltage requirements, power consumption, calibration needs, aging, cost, and so on.

Depending upon the application, photo-detectors can be classified in three broad categories, viz., vacuum photo-detectors, gaseous photo-detectors, and solid-state photo-detectors. The salient features of the main technologies and the common variants are briefly described below.

1.3.1 Vacuum Photo-Detectors

Vacuum photo-detectors can be broadly subdivided into three types: photomultiplier tubes, micro-channel plates, and hybrid photo-detectors.

1.3.1.1 Photomultiplier Tubes

A versatile class of photon detectors, vacuum photomultiplier tubes (PMT) has been employed by a vast majority of all particle physics experiments [1]. The cathode material in PMT has a low work function. When a photon hits the cathode and liberates an electron, the latter is accelerated and guided by electric fields to impinge on a secondary- emission electrode, or dynode, which then emits a few (5) secondary electrons. The multiplication process is repeated typically 10 times in series to generate a sufficient number of electrons, which are collected at the anode for delivery to the external circuit. The total gain of a PMT depends on the applied high voltage V as G = AV^{kn} , where k $\sim$ 0.70.8, depending on the dynode material, n is the number of dynodes in the chain, and A a constant. Typically, G is in the range of 105 106 . Pulse rise times are usually in the few nanosecond range.

A large variety of PMTs covers a wide span of wavelength ranges from infrared (IR) to extreme ultraviolet (XUV) [2]. Fast PMTs with very high efficiency have been developed in recent years for detection of Cherenkov radiation in neutrino experiments such as Super-Kamiokande and KamLAND among many others.

1.3.1.2 Microchannel Plates

Microchannel plate (MCP) photo-detector consists of one or more $\sim$2 mm thick glass plates with densely packed cylindrical holes, or channels?, having diameter $\sim$ 10 μm sitting between the transmission-type photo-cathode and anode planes, separated by 1 mm gaps. Instead of discrete dynodes, the inner surface of each cylindrical tube serves as a continuous dynode for the entire cascade of multiplicative bombardments initiated by a photo-electron.

MCPs offer good spatial resolution, have excellent time resolution ($\sim$20 ps), and can tolerate random magnetic fields up to 0.1 T. However,they suffer from relatively long recovery time per channel and short lifetime. MCPs are widely employed as image-intensifiers, although not so much in HEP or astrophysics.

1.3.1.3 Hybrid Photon Detectors

Hybrid photon detectors (HPD) combine the sensitivity of a vacuum PMT with the excellent spatial and energy resolutions of a Si sensor [3]. A single photo-electron ejected from the photo-cathode is accelerated through a potential difference of 20 kV before it impinges on the silicon sensor. The gain nearly equals the maximum number of e-h pairs that could be created from the entire kinetic energy of the accelerated electron: $G = eV/w$, where e is the electronic charge, V is the applied potential difference, and $w = 3.7$ eV is the mean energy required to create an e-h pair in Si at room temperature.

Current applications of HPD's include the CMS hadronic calorimeter and RHIC detector in LHCb.

1.3.2 Gaseous Photon Detectors

In gaseous photomultipliers (GPM) a photo-electron in a suitable gas mixture initiates an avalanche in a high-field region, producing a large number of secondary impact-ionization electrons. In principle the charge multiplication and collection processes are identical to those employed in gaseous tracking detectors such as multi-wire proportional chambers, micro-mesh gaseous detectors (Micromegas), or gas electron multipliers (GEM).

The devices can be divided into two types depending on the photo-cathode material. One type uses solid photo-cathode materials much in the same way as PMTs. Since it is resistant to gas mixtures typically used in tracking chambers, CsI is a common choice. In the other type, photo-ionization occurs on suitable molecules vaporized and mixed in the drift volume.

Many of the ring imaging Cherenkov detectors to date have used GPMs for the detection of Cherenkov light [4].

1.3.3 Solid-state photon detectors

Compared to traditional vacuum- and gaseous photo-detectors, solid-state devices are more compact, tolerant to magnetic fields, and often cheaper. They are equipped with fine pixelization, which makes them ease to integrate into large systems, and can operate at low electric potentials, while satisfying the performance criteria. They are particularly well suited for detection of γ- and X-rays.

A typical solid-state photon detector, Silicon photodiodes (PD) are widely used in high-energy physics as particle detectors like CLEO, L3, Belle, BaBar,and GLAST and in a great number of applications as light detectors.

1.4 Organic scintillators

Organic scintillators are broadly classed into three types, crystalline, liquid, and plastic, all of which utilize the excitation produced by charged particles to generate optical photons, usually in the blue to green wavelength regions [5]. Plastic scintillators are the most widely used, liquid organic scintillator is finding increased use, and crystal organic scintillators are practically unused in high-energy physics. The resulting photo-electron signal in organic scintillators will depend on the collection and transport efficiency of the scintillator and the quantum efficiency of the photo-detector.

Although plastic scintillators are reliable, robust, and convenient, they possess certain disadvantages. Exposure to solvent vapors, high temperatures, mechanical flexing, irradiation, or rough handling will aggravate the process. A particularly fragile region is the surface which can develop micro-cracks which degrade its transmission of light by total internal reflection. This micro-cracks is particularly likely where oils, solvents, or fingerprints have contacted the surface of the scintillator.

Also irradiation of plastic scintillators creates color centers which absorb light more strongly in the UV and blue than at longer wavelengths. This effect appears as a reduction both of light yield and attenuation length. Radiation damage depends not only on the integrated dose, but on the dose rate, atmosphere, and temperature, before, during and after irradiation, as well as the materials properties.

1.5 Inorganic scintillators

Inorganic crystals form a class of scintillating materials with much higher densities than organic plastic scintillators (typically $\sim$ 48 g/cm^3) with a variety of different properties for use as scintillation detectors. Due to their high density and high effective atomic number, they can be used in applications where high stopping power or a high conversion efficiency for electrons or photons is required.

Some crystals are intrinsic scintillators in which the luminescence is produced by a part of the crystal lattice itself. However, other crystals require the addition of a dopant, typically fluorescent ions such as thallium (Tl) or cerium (Ce) which is responsible for producing the scintillation light. However, in both cases, the scintillation mechanism is the same. Energy is deposited in the crystal by ionization, either directly by charged particles, or by the conversion of photons into electrons or positrons which subsequently produce ionization. This energy is transferred to the luminescent centers which then radiate scintillation photons.

Some of the important inorganic scintillators that are most commonly used are Thallium-doped Sodium Iodide (NaI(Tl)), Bismuth gemanate ($Bi_4Ge_3O_{12}$ or BGO), Cerium doped lutetium oxyorthosilicate (Lu_2SiO_5:Ce, or LSO:Ce), Lead tungstate ($PbWO_4$ or PWO) etc. Aiming at the best jet-mass resolution inorganic scintillators are being investigated for HEP calorimeters with dual readout for both Cherenkov and scintillation light to be used at linear colliders. These materials may be used for an electromagnetic calorimeter [6] or a homogeneous hadronic calorimetry (HHCAL) detector concept, including both electromagnetic and hadronic parts [7].

Most of the inorganic crystals have been used in high energy or nuclear physics experiments when the ultimate energy resolution for electrons and photons is essential. Examples are the Crystal Ball NaI(Tl) calorimeter at SPEAR, the L3 BGO calorimeter at LEP, the CLEO CsI(Tl) calorimeter at CESR, the KTeV CsI calorimeter at the Tevatron, the BaBar, BELLE and BES II CsI(Tl) calorimeters at PEP-II, KEK and BEPC III. Because of its high density and relative low cost, PWO calorimeters are widely used by CMS and ALICE at LHC, by CLAS and PrimEx at CEBAF, and by PANDA at GSI.

1.6 Gas Filled Radiation Detectors : Basic Working Principle

Gas filled detectors were first discovered to detect the radiation [17]. Now a days gas filled detectors are robustly used in all the large high energy physics experiments (e.g. STAR, CMS, ATLAS, ALICE, OPERA, BaBar, Belle, BESIII).

Among the three states of matter,viz., solid, liquid and gas, it is very important to understand the usefulness of the gas to be used as a detector material. The main advantages of such type of detectors are as follows-

a) Gas filled detectors are relatively cheap and simple in terms of the fabrication and operation procedure.

b) There can be optimized gas mixtures possible for different types of uses, such as detection of charged particle in high energy and nuclear physics, X-rays in synchrotron physics and astronomy and neutrons in neutron scattering.

c) Electron transport properties are favourable and well characterized in gaseous medium.

d) Gas gain or electron multiplication factor can be achieved over large dynamic range.

e) Ionization collection through gaseous medium can form signals, that can be used for further information.

f) The detectors mostly do not suffer from the problems of radiation damage.

The basic operational principle of a typical gas detector can be depicted by the following Figure 1.3. When a charged particle passes through the gas within the detector, primary ionization occurs, which may be represented by the equation [18]

$$X + p \rightarrow X^{+} + p + e^{-}$$

where X represents gas atom, p charged particle passing through the gas, e^{-} delta-electrons produced in the gas. If the energy of the delta electrons are high enough, then they can lead to secondary ionization,represented by the equation

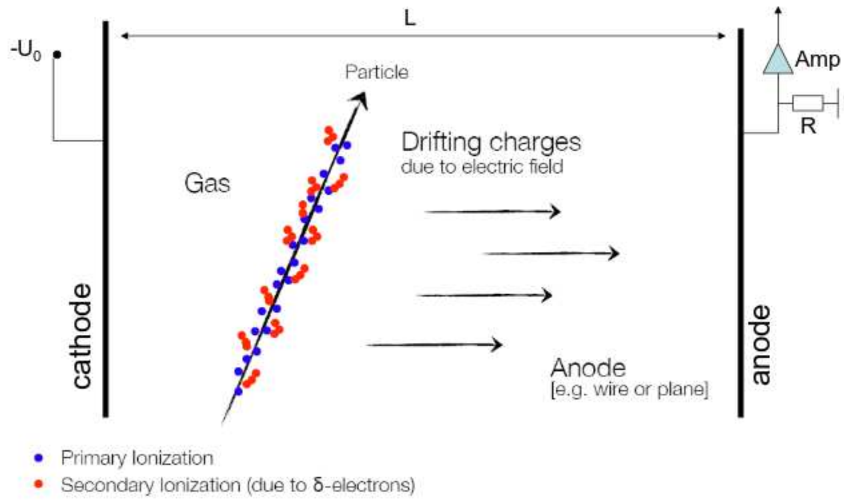

Figure 1.3: Basic working principle of gas detector

$$X + e^- \rightarrow X^+ + e^- + e^-$$

The relevant parameters controlling the process of ionization within the gas are the ionization energy E_i, average energy per ion pair W_i, average number of primary ion pairs n_p and average number of ion pairs produced due to secondary ionization n_s, where 'i' stands for the primary ionization parameters. The value of n_s follows the formula, 'L' being the gas gap,

$$\langle n_s \rangle = \frac{L(\langle \frac{dE}{dx} \rangle)_i}{W_i}$$

which is typically 2-6 times n_p.

Production of primary ion/electron pairs follows Poisson distribution

$$P(n_p, \langle n_p \rangle) = \frac{\langle n_p \rangle^n e^{-\langle n_p \rangle}}{n_p!}$$

with $\langle n_p \rangle = L/\lambda$ and $\lambda = 1/(n_e \sigma_I)$, L being the gas gap, n_e electron density and σ_I Ionization cross-section.

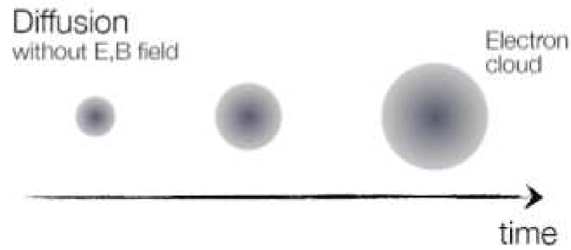

Figure 1.4: Diffusion of electrons through gas without electric field

The main features governing the behaviour of gas filled detectors are the mobility of charge carriers (ions and electrons), influencing the timing behaviour of the detector; the electron attachment and recombination power, influencing detector efficiency and mostly on gas multiplication ability.

Without the presence of any electric field the motion of electrons are mostly influenced by diffusion, as schematically shown by the Figure 1.4 and governed by the equation

$$\frac{dN}{dx} = \frac{N_0 exp(-\frac{x^2}{4Dt})}{\sqrt{4\pi Dt}}$$

where N_0 is the initial number of electrons present within the gas and D is diffusion coefficient, given by

$$D = \frac{1}{3} v\lambda$$

v and λ being mean velocity and mean free path respectively and given by

$$\lambda = \frac{1}{\sqrt{2}} \frac{kT}{\sigma_0 P}$$

$$and \quad v = \sqrt{\frac{8kT}{\pi m}}$$

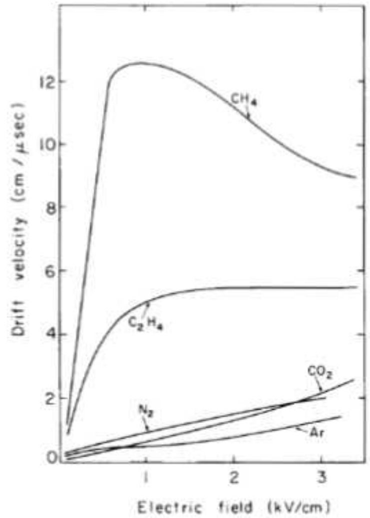

Figure 1.5: Variation of drift velocity in different gases

But the situation is different in presence of an electric field. With an external electric field the electrons/ions obtain a velocity, called 'drift velocity' in addition to thermal motion. On average the electrons/ions move along the electric field lines. The drift velocity is proportional to applied electric field intensity.

$$v_D = \mu_{\pm} E$$

where μ stands for the mobility and '+' and '-' signs indicate the ions and electrons respectively. In general the drift velocity for electrons is much higher ($\sim$ cm/μs) compared that of the ions ($\sim$ cm/ms). At thermal equilibrium the mobility follows Einstein's formula

$$\frac{D}{\mu} = \frac{kT}{e}$$

A typical variation of drift velocity under normal conditions in several gases is shown in Figure 1.5.

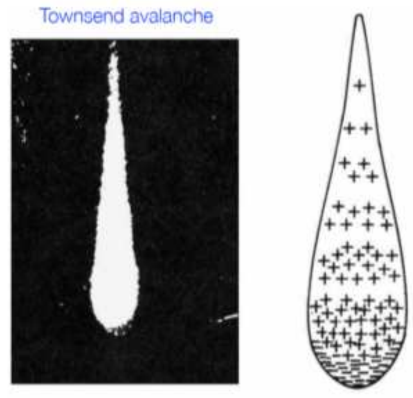

Figure 1.6: Formation of an avalanche

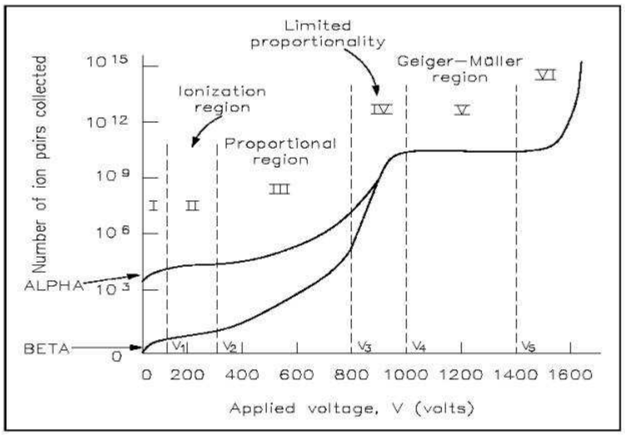

Figure 1.7: Variation of number of pair as a function of high voltage

A larger value of electric field yields a larger value of kinetic energy which in turn produce avalanche formation, where larger mobility of electrons results in liquid drop like avalanche with electrons near head, as shown in the Figure 1.6.

Also the function of a gas filled detector depends on the operating voltage. A schematic representation of the number of ion pair collected for a gas filled detector for varying high voltage is shown in Figure 1.7.

1.7 Geiger-M$\ddot{u}$ller Counter

The Geiger-M$\ddot{u}$ller counter or Geiger tubes is one of the oldest radiation detector types in existence. The Geiger-M$\ddot{u}$ller tube is filled with an inert gas such as helium, neon, or argon at low pressure, to which a high voltage is applied. The tube briefly conducts electrical charge when a particle or photon of incident radiation makes the gas conductive by ionization. The ionization is considerably amplified within the tube by the Townsend Discharge effect to produce an easily measured detection pulse, which is fed to the processing and display electronics. This large pulse from the tube makes the detector relatively cheap to manufacture, as the subsequent electronics is greatly simplified. The electronics also generates the high voltage, typically 400600 volts, that has to be applied to the Geiger-Mueller tube to enable its operation.

The detector is mainly used to detect alpha and beta particles, but beside that it is also enabled to detect radiations like X-ray, Gamma, neutron, etc. There are two main limitations of the Geiger counter. Because the output pulse from a Geiger-M$\ddot{u}$ller tube is always the same magnitude regardless of the energy of the incident radiation, the tube cannot differentiate between radiation types. A further limitation is the inability to measure high radiation rates due to the 'dead time' of the tube. This is an insensitive period after each ionization of the gas during which any further incident radiation will not result in a count, and the indicated rate is therefore lower than actual. Typically the dead time will reduce indicated count rates above about 10^4 to 10^5 counts per second depending on the characteristic of the tube being used.

1.8 Proportional Gas Detectors

A schematic of a proportional gas detector is shown in Figure 1.8. The thin axial anoide wire is supported at either end by insulators that provide a vaccum-tight electrical feedthrough for connection to the high volyage. The outer cathode is conventionally grounded. For low energetic radiation a thin entrance window is provided at some point along the cathode wall. In such a detector the gas multiplication is critically depends on the migration of electrons rather than much slower positive ions. The gas which is used in such deetctors is chosen such that they do not exhibit an appreciable electron attachment coefficienct. Gas multiplication in this detector is based on the secondary ionization created in collision between electrons and

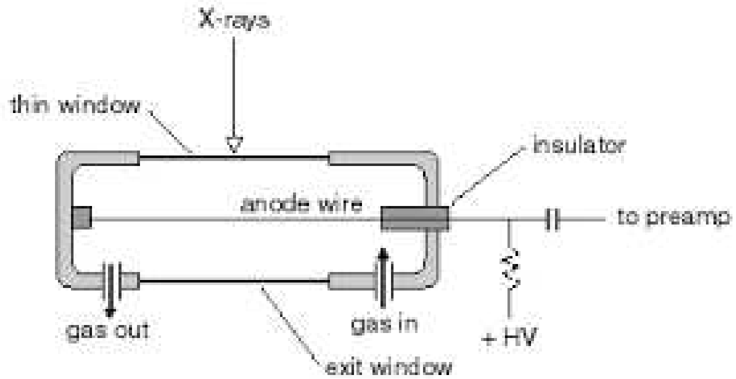

Figure 1.8: Schematic of proportional gas detector

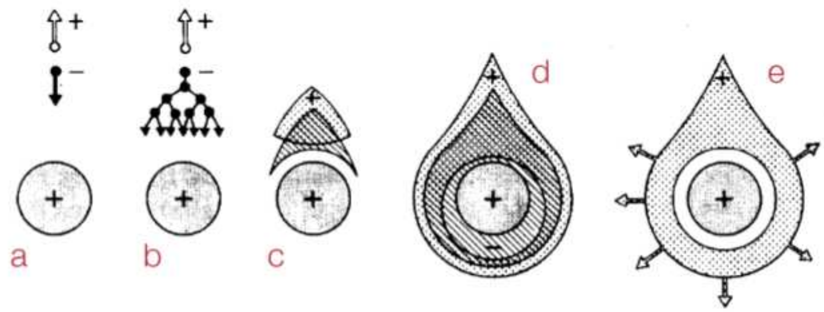

Figure 1.9: Avalanche formation in proportional gas detector

the gas within the detector. Also to avoid the photon-induced ionization within the detector arising due to the deexcitement of gas mocules, a special type of gas, called 'quench gas' is used.

The time development of an avalanche near the anode wire of a proportional gas detector can be depicted following Figure 1.9.

It can be summarized as follows-

a) a single primary electron proceeds towards the wire anode

b) in the region of increasingly high field the electron experiences ionizing collisions (avalanche multiplication)

c) electrons and ions are subject to lateral diffusion

d) a drop-like avalanche develops which surrounds the anode wire

e) the electrons are quickly collected (∼1ns) while the ions begin drifting towards the cathode generating the signal at the electrodes.

Among different proportional gas detectors that are used in high energy experiments Multi-Wire Proportional Counter (MWPC), Time Projection Chamber (TPC), parallel plate avalanche chamber (PPAC), Gas Electron Multiplier (GEM), micromegas etc are important.

1.9 MWPC

MWPC were first invented by Georges Charpak [22] in 1968. Figure 1.10 shows a sketch of the arrangement of the wires along with the configuration of the electric field caused by the wires. Due to the ionization of the gas the electrons are produced and due to an initial nearly uniform field the electrons drift towards the anode wires. After that they are accelerated to the nearest anode wire and due to a strong electric field avalanches are formed. Due to the formation of the avalanche a high negative polarity induced pulse is generated on the anode wire, while the neighbouring anode wires show smaller positive pulse.

The preamplifier connected to each wire thus be able to localize the event to the nearest wire. MWPC is mainly operated in proportional mode, because the low signal amplitude can be a limiting factor in position-sensing applications. Also the self-quenching streamer mode is applied sometimes because of the larger signal size that is produced [23, 24].

Figure 1.11 shows the picture of Spilt Field Magnet Detector (1972-1983), where for the first time 40 large area MWPCs were installed at CERN ISR.

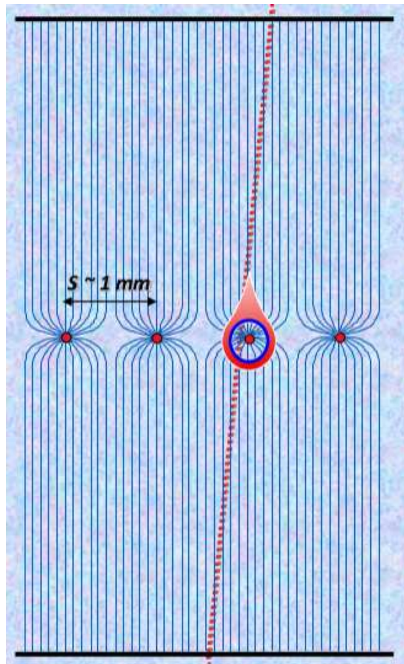

Figure 1.10: Scematic of multi-wire proportional chamber

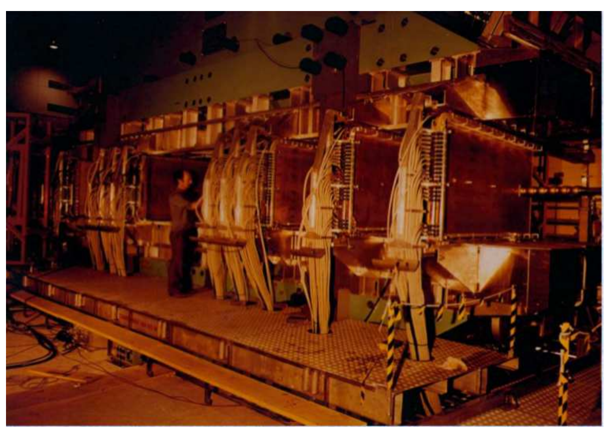

Figure 1.11: Spilt Field Magnet Detector at CERN

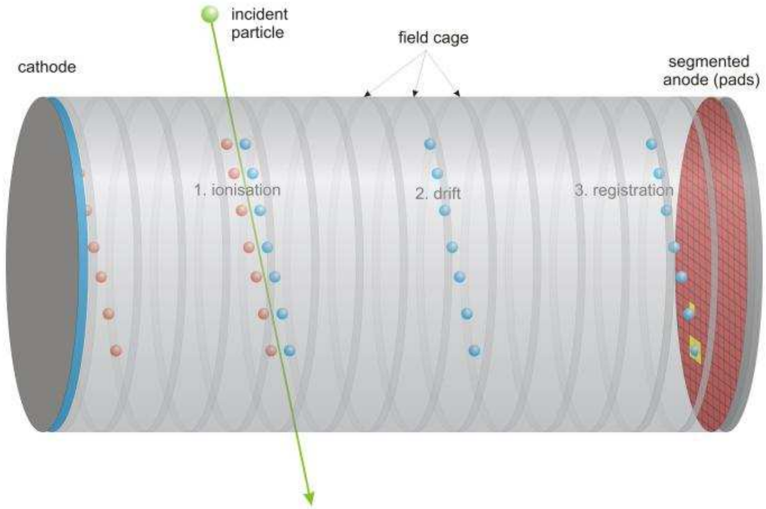

Figure 1.12: Schematic of Time Projection Chamber

1.10 TPC

The Time Projection Chamber has been introduced in 1976 by D.R. Nygren. It consists of a gas filled sensitive volume, usually with a central cathode that divides the volume into two identical halves. Each side has an anode with a readout system. The cathode is at a high potential that results in a field strength of some 100 V/cm while the anode is at ground potential.

In Figure 1.10 the basic working principle is demonstrated. A charged particle traversing the gas volume of the TPC will ionize the atoms of the gas mixture (usually around 90% noble gas and 10% quencher gas) along its trajectory (point 1 in Figure 1.10). A high electric field is applied between the endplates of the chamber. The released electrons drift in this field towards the anode (point 2 in Figure 1.10).To be able to measure the position of the particle trajectory as accurately as possible, the electric field has to be very homogeneous. This can be achieved by a field cage, which usually consists of conducting rings around the cylinder. These rings divide the potential from the cathode stepwise down to the anode. Additionally, a high magnetic field parallel to the electric field is used to "bend" the trajectory of the particle on a spiral track due to the Lorentz force. This gives the possibility to calculate the momentum of the particle from the knowledge of the curvature and the B-field.

At the anode plane, the electrons can be detected on the readout plane which is segmented in the directions perpendicular to the drift direction (point 3 in Figure 1.10). As the electron signal from the primary ionization process is only of the order of 100 electrons per centimeter, the signal needs to be amplified before being detectable. Traditionally this has been done within high electric field in vicinity of thin wires.

The rϕ position (coordinates perpendicular to the cylinder axis) of the trajectory can be reconstructed directly from the coordinates of its projection on the pad plane. The z position (coordinate along the cylinder axis) is reconstructed from the drift time (time between particle passing the TPC volume and measured signal on the pads). Therefore an external timing information, e.g. from a silicon detector, is needed.

1.11 GEM

GEMs were invented in 1997 in the Gas Detector Development Group at CERN by physicist Fabio Sauli [31].

Typical GEMs are constructed of 50-70 micrometre thick Kapton foil clad in copper on both sides. A photolithography and acid etching process makes 30-50 micrometer diameter holes through both copper layers; a second etching process extends these holes all the way through the kapton. The small holes can be made very regular and dimensionally stable. For operation, a voltage of 150-400 V is placed across the two copper layers, making large electric fields in the holes. Under these conditions, in the presence of appropriate gases, a single electron entering any hole will create an avalanche containing 100-1000 electrons; this is the 'gain' of the GEM. Since the electrons exit the back of the GEM, a second GEM placed after the first one will provide an additional stage of amplification. Many experiments use double- or triple-GEM stacks to achieve gains of one million or more.

In Figure 1.13, cross-section of a typical GEM detector has been shown. Also the variation of the electric field through the holes of the detector has been shown in Figure 1.14.

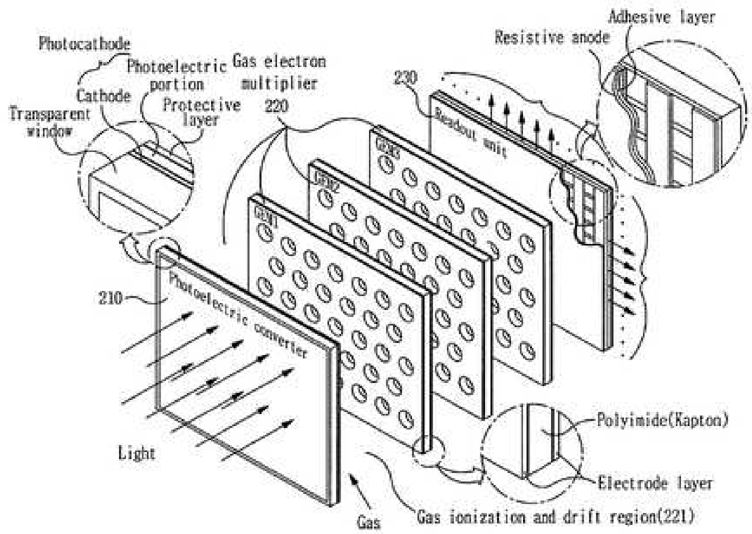

Figure 1.13: Cross-sectional view of GEM detector

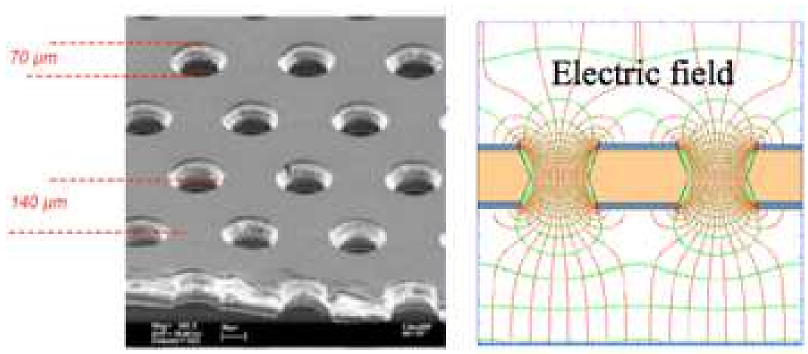

Figure 1.14: Electric field lines through GEM

Operation of wire chambers typically involved only one voltage setting: the voltage on the wire provided both the drift field and the amplification field. A GEM-based detector requires several independent voltage settings: a drift voltage to guide electrons from the ionization point to the GEM, an amplification voltage, and an extraction/transfer voltage to guide electrons from the GEM exit to the readout plane. A detector with a large drift region can be operated as a time projection chamber; a detector with a smaller drift region operates as a simple proportional counter.

A GEM chamber can be read-out by simple conductive strips laid across a flat plane; the readout plane, like the GEM itself, can be fabricated with ordinary lithography techniques on ordinary circuit board materials. Since the readout strips are not involved in the amplification process, they can be made in any shape; 2-D strips and grids, hexagonal pads, radial/azimuthal segments, and other readout geometries are possible.

GEMs have been used in many types of particle physics experiments. One notable early user was the COMPASS experiment at CERN. GEM-based gas detectors have been proposed for components of the International Linear Collider, the STAR experiment and PHENIX experiment at the Relativistic Heavy Ion Collider, and others. The advantages of GEMs, compared to multiwire proportional chambers, include: ease of manufacturing, since large-area GEMs can in principle be mass-produced, while wire chambers require labor-intensive and error-prone assembly; flexible geometry, both for the GEM and the readout pads; and suppression of positive ions, which was a source of field distortions in time-projection chambers operated at high rates.

1.12 Resistive Plate Chambers

After being developed by R. Santonico and R. Cardarelli [19, 20] in 1981 Resistive Plate Chambers has its robust use in different physics and other applications. Resistive Plate Chamber (RPC) is a gas filled detector utilizing a constant and uniform electric field produced between two parallel electrode plates made of a material with high bulk resistivity e.g. glass, bakelite. Since such a detector has very good timing ($\sigma \sim$ 1-2 ns) and spatial resolution, it is well suited for a tracking calorimeter.

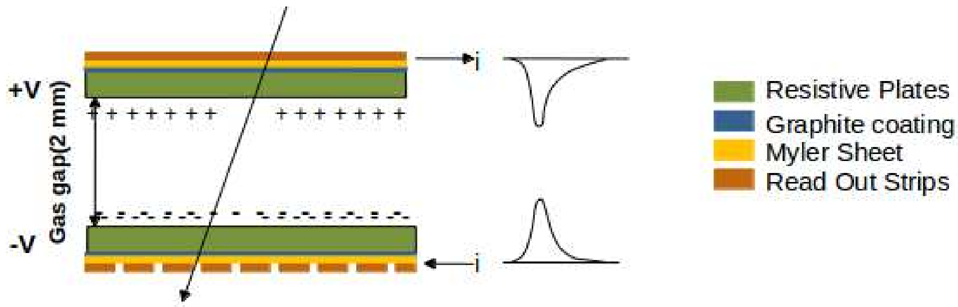

Figure 1.15: Schematic of Resistive Plate Chamber

The operational principle of a RPC can be depicted by the Figure 1.15.

The electrodes of the RPC are made up of high resistive materials e.g. Glass and Bakelite (Bulk resistivity $\sim 10^{10}$ - $10^{12}\Omega$cm). A proper conductive coating is made on the outer surfaces of the plates for uniform distribution of the applied electric field over the surfaces. Mylar sheets are kept above the graphite coating for proper isolation. Surface of resistive electrodes are charged from power supply. Charge-up process is slow due to high resistivity of the material. When a charged particle passes through the gas, it produces avalanches. When readout strips are placed, charge is either drawn in or drawn out from the readout board, generating voltage signals of opposite polarities.

The RPCs are operated in two modes, viz., the avalanche mode and the streamer mode [21]. The characteristic of the avalanche mode is the production of a small amount of charge withn the gas, which allows the RPC to provide short dead time to handle high counting rates. But due to the short height of the pulse generated in this mode the use of preamplifier is necessary. Aging effects due to induced charge is relatively less in this mode. In the streamer mode, the amount of charge produced is considerably larger creating induced signals of larger magnitude, which provides a benefit of not using any preamplifier. But, the dead time is larger and the irreversible damage caused by the induced charge reduces the life of the RPC, although different precautions can be taken to prolong its life under streamer mode of operation. Careful choice of materials, smoothness of surfaces to avoid localization of excess charges, surface treatment to reduce the surface resistivity or providing alternate leakage path for post-streamer recovery are adopted in the major high energy physics experiments.

The operations in these two modes can be explained as below -

Let n_0 be the number of electron present in the cluster at any point inside the gas, α is the first Townsend coefficient and β is the attached coefficient for the gas used. So the number of electrons (n) which will be able to reach the anode is given by the equation

$$n = n_0 e^{(\alpha-\beta)x}$$

where 'x' is the distance between the anode and the place where the charge cluster has developed. The gas gain is defined by

$$M = \frac{n}{n_0}$$

If the value of M > 10^8 the mode is defined as streamer mode and if M << 10^8 the mode of the gas used is defined as avalanche mode.

The two modes can also be understood in a way considering the detector to behave as a plane condenser. The total average charge produced within such a plane condenser can be written as

$$Q = \frac{\epsilon S V}{d}$$

where V is the applied voltage between the electrodes, S is the surface area of each electrode, d is the gap between the electrodes and ϵ is the permittivity of the medium between the electrodes. The streamer mode can be defined for such a detector if Q∼100 pC, and the avalanche mode is defined if Q∼ 1 pC.

According to the application the RPC can be classified into two broad categories : trigger and timing RPCs. Triggering RPCs can be used for triggering minimum ionizing particles, whereas large area RPCs can be used for the time-of-flight measurements. According to the design and the material used for making the RPC, it can be classified into several categories among which single gap, wide-gap, multi-gap, hybrid RPC are important.

The important experiments where RPCs are used in different high energy experiment are BaBar, ALICE-Muon detector,ALICE-TOF, STAR, PHENIX, OPERA, etc.

1.13 Semiconductor Detectors

Semiconductor detectors provide a unique combination of energy and position resolution. In collider detectors they are most widely used as position sensing devices and photo-detectors. Integrated circuit technology allows the formation of high-density micron-scale electrodes, providing excellent position resolution. The high energy resolution is a key parameter in x-ray, gamma, and charged particle spectroscopy. Silicon and germanium are the most commonly used materials, but gallium-arsenide, CdTe, CdZnTe, and other materials are also useful. Semiconductor detectors depend crucially on low-noise electronics, so the detection sensitivity is determined by signal charge and capacitance.

When implemented properly, semiconductor detectors provide significant advantages in systems where the shape of detector signal pulses changes greatly, for example in large semiconductor detectors for gamma rays or in gaseous detectors (e.g. TPCs) where the duration of the current pulse varies with drift time, which can range over orders of magnitude.

1.14 Summary

An overview of the detectors developed so far for uses in high energy and particle physics experiments is given in this chapter. The major detector types, their behaviours and uses in different high energy physics experiments have been discussed. The discussion of the gas-based radiation detectors is one of the important discussions of this chapter. A detail description of different gas ionization detectors like Geiger-M$\ddot{u}$ller counter, Proportional gas chamber, MWPC, TPC, GEM, RPC is a part for the discussion.

Chapter 2

MRPC and its applicaions

2.1 Introduction

The goal of using Resistive Plate Chambers (RPC) is a fast detector that has good time and spatial resolutions suitable for triggering in HEP experimets and can withstand a flux of several kHz/cm^2. Two types of RPCs can be considered as candidates. The more conventional RPC with a 2 mm gas gap was initially developed to operate in streamer mode for low flux applications. Another approach is to have a RPC of several gap width and operate in avalanche mode with more conventional freon-free gas mixtures. A wide gap RPC can also be operated it with a lower average avalanche charge for a given threshold. This leads to a higher rate capability and lower power dissipation in the gas volume.

The Resistive Plate Chamber is essentially two parallel plates enclosing a gas volume. Two plates made of resistive material act as electrodes. By applying voltage to these electrodes, an electric field is generated across the gas gap. If this field is sufficiently strong, electrons liberated in the gas by through-going ionising particles will produce avalanche and thus generates a signal on the external electrodes. The generated charge is deposited on a small region of the plate by the avalanche, this spot is slowly recharged by current flowing through the plate. If the electric field is even more intense, a 'spark' breakdown can be initiated by the avalanche. The resistive plates limit the spread of the discharge; in general there is a factor 10 to 20 increase in the charge generated by a spark breakdown compared to the avalanche signal.

2.2 Wide gap RPC

The gas gap in an RPC is used both for gas gain via avalanche process and also as the source of primary ionization. The avalanche pulse is generated by a multiplicative gas gain across the gas gap, thus the largest gain is from electrons that traverse the entire gap. An electron that is produced at a distance 'x' from the anode will have a gain of $G^{x/D}$, where D is the distance between the anode and cathode plate, and G is the gain of an electron traversing the whole gap. A minimum ionizing particle traversing a gas volume containing Argon (a typical gas used in gaseous detectors) produces 30 primary ionization clusters per cm (thus 3 clusters/mm on average). Poisson statistics shows that there is 5% probability that there are no clusters of primary ionization in the first millimeter of the gas gap. So in order to work near to 100% efficiency, the gain for a single electron over the remaining gap has to be large enough to produce a detectable pulse. Thus ifthere are no clusters in the first millimeter, there remains only 1 mm of the 2 mm gas gap to produce an avalanche signal above the discrimination level. If, typically, the avalanche gain is set to be 10^5 across this 1 mm, then a gain of 10^{10} for an electron can be obtained that avalanches over the full 2 mm. However, for a chamber with an 8 mm gas gap, there remains 7 mm for the avalanche process; thus, in this case, the gain is set to be 10^5 over 7 mm, which gives a gain of 5.2×10^5 for an electron that traverses the full 8 mm. Thus there is a dramatic reduction of dynamic range of avalanche pulse size (10^5 is reduced to 5.2) with a larger gas gap (2 mm increased to 8 mm). As sparks are usually associated with a high density of positive ions, it would be no surprise that a larger gas gap reduces the probability of sparks.

It is already demonstrated [17] that a narrow gap RPC has a superior timing resolution compared to the wide gap RPC, although wide gap RPC has a superior rate handling capability. This is due to a lower dynamic range of avalanche charge, and thus a lower average charge being produced. Thus the power dissipated in the gas gap in the wide gap RPC is also a factor 10 lower than the narrow gap RPC.

2.3 Multi-gap Resistive Plate Chamber (MRPC)

As discussed earlier, primary ionization follows Poisson statistics. So to work at efficiencies close to 100%, a detectable avalanche signal needs to be produced from a single electron cluster located anywhere within the closest 1-1.5mm to the cathode [19]. The variation in the position of the initial clusters of primary ionization generates a time jitter. Typically, at the electric fields usual in the wide gap RPC, the drift speed of electrons is ∼10ns/mm. So the time resolutions with a full width at base (FWAB) is expected to be in the order of 15 ns [17]. If the wide gap is divided into smaller sub-gaps, then the distribution of primary ionization will cause less time jitter within the gaps. In Figure 2.1, the advantages of dividing the wide gap into smaller sub-gaps and thereby improvising the timing is demonstrated.

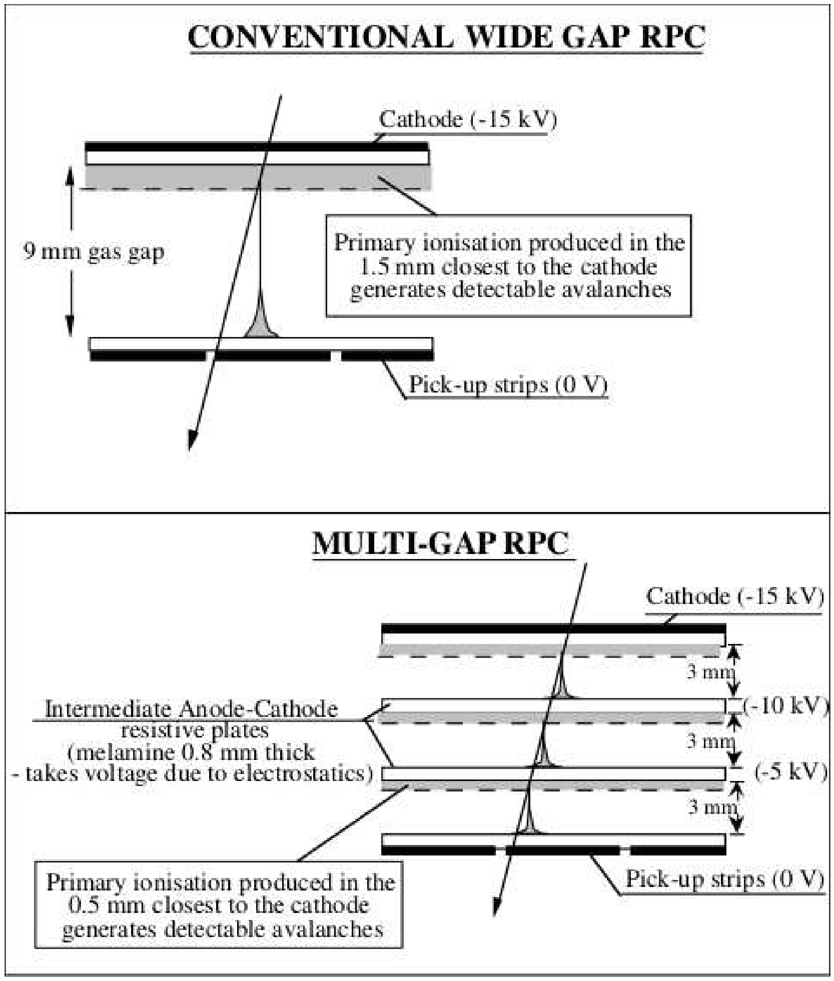

Figure 2.1: Schematic of working principle of MRPC

It can be seen from Figure 2.1 that a 9 mm gas gap is divided into 3 × 3 mm sub-gaps [20]. The voltage is applied on outermost electrodes. The internal plates are electrically floating, taking a voltage due to electrostatics. If a minimum ionizing particle passes through the detector, on average each sub-gap produces a detectable avalanche, but the limiting case is when just one sub-gap generates a detectable avalanche. In this limiting case the initial cluster of primary ionization is within 0.5 mm of one of the three cathode surfaces; thus one could expect a threefold reduction in time jitter.

Obviously it is mandatory to operate these two devices (RPC and MRPC) with a different Townsend coefficient, α. For example, an RPC with one typical 9 mm gap filled with a gas that produces an average of 3 primary ionization clusters per mm for a minimum ionizing particle. Typical results [20] shows that 99% of through-going charged particles produce ionization within the 1.5 mm closest to the cathode. If the gas gain is set to be 10^6 over the remaining 7.5 mm, then a single electron avalanching over this distance would produce a signal of 10 fC, which may be considered as a reasonable lower limit for the threshold for electronics used on large area detectors. The gas gain of a single electron avalanching over the full 9 mm would be of the order of 1.6 $\times 10^7$. The dynamic range for this case is 16. In order to achieve this gas gain, it is found that [20] the value of the Townsend coefficient has to be $\frac{\alpha}{p} = 0.024$. In the case of $3 \times$ 3 mm gas gaps, around 99% of through-going charged particles produce ionization within any of 0.5 mm closest to the cathode plate of all sub-gaps (as shown in Figure 2.1). The minimum signal is when only one gap generates a detectable avalanche, with a single electron avalanching over 2.5 mm. Since the avalanche forms over a factor 3 shorter distance, the induced signal is a factor 3 smaller; thus to produce a 10 fC signal an avalanche is needed that generates 3×10^6 electrons. An electron that avalanches over the full 3 mm would produce an avalanche of 5.9×10^7 electrons, making the dynamic range of gain 20, keeping the value of $\frac{\alpha}{p} = 0.078$ by increasing the electric field [31].

The MRPC is mainly operated at atmospheric pressure and consists of several small gas gaps (0.2 mm to 0.5 mm for each gap) [18]. It is important to understand whether the electrically-floating internal resistive plates acquire the correct voltage. Such a case a shown schematically in Figure 2.2. Since each gap has the same width, on the average each will produce the same number of avalanches from the flux of incoming charged particle. This indicates that the flow of electrons and ions will be same for all gaps. Each immediate plate will receive a flow of electrons into one surface balanced by a flow of positive ions into the opposite surface.

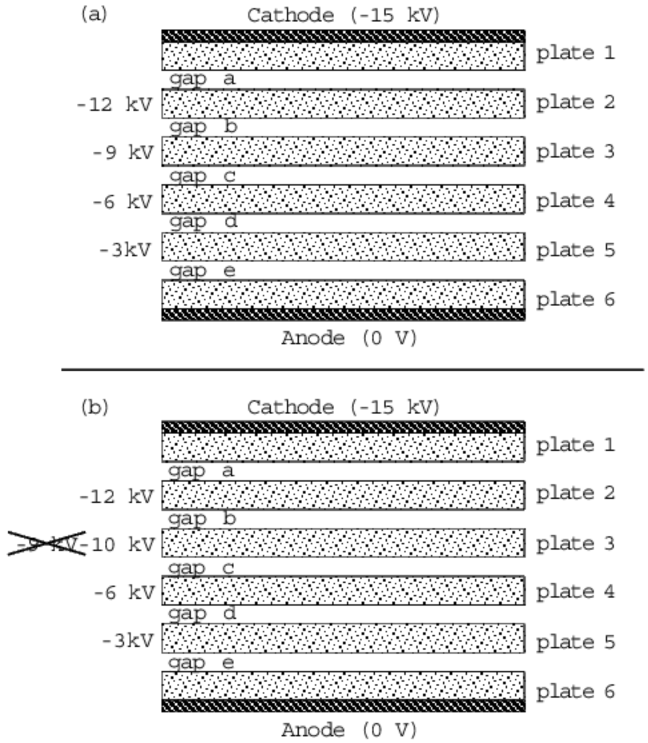

Figure 2.2: Equi-potential surfaces of MRPC

Thus the net charge to an immediate plate is zero, making the state stable. Now let's consider the case, where the immediate plates has 'incorrect' voltage (as depicted by part-b of Figure 2.2 where the voltage on plate 3 has shifted from -9 kV to -10 kV). As labeled in Figure 2.2, this shift of voltage decreases the field in gap b and increases it at gap c. So the flow of electrons from gap b into plate 3 will be reduced, and the flow of positive ions from gap c will be increased, which in turn make the voltage on plate 3 more positive. So the voltages are automatically adjusted to give equal gain in each of the gaps.

In the next few sections the dependency of different parameters controlling the functions of MRPC followed by the application of MRPC used in different high energy experiments will be discussed.

2.4 Dependence of voltage with gap size

The MRPC operating voltage increases with the gap size at a lower rate than expected from a linear relationship [21], i.e. the operating electric field decreases with the gap. The simplest functional relationship that can be predicted between the voltage V per gap and the gap size g, for fixed pressure and temperature, as

$$V = Kg^{\gamma}$$

where K and γ are the parameters depending on the gas and operating mode, with $0 < \gamma < 1$. The parameters K and γ can be obtained by fitting the existing data on different gases for both avalanche and streamer operation [21].

2.5 Dependence of temperature and pressure

The correction of the operating voltage for changes of pressure and temperature is usually done [22] by scaling the applied voltage V_a according to the relationship

$$V = V_a \frac{P_0 T}{P T_0}$$

which gives the operating voltage V scaled at some standard pressure P_0 and temperature T_0. Although this formula is valid for small changes of temperature and pressure.

2.6 Application of MRPC

MRPC due to its layered structure and having good position and time resolutions has been used in different high energy and particle physics experiments. Also as a spin-off use, MRPsC, as a probable alternative substitute of scintillator detectors, has potential use in Nuclear medicine fields specially in TOF-PET imaging systems.

In the following section, some of the uses of MRPC, both for trigger and timing purposes in recent high energy physics experiments will be discussed. The discussion will proceed further by reviewing its use in medical fields in the nest chapter.

2.6.1 MRPC in LHCb Muon System

The LHCb Muon system [23] is composed of five muon-tracking stations interleaved in a longitudinally segmented shield. It is mainly used to provide muon identification and L0 muon trigger formation. As good time resolution for bunch-crossing identification and reasonable momentum resolution is essential for this system, MRPC is selected as a good candidate.

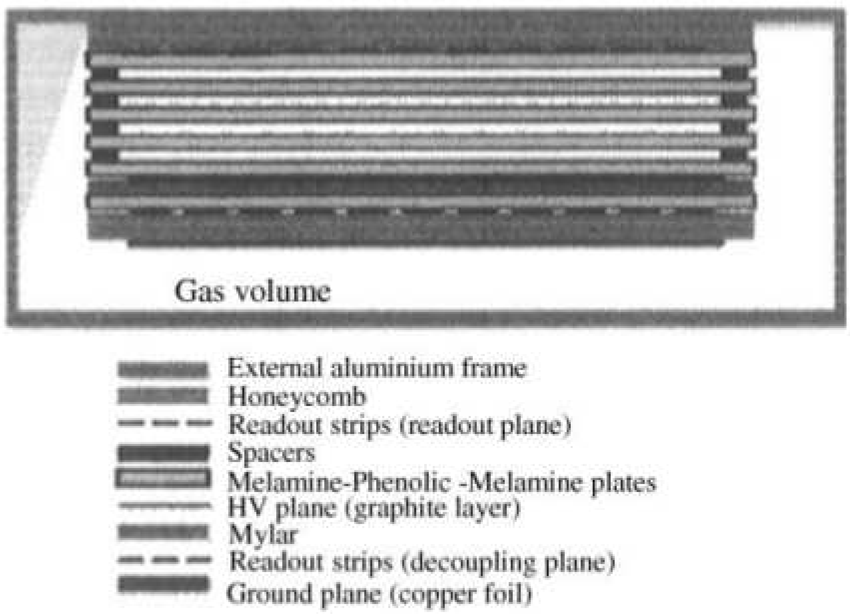

Figure 2.3: Schematic of the MRPC in LHCb experiment

Figure 2.3 shows the schematic of the MRPC used in CERN PS and SPS. The detector is composed of four gas gaps, each having thicknesses of 0.66 mm. Nylon button spacers are used to maintain the uniform gas gap. The electrodes are 0.7 mm thick melamine-phenolic laminates, having bulk resistivity 5-6$\times10^{11}\Omega$-cm. The high-voltage (HV) plane consists of a graphite layer sprayed on the outer surface of the external resistive plate. The readout plane is made of kapton foil with copper-gold coated strips having dimension of 24 cm $\times$ 1.3 cm. Each of the strips are connected to an amplifier shaper discriminator chip. The gas mixture was 96% $C_2H_2F_4$/3% iso-Butane/1% SF_6. Also, 1% of water vapour was added to this gas mixture to maintain the stability of the electrical and mechanical properties of the plates.

The detector was tested in Gamma Irradiation Facility (GIF) at CERN. The detector was reported [24] to operate with 97% efficiency at 18 kV for an approximate rate 1.9 kHz/cm^2. The time resolution (FWHM) was found to be 1.5 to 1.9 ns. Also typical noise rate measurement shows that the detector is capable of measuring 60 Hz/cm^2.

2.6.2 The TOF detector in ALICE experiment

ALICE [25] experiment is a dedicated heavy-ion experiment at the CERN LHC to study the physics aspects of strongly interacting matter at extreme energy densities where the formation of quark-gluon plasma (QGP) is expected. ALICE is also helpful for the study of proton-proton collisions. Particle Identification (PID) is also a crucial aspect of the ALICE experiment.

The Time-Of-Flight system in ALICE experiment is a 7 m long barrel having radius of 3.7 m. The design of ALICE is based on strips each having an effective area of 1.2 m $\times$ 7 cm and having six gas gaps. Each strip has 96 read-out pads for collecting single-ended differential signal from the detector, each having area of 2.5 $\times$ 3.5 cm^2. The TOF system consists of 1600 such strips. The MRPC system allows a differential signal, derived from the strips, which is fed to the front-end electronics.

A typical cross-sectional view of ALICE TOF detector is shown in Figure 2.4.

The commissioning of the full TOF detector was performed in 2008 and 2009 [26, 27] and all operating parameters have been measured to be well within the expectations of the project. The HV, noise and trigger performances have been measured during the LHC operation. At the maximum charged particle flux sustainable by the ALICE detector, corresponding to a instantaneous luminosity of $L = 2 \times 10^{30} s^{-1} cm^{-2}$, the current drawn by the MRPCs comprising the TOF is reported to be around 35 mA. Also the efficiency measurements indicate the

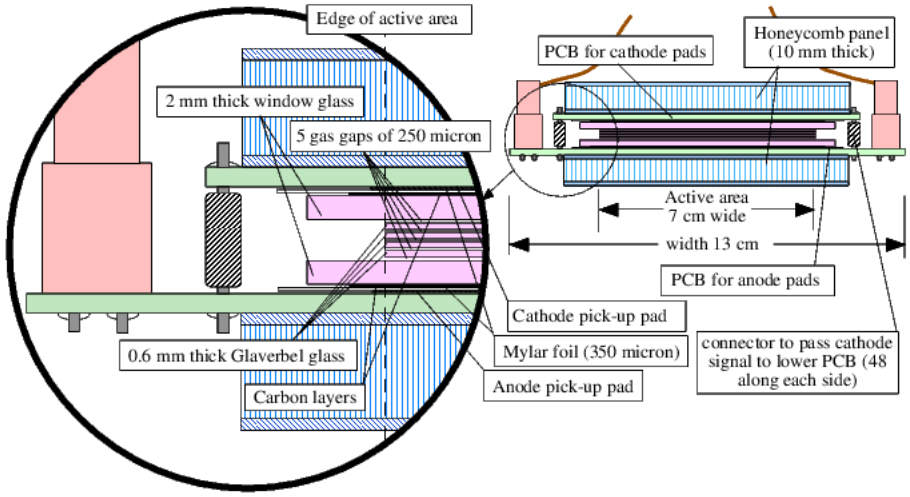

Figure 2.4: Schematic of the MRPC in ALICE experiment

performance of the MRPC to be around 98%. Also the time resolution for the TOF MRPC for the experiment is reported [32] to be around 50 ps.

The TOF detector has been taking data since the first p-p collisions recorded in ALICE in December 2009, with high performance in terms of dark current,noise,efficiency and time resolution. During the 2010 data taking, the TOF successfully provided particle identification both for p-p and PbPb collisions and many analysis carried out by the ALICE Collaboration are widely using information provided by the TOF detector.

2.6.3 TOF detector in CBM expeiment

At the upcoming FAIR accelerator facility (GSI,Germany) the Compressed Baryonic Matter(CBM) experiment investigates the strongly interacting matter under extremely high net baryon densities and moderate temperatures. [28]. A time-of-flight system based on MRPCs, having the capability to handle particle rate up to 20 kHz/cm^2 is used for hadron identification in the experiment.

The typical structure of the MRPCs used in the experiment is depicted in Figure 2.5.

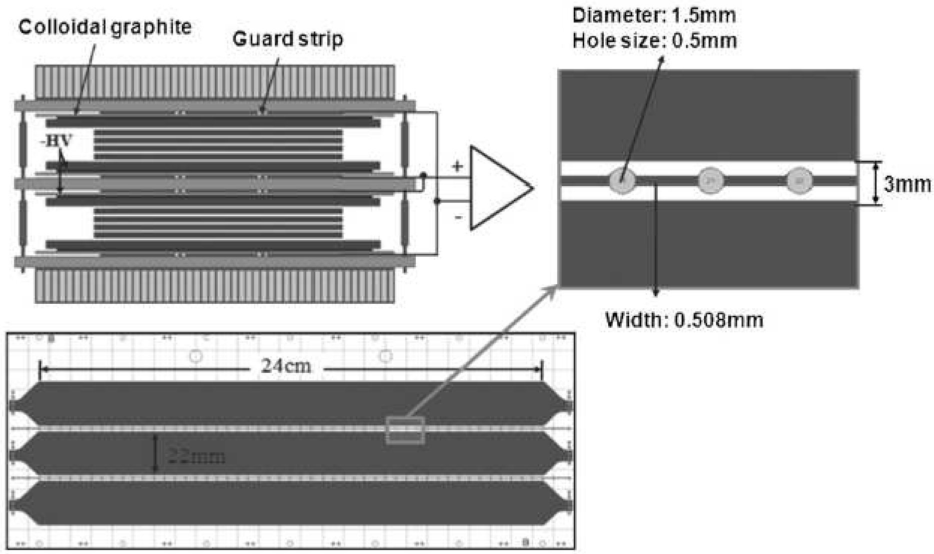

Figure 2.5: Schematic of the MRPC in CBM experiment

Special silicate glass is used for the construction of the high rate MRPC. A gas mixture of 96.5%$C_2H_2F_4$, 3%iso-C_4H10 and 0.5% SF_6 at atmospheric pressure is used for the experiment.

The schematic of the beam test set-up is shown in Figure 2.6.

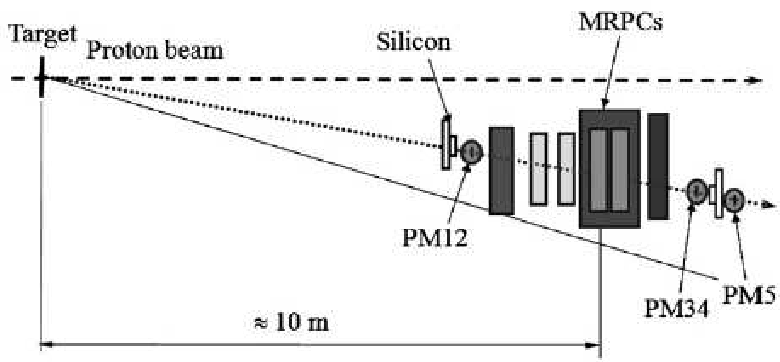

Figure 2.6: Beam test set-up of the MRPC in CBM experiment

It is reported that [29] the MRPCs are performing with a time resolution (σ) of 70 ps and efiiciency of 95% at an operating voltage of $\pm$ 6.8 kV.

2.6.4 MRPC as a Neutron Detector in NeuLAND Experiment

The design of NeuLAND consists of a layered structure of passive converting material(iron) and active detectors. The neutrons, reacting with the iron converter, produces charged particles (mainly protons). These protons are subsequently detected by MRPC detectors. The time resolution and efficiency of those detectors are studied using monoenergetic electron beams at the superconducting electron linear accelerator ELBE in Dresden, Germany. In the experiment the neutron detection efficiency of the NeuLAND MRPC is measured.

A schematic layout of the experimental setup at the The Svedberg Laboratory(TSL) neutron beam facility is shown in Figure 2.7.

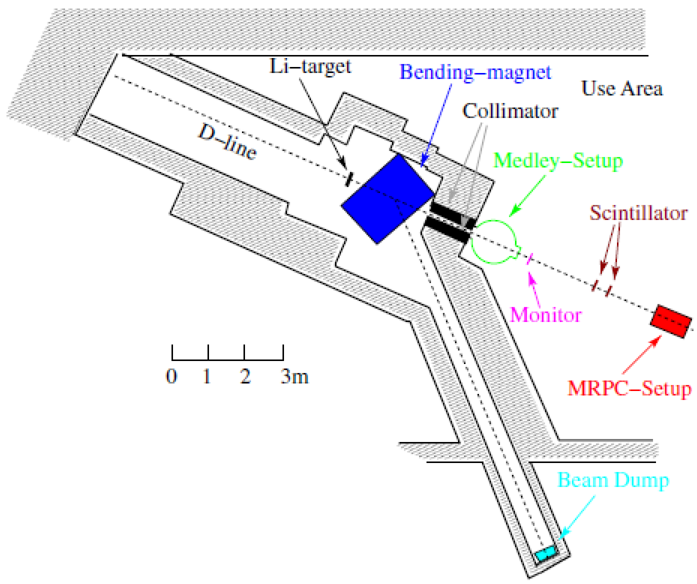

Figure 2.7: Experimental set-up of the MRPC in NeuLAND experiment

Also the schematic of a 2 × 4 gap MRPC NeuLAND prototype is shown in Figure 2.8[30].

Within the setup a single ended readout is adopted. For this purpose, the middle electrode is used to divide the detector in 8 strips. A thin film of Licron is used to provide high voltage to

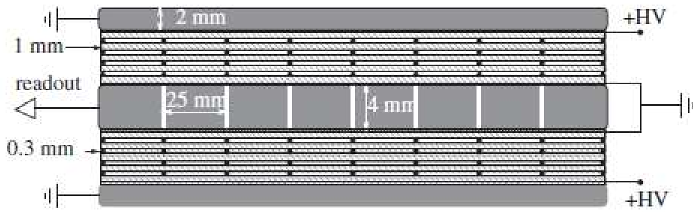

Figure 2.8: Schematic of the MRPC prototype in NeuLAND experiment

the electrodes. The detector is operated at 12 kV. The readout strips are 2.5 cm wide and 40 cm long. A gas mixture of 85% $C_2H_2F_4$, 10%SF_6 and 5% iso-C_4H_{10} is used for detecting the beam particles. The detector is reported [30] to have an efficiency of (0.77 $\pm$ 0.33)% for 175 MeV neutrons considering statistical and other errors. Also this lower value for efficiency was reported for the high charge threshold used in the experiment.

2.7 Summary

Due to high efficiency and good time resolution compared with the standard single gap RPC, MRPC is more suitable candidate to be used in different high energy physics experiments. To summerize the chapter a table of different experiments using MRPC as particle detector is shown.

Table 2.1: MRPC as a particle detector in different high energy experiments

Experiment	No. of gaps	Gas Mixture	Gap Width	Electrode Material	Rate Capability	Time Resolution(σ)
LHCb Muon system	Four (4)	$C_2H_2F_4$: iso-butane : SF_6 (96% : 3% : 1%)	0.66 mm	melamine-phenolic laminates	60 Hz/ cm^2	1.5 -1.9 ns
TOF detector in ALICE	Six (6)	$C_2H_2F_4$:SF_6 (90% : 3%)	0.25 mm	Soda-lime commercial glass	10 Hz	86 ps
TOF detector in CBM	Ten (10)	$C_2H_2F_4$: iso-butane : SF_6 (96.5% : 3% : 0.5%)	0.5 mm	Special Silicate Glass	20 kHz/ cm^2	70 ps
Neutron Detector in NeuLand Experiment	2 × 4 gaps	$C_2H_2F_4$: iso-butane : SF_6 (85% : 5% : 10%)	0.3 mm	Float Glass	4 kHz/ cm^2	-

Chapter 3

MRPC as a Medical Imaging Detector

3.1 Introduction

Medical imaging is the technique, process and art of creating visual representations of the interior of a body for clinical analysis and medical intervention. Medical imaging seeks to reveal internal structures hidden by the skin and bones, as well as to diagnose disease. It also establishes a database of normal anatomy and physiology to make it possible to identify abnormalities.

As a discipline and in its widest sense, it is part of biological imaging and incorporates radiology which uses the imaging technologies of X-ray radiography, magnetic resonance imaging, medical ultrasonography or ultrasound, endoscopy, elastography, tactile imaging, thermography, medical photography and nuclear medicine functional imaging techniques as positron emission tomography.

As a field of scientific investigation, medical imaging constitutes a sub-discipline of biomedical engineering, medical physics or medicine depending on the context: Research and development in the area of instrumentation, image acquisition (e.g. radiography), modeling and quantification are usually the preserve of biomedical engineering, medical physics, and computer science.

In the following sections a general introduction to Nuclear Medicine and Positron Emission Tomography will be discussed, which will be followed by the discussions of simulation results of the photon conversion in MRPC detector and test results of different MRPC prototypes as a feasibility study for making it suitable as a PET detector.

3.2 Nuclear Medicine

Nuclear medicine encompasses both diagnostic imaging and treatment of disease and may also be referred to as molecular medicine or molecular imaging & therapeutics. Nuclear medicine uses certain properties of isotopes and the energetic particles emitted from radioactive material to diagnose or treat various pathology. Different from the typical concept of anatomic radiology, nuclear medicine enables assessment of physiology. This function-based approach to medical evaluation has useful applications in most subspecialties, notably oncology, neurology, and cardiology. Gamma cameras are used in e.g. scintigraphy to detect regions of biologic activity that may be associated with disease. Relatively short lived isotope, such as ^{123}I is administered to the patient. Isotopes are often preferentially absorbed by biologically active tissues in the body, and can be used to identify tumors or fracture points in bone. Images are acquired after collimated photons are detected by a crystal that gives off a light signal, which is in turn amplified and converted into count data.

Table 3.1 shows different types of medical scanners used in Nuclear medicine.

3.3 Positron Emission Tomography

In the field of nuclear medicine, Positron Emission Tomography (PET) is a very powerful imaging technique that provides three-dimensional (3-D) images of functional processes in the body [86]. In this technique, a radio-pharmaceutical having positron emitter, such as ^{11}C and ^{13}N, is administered into the object of study. Inside the object, these positrons annihilate with the available electrons to produce two nearly back-to-back photons each having energy of 511 keV. The correlated detection of these photons with efficient detectors can lead to the identification of the annihilation point. A line is drawn connecting the detected positions of the two gammas; thus an image can be constructed when many such lines have been recorded. If the time of arrival of the gamma in the detector can be measured (with some precision), then the position of the positron annihilation can be localized along this line. This technique is known as TOF-PET and studies have shown that the resultant image becomes much clearer due to the reduction of the background [34]. As these positron emitters are injected via some

Table 3.1: Different Scanners used in Medical Imaging

Scan	Medium	Purpose	Comments
X-ray	X-ray Generator Fluorescence Plate	Bone Scan Fractures	A few seconds, useful for gross understanding
CT	Movable X-ray source and detectors	Disorders of body functions, injuries	A few minutes, better 2D image, good resolution
MRI	Radio Frequency, Strong magnetic field, contrast materials	Heart, Lung Liver	15-45 minutes required, cleaner image than X-ray and CT
NMI	Radio-nuclides,e.g., gamma camera	Blood flow, Heart Bone, Lung, Kidney Thyroid, Injuries	13-15 minutes, very specific, more accurate, real fnctonal image
High resolution X-ray imaging	X-Rays and GEM detector	Images like soft/ Hard X-rays, 2D images	Less expensive, minimum dose Short Scanning time, better resolution, user friendly
PET/TOF-PET	Radio-nuclides, chemical tag positron-sensitive gamma camera	Specially for Cancer tumor, heart 2D/3D images	Less than few hours, very expensive High quality images

physiological substances, mapping of the density of the positron sources can give information about the activity inside the object of interest.

In a conventional image reconstruction method, the activity profiles are projected and overlapped on the image grid, which in turn exalts the larger structures, corresponding to the lower spatial frequencies. To correct this, the back-projection is filtered by applying a Fourier transform over the frequency domain. The additional TOF information reduces the length determined by the timing resolution of the scanner, over which the coincident image is back-projected for image reconstruction. For example [87], for a coincidence timing resolution of 600 ps the positional uncertainty is 9 cm Full Width at Half Maximum along the line pair.

The average diameter of a typical patient (torso) is 25-30 cm, or approximately three times the TOF positional uncertainty. The ratio of patient diameter (D) to the positional uncertainty (x) has been reported to be representative of the noise reduction, or the gain of sensitivity. An improvement in coincidence time resolution will increase the sensitivity of the system.

In conventional PET scanners the process of detecting scintillation light using Photo-Multiplier Tube (PMT) and associated electronics results in a large dead time. These systems, due to large dead times can only handle low rate applications, requiring large dose for obtaining good image quality. In addition to that, the scanners suffer from the limitations of a short Field of View (FOV) [15-25 cm] and relatively poorer position resolution.

3.4 MRPC as TOF-PET Detector

The Multi-gap Resistive Plate Chamber (MRPC) is capable of high precision time measurements and has been used for time-of- flight purposes in many experiments [36, 37]. The interaction of the gammas with the MRPC resistive plates provides the possibility of their detection. However, the efficiency of the chamber depends on the probability of conversion and the resultant electron emerging into one of the gas gaps [38].

For several years different scientific groups across the world have been trying to build MRPC-based PET imaging systems with a varying number of gaps [39, 40]. However, like many other gas-based detector systems, the efficiency of conversion of 511 keV photons is very low (0.15%) for MRPC [41]. The conversion efficiency up to 20-25% has been obtained by optimization study using the combined layers of lead as converters and glass as MRPC electrodes [39, 42]. Throughout this section I shall discuss the process of optimization of MRPC as a suitable TOF-PET detector. A two-stag simulation process will be discussed as the optimization procedure. At first GEANT4 [43] has been used to simulate the conversion of the incident photons and secondly the electrons obtained by photon conversion are considered to be the particles ionizing the gas. The processes from ionization to signal generation have been implemented in another Monte Carlo (MC) code, as the final step.

3.4.1 Simulation Procedure

3.4.1.1 Conversion procedure of 511 keV gamma within the MRPC detector

As a first step of the simulation I have considered the following configuration of the detector set-up, as shown by Figure 3.1.

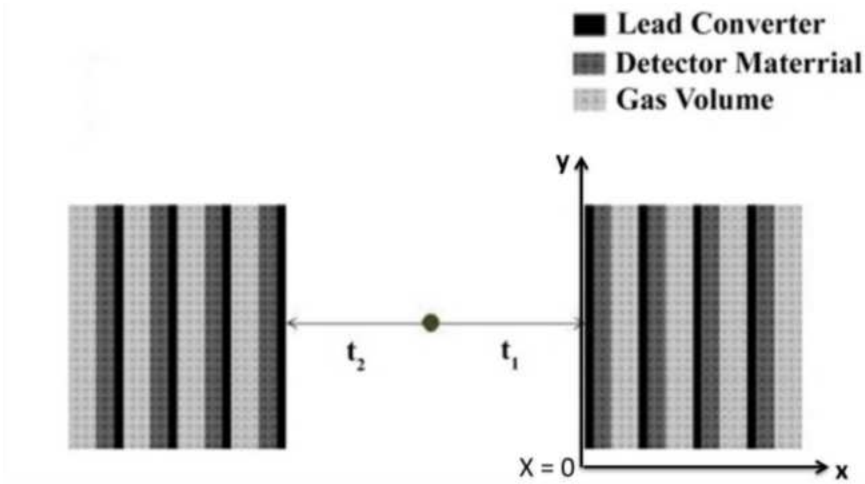

Figure 3.1: Schematic diagram of the detector configuration for simulation

GEANT4 (version 4.9.4) has been used to simulate the response of photons which pass through the converter and generate electrons ultimately reaching the gas volume. The input photon-pairs are considered to be almost back-to-back. As shown in Figure 3.1 a combination of 0.25 mm gas gap and converter of adjustable thickness is termed as one layer. Materials, e.g., Lead as converter, glass having a fixed thickness of 700 μm as resistive electrodes of MRPC and the gas mixture $C_2F_4H_2$/i-C_4H_{10}/SF_6 (95/4.5/0.5) have been implemented in GEANT4 framework. For gamma ray conversion, the data file G4EMLOW version 6.19, containing cross-sections for low energy electromagnetic processes, was used. Two back-to-back 511 keV photons are used as the input for every event. Any particle (photon or electron) back-scattered from one layer to the other are not considered for further study. After conversion, the low energy electrons with sufficient energy reach the gas volume for signal generation. Increasing the number of Pb-MRPC layers improves the conversion probability. The **conversion efficiency** of each detector is defined as the ratio of the number of the photons that produce conversion electrons reaching in any of the gas gaps to the number of the incident photons.

3.4.1.2 Monte Carlo study for response of MRPC

For a Monte-Carlo based procedure, which has been developed to study the response of the incident electrons for signal generation, the electrons reaching the gas gap, as discussed in the previous sub-section, are used as input. When an electron reaches the gas gap it has a certain probability to ionize it, which leads to the avalanche formation. During primary ionization, the average number of clusters formed per incident electron in the gas mixture is taken to be nine/0.2 mm [44], which is higher for slow conversion electrons when compared with the value commonly used for minimum ionizing particles for the gas of the given composition. The avalanche formation by the electrons of the primary cluster while passing through the gas volume is governed by the Townsend coefficient (α) and the attachment coefficient (η), which in this work are simulated by Magboltz [45]. I have considered the variation of Townsend and attachment coefficient along with the drift velocity of electrons within the gas mixture as mentioned earlier for this simulation purpose as depicted by the Figure 3.2 and Figure 3.3 .

If we consider the electrode to be situated at x=0, as shown in Figure 3.1, then the probability to obtain 'n' avalanche electrons at any position 'x' within the gas volume, is given by the relation [46]

$$\begin{aligned} P(n,x) &= k\frac{\overline{n}(x)-1}{\overline{n}(x)-k}\ , && n=0 \\ &= \overline{n}(x)\left(\frac{1-k}{\overline{n}(x)-k}\right)^{2}\left(\frac{\overline{n}(x)-1}{\overline{n}(x)-k}\right)^{n-1}\ , && n>0 \end{aligned} \tag{3.1}$$

where $\overline{n}(x) = e^{(\alpha-\eta)x}$ and $k = \frac{\eta}{\alpha}$.

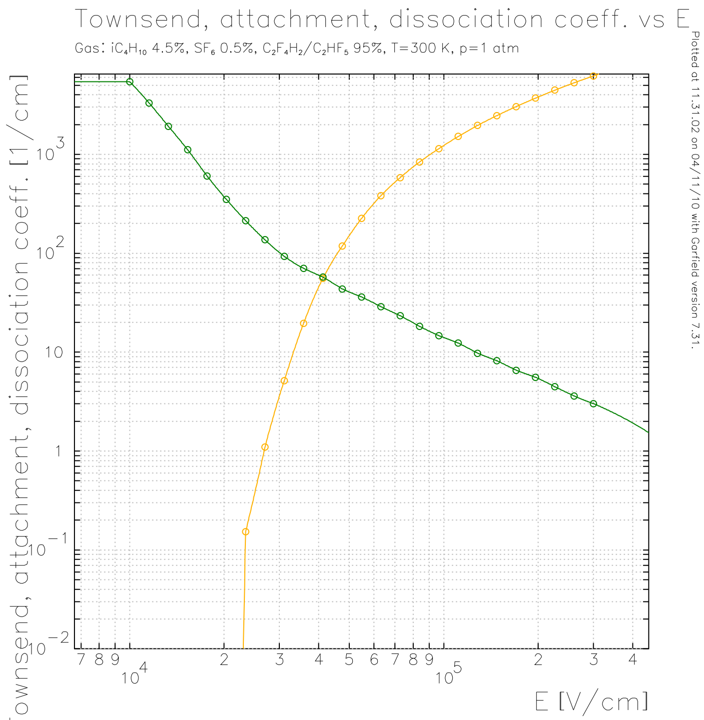

Figure 3.2: Variation of Townsend and attachment coefficient with the electric field

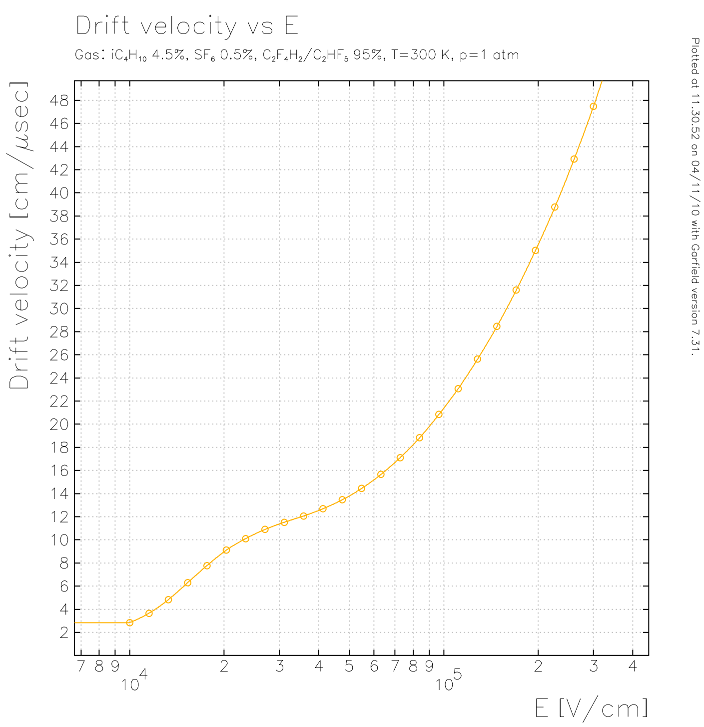

Figure 3.3: Variation of drift velocity with the electric field

To reduce the computational time in avalanche formation by a large number of secondary electrons, in our case for n(x) > 200, we have used the Central Limit Theorem (CLT), as mentioned in [45], to obtain the average number of electrons and their spread at a particular position. The space charge effect is also implemented by the application of a cut off on the number of avalanche electrons, after which multiplication stops. In the present case, the threshold for the number of the avalanche electron is set to be 1.6×10^7. Finally the avalanche electrons induce current signals onto the MRPC pick-up strips. The current signal induced to the MRPC eletrode can be wriiten by th formula [46]

$$i(t) = \frac{E^w v e_0 N(t)}{V^w} \tag{3.2}$$

where e_0 is the electron charge, E^w is called 'weighting field' , v is the electron drift velocity and N(t) is the number of primary electrons present at any instant of time t. The **weighting field** is defined as the electric field within the gas gap if any one of the electrode is put in an electrostatic potential V^w, all the other electrodes being grounded. The weighting field for any MRPC configuration can be calculated if we consider the MRPC elecrodes are very large compared to the gas gap. For such a configuration, considering the MRPC detector as a parallel plate capacitor, the electric fields E_i within the capacitor with n number of layers, each having thickness of d_i and permittivity ε_i, can be written as

$$\begin{aligned} &\sum_{i=1}^{n} E_i d_i = V^w \\ and \quad &\varepsilon_i E_i = \varepsilon_j E_j \end{aligned}$$

for all the neihbouring layers.

The particle is said to be detected if the induced charge crosses a threshold value, which is 20 fC in this simulation procedure. The **detection efficiency** of the MRPC is defined as the ratio of the number of incident electrons for which the induced charge exceeds the threshold value to the number of incident photons for which conversion electrons enter the gas gap.

The efficiency and time response of the system for a varying number of layers have been simulated. However, no effort has been made to implement the response of the readout electronics.

The **avalanche growth time** is defined as the time taken by the avalanche, starting from time t=0, to produce sufficient number of electrons within the gas volume so that it can induce a charge greater than 20 fC to the MRPC electrodes. The standard deviation of the distribution of the avalanche growth time taken over a large number of particles is called the **time resolution** (TR) of the detector for a single photon. For a pair of detectors, facing each other, as shown in Figure 3.1, the difference between the times (t_1) and (t_2) taken by two photons to produce detectable signals in the respective detectors is defined as the **pair time difference** [δt = t_1 t_2]. The standard deviation of the pair time difference taken over a large number of photon pairs is defined as the **pair time resolution** (PTR) for pair of photons. For present case, as two detectors are of exactly similar configuration, PTR is governed mainly by the folding of the TRs of two detectors.

3.4.2 Simulation Results

3.4.2.1 Photon conversion efficiency

Figure 3.4 shows the variation of conversion efficiency with the number of layers in the system, where the converter thickness has also been varied. By increasing the number of layers, the effective thickness increases. It is seen clearly that with the increasing number of layers, the conversion efficiency increases.

However for converter thickness of 0.1 mm or higher, the efficiency saturates at about 20% thereby suggesting the converted electrons stop inside the glass volume. Use of thinner converter in large numbers however increases the efficiency further. The plot indicates that an efficiency greater than 30% can be achieved with a configuration having 120 layers with the converter thickness of 0.02 mm. It is also seen that the 0.008 mm thin converter also gives an impressive conversion efficiency beyond 140 layers. A saturation of the conversion efficiency for more than 140 layers is observed for almost all the converter thickness studied. As the improvement of the conversion efficiency by varying the thickness is the main goal of this study, it is evident from the figure that the lead thickness of 0.04 mm and somewhat lower can be used for the conversion of the incident photons without substantial absorption of the converted electrons inside the converter. The range of thickness also matches with the highest stopping power

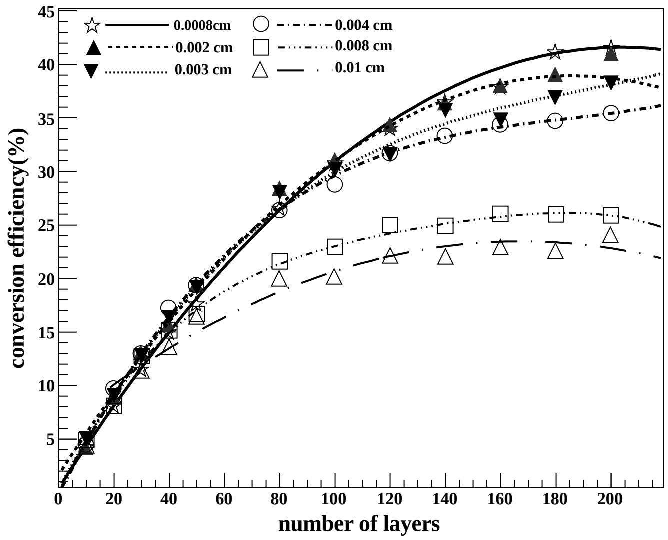

Figure 3.4: Variation of conversion efficiency with number of layers for different converter thickness

(16 keV/mm) of conversion electrons in lead. During all through the subsequent simulation procedure the optimized converter thickness is considered as 0.04 mm.

Figure 3.5 indicates the photon conversion efficiency with the configuration prescribed earlier for different materials each having the same thickness of 0.04 mm. The plot clearly indicates that lead is the most suitable converter for 511 keV photons for 0.04 mm thickness of the converter layer.

3.4.2.2 MRPC time response

In Figure 3.6 the distribution of the signal collection time, as obtained from MC simulation for MRPC response for photons producing an electron in any of the gas gap is plotted. The time resolution (σ) is found to be 19 ps , which is in good agreement with earlier simulation results for comparable number of conversion electrons [47].

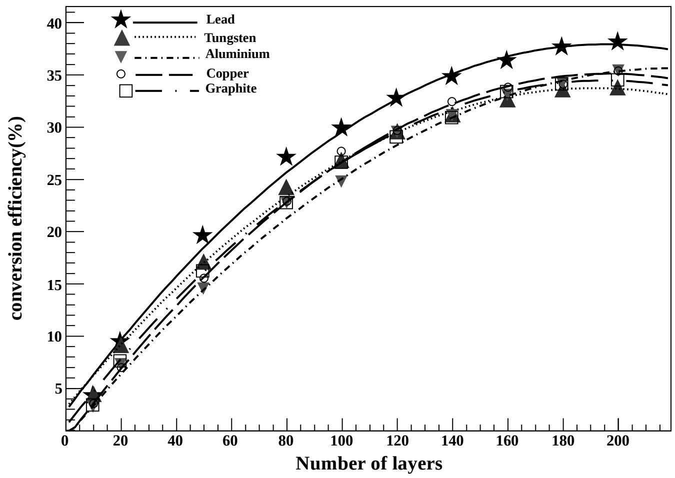

Figure 3.5: Variation of conversion efficiency with number of layers for different material

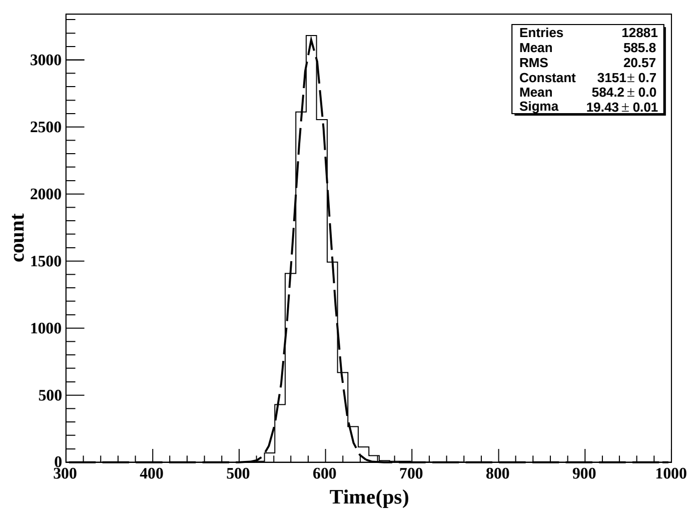

Figure 3.6: Time response of single MRPC detector

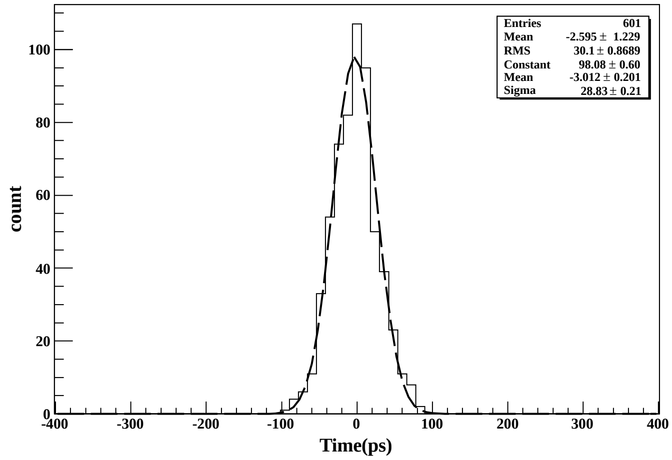

Figure 3.7: Pair time resolution of back-to-back MRPC detectors

The pair time resolution was calculated considering the start time to be zero. Figure 3.7 shows the distribution of the pair time difference collected from both the detectors. The standard deviation of the plot, 28 ps in this case, has a good agreement with the fact that both the detectors have same intrinsic time resolution.

3.4.2.3 Estimation of position resolution for an extended source of photon pairs

The position resolution of the detector in the prescribed configuration for an extended annihilation source is also simulated. For this purpose, a Gaussian spread of the source position in one direction, e.g., in z-direction (perpendicular to the plane of Figure 3.1) keeping mean at zero and sigma of 0.5 mm is introduced and the corresponding time difference measured by the pair of detectors is obtained. In Figure 3.8 the ratio of the distance of the source from the origin to the corresponding measured time difference is plotted.

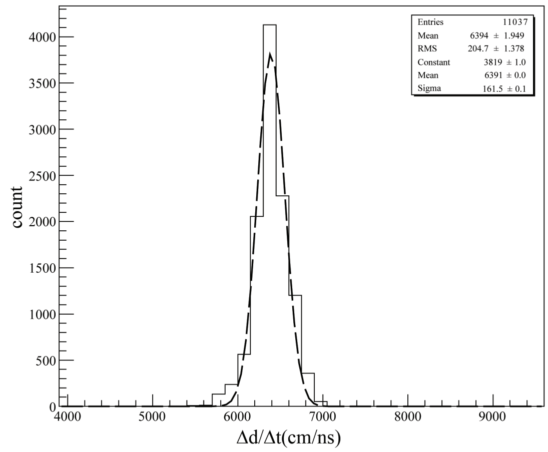

Figure 3.8: Position estimation for a MRPC detectors

The spread gives an estimation of the resolution of the position measurement. In this simulation the time of detection of a photon by the detectors is the sum of the time taken by the photon to reach the detector from the point of its origin and the signal generation time for each detector. It should be mentioned that the contribution from the second plays the leading role in the spread of the detection time.

3.5 Fabrication of the detector modules

As a feasibility study of the use of MRPC as TOF-PET detector, a set of experiments have been performed. The experiments are mainly divided into two categories. In the following subsection the fabrication of bakelite-based MRPC will be discussed followed by the fabrication of glass-based MRPC in the next sub-section.

3.5.1 Bakelite-based MRPC

The technology mentioned in [48, 49] was used to build a two-gap and a four-gap Bakelite-based MRPCs. In the following subsections the constructions of the detectors will be discussed.

3.5.1.1 Two-Gap MRPC : Construction

A 30 cm. $\times$ 20 cm. two-gap bakelite-based MRPC having thickness of 2 mm. was constructed by procuring the bakelite from local market. The general steps that are used to construct the MRPC are as follows:

1. All the bakelite sheets were cleaned with alcohol.

2. For gas input and output, four nozzles (two on each side) were pasted diagonally, as shown in Figure 3.9 and Figure 3.10.

3. Uniform button spacers of polycarbonate material having diameter of 1 cm. and thickness of 2 mm. and edge spacers of the same material having dimension 30 cm $\times$ 0.8cm $\times$ 0.2 cm. were implanted for uniform gas spacing.

4. A thin coating of Silicone [48, 49] was applied on the surfaces of the bakelite to improve the surface smoothness.

5. The Silicone treated bakelites were kept under a heat lamp for several hours.

6. The MRPC module was leak-checked by Ar-He sniffer probes.

7. A graphite coating of resistivity 1 M$\Omega/\square$ was applied on the upper and lower surface of the bakelite sheets for uniform distribution of electric field over the detector.

8. Pick-up strips made of Copper and having dimensions of 30cm $\times$ 2.5 cm $\times$ 20 μm were placed above the graphite coated surface.

9. Copper strips were pasted on the surfaces for High Voltage(HV) connection.

10. Signals from different strips were sent through a ribbon cable, followed by coaxial cables using proper impedance matching.

The detector has been operated in streamer mode as it gives larger signal size and does not need any preamplifier. For the testing of the detector a mixture of Ar/i-butane/Freon(R134a)

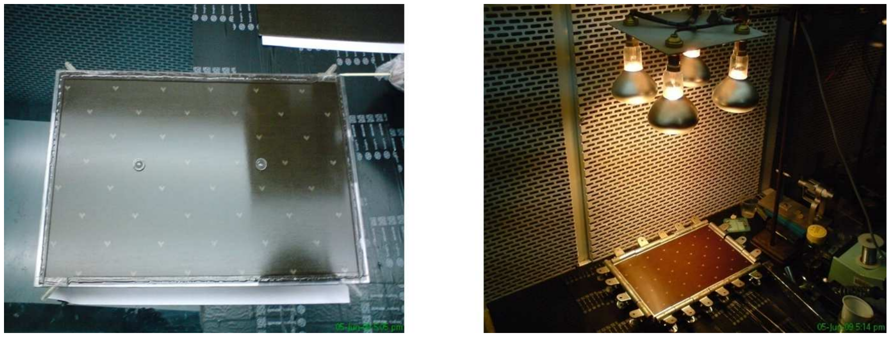

Figure 3.9: (Left:) Two-gap bakelite-based MRPC (Right:) Heat treatment to the detector after Silicone coating

Figure 3.10: Construction of two-gap MRPC

in the ratio of 55/7.5/37.5 was used as the working gas. For obtaining the signal from the detector proper impedance matching has been done.

3.5.1.2 Four-Gap MRPC : Construction

Figure 3.11 shows the construction of a four-gap MRPC. For this construction a grooving of perspex material of dimension 23 cm × 23 cm × 1 cm is made with proper gas inlet and outlet channel. The rest of the construction procedure is exactly same as discussed in subsection 3.6.1.1.

3.5.2 Glass-based MRPC

As a feasibility study we have also make an six-gap glass based MRPC having dimensions of 28 cm × 8 cm. The window glasses are procured from GSI, Germany having a thickness of 600

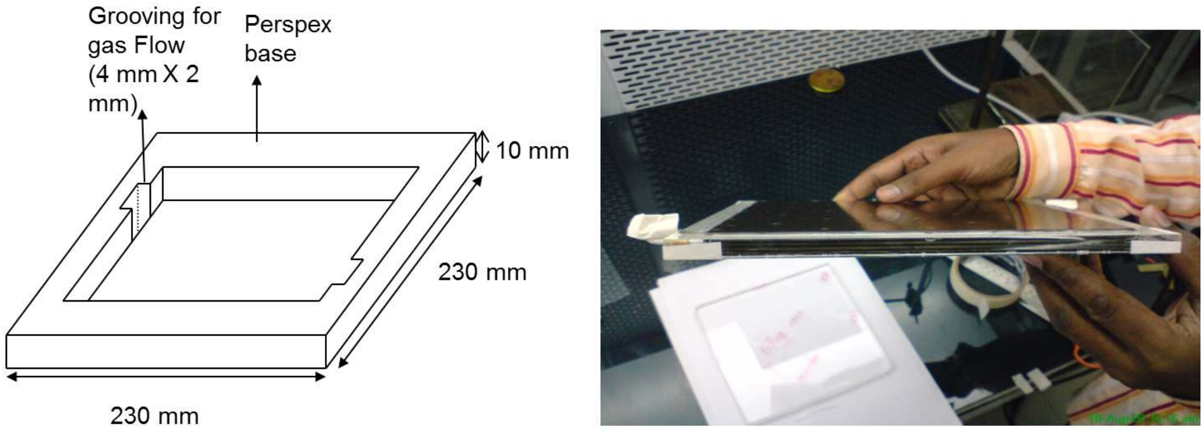

Figure 3.11: Construction of Four-gap Bakelite-based MRPC

μm. We have used G10 material having thickness of 200 μm as the gas gap. For the purpose of electrical conductivity through the detector we have used graphite paint as the conductive material. Figure 3.12 shows the typical step of construction of the detector.

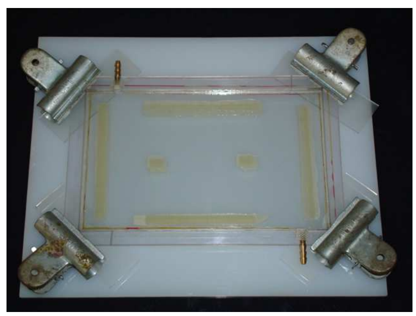

Figure 3.12: Construction of a six-gap glass based MRPC

To summarize the construction procedures of different detector modules a block diagram is shown in Figure 3.13.

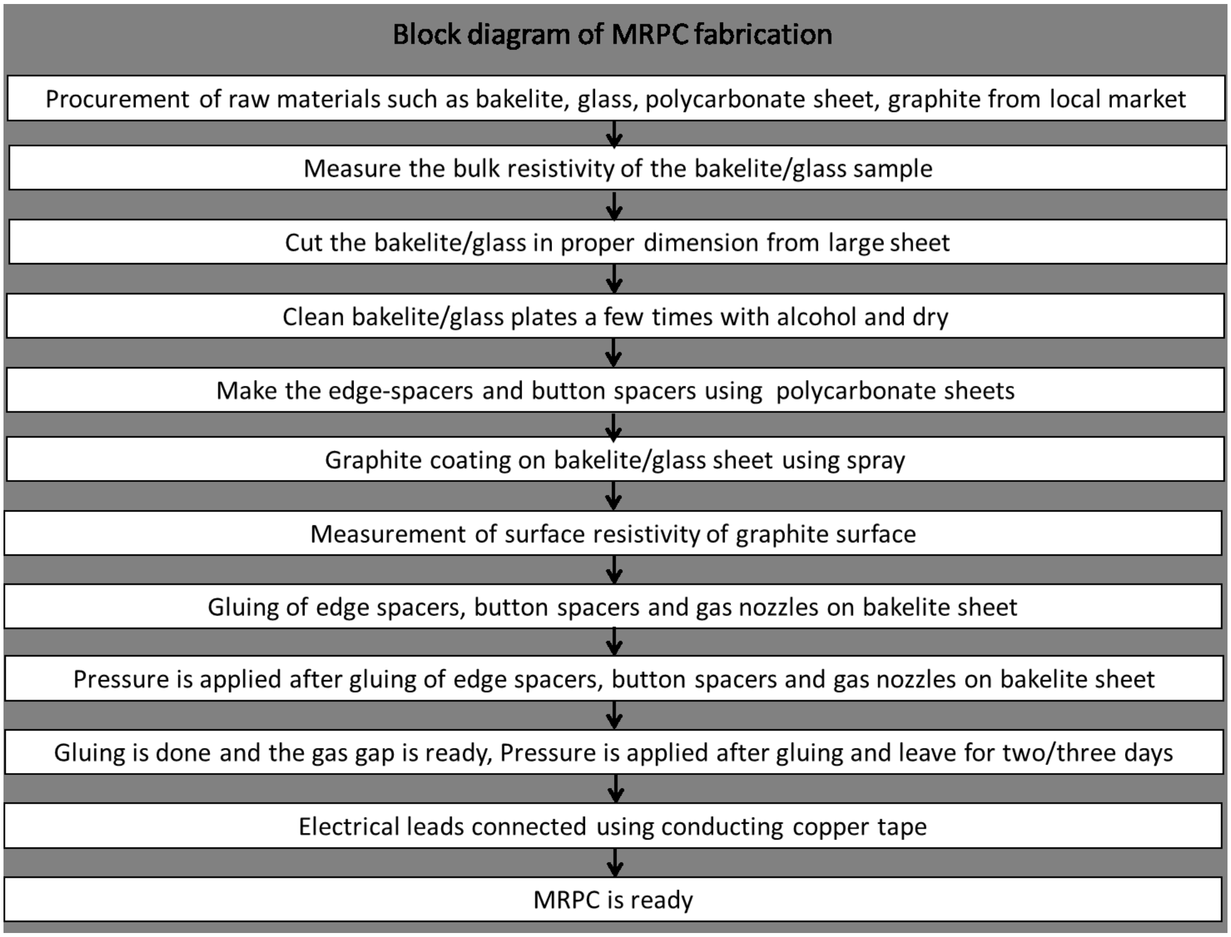

Figure 3.13: A schematic representation of the construction procedure of the detector modules

Also a comparative study of different parameters of these different detector modules are shown in Table 3.2.

Table 3.2: A comparative study of the different design parameters of the detector modules

No. of gaps	Detector material	Surface resistivity of the material	Dimensions	Gas gap
Two Gap	Bakelite	9×10^{13} Ω-cm	30 cm × 20 cm	2 mm
Four Gap	Bakelite	9×10^{13} Ω-cm	30 cm × 20 cm	2.5 mm
Six Gap	Glass	1.68×10^{13} Ω-cm	28 cm × 8 cm	0.2 mm

3.6 Testing of the detector modules

In this section the test results of the detector modules (both bakelite as well as glass made detectors) under cosmic ray will be discussed. For cosmic ray testing the following trigger scheme was used, as shown in Figure 3.14.

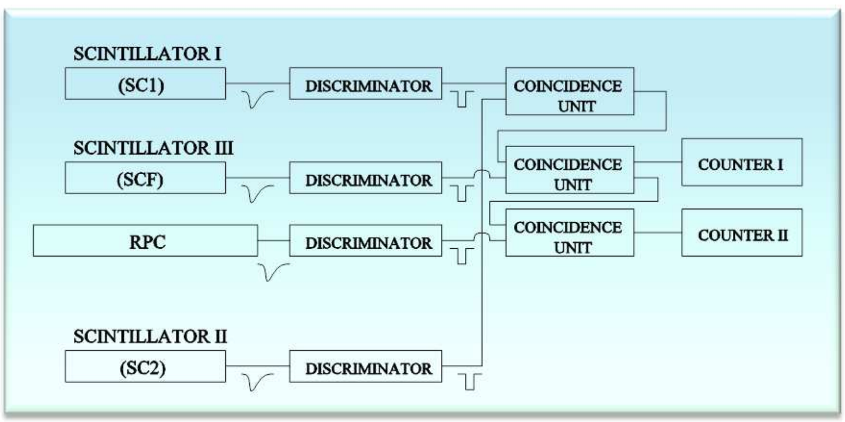

Figure 3.14: Schematic diagram of trigger used for Cosmic ray testing

The master trigger signal is defined by taking AND combination between Scintillator 1, Scintillator 2 and Finger Scintillator, i.e., **SC1.AND.SC2.AND.SCF**. For calculating the efficiency of the detectors the following formula has been applied

$$Efficiency = \frac{MRPC\ count\ in\ coincidence\ with\ master\ trigger}{Master\ trigger\ count} \quad (3.3)$$

and for measuring the time resolution of the detectors **START** signal is taken from master trigger and **STOP** signal is taken from MRPC.

For the testing of the modules a set of digital electronics had been used. A list of such electronic devices used is listed in Table 3.3.

Table 3.3: Different electronics components used for the testing of the detectors

Component	**Make**	**Model Number**
HV power Supply	CAEN	N471A
Leading Edge Discriinator	CAEN	N841
Counter Module	CAEN	N1145
Coincidence Unit	CAEN	N455
TDC	Philips Scientific	PS 7186

The double-gap and four-gap Silicone coated bakelite MRPC had been tested in the streamer mode with gas mixture Ar/iso-butane/R-134a = 55/7.5/37.5, whereas the six-gap glass based MRPC was tested in the avalanche mode with the gas mixture R-134a/iso-butane/SF_6 = 95/4.5/0.5. The high voltage to the MRPCs were applied at the ramping rate of 5 V/s on both the electrodes for both types of detectors. The streamer pulses for the bakelite based MRPCs were obtained starting from the high voltage of 5 kV across the MRPCs. The high voltage was applied to some of the MRPCs by using the CAEN Mod.N470 unit and to the others using the CAEN Mod.N471A unit. The leakage current as recorded by the high voltage system was studied. Also during the study various characteristic parameters of the detector modules like efficiency, time resolution, charge spectrum, effect of threshold on efficiency etc. had been measured. The Philips Scientific leading edge discriminators (Model 708) were used for the scintillators and the MRPC pulses. Various thresholds were used on the discriminators to reduce the noise. For the final results, a threshold of 40 mV was used on the MRPC signal. A CAMAC-based data acquisition system, LAMPS, developed by Electronics Division, Bhabha Atomic Research Centre, Trombay, India had been used. Counts accumulated in a CAEN (Model 257) scalar over a fixed time period were recorded at regular intervals, and saved in a periodic log database. The temperature and the humidity were also monitored at a regular interval of time during the measurements. For the testing of Bakelite-based detectors no preamplifier has been used, as the signal size is large enough to detect.

In the next subsection the test results of two bakelite based MRPC will be discussed followed by the performance of the six-gap glass based MRPC.

3.6.1 Bakelite based MRPC

3.6.1.1 Two-Gap MRPC

Figure 3.16 shows the variation of current and efficiency of the detector as a function of high voltage. Figure 3.16(a) clearly shows two distinct slopes of current, first part of which is generated due to the influence of spacers and second part of which is generated due to gas mixture. The reason for these two distinct slopes can be understood by considering an electrical eqivalent circuit of a RPC, as depicted in Figure 3.15 [48].

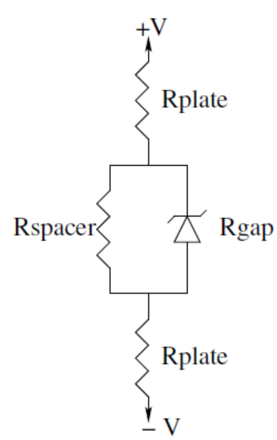

Figure 3.15: An electrical equivalent circuit for RPC

At low value of the volatge applied

$$
\begin{aligned}
&Resistance_{gap} = \infty, \qquad Resistance_{spacer} \gg Resistance_{plate} \\
&\frac{dV}{dI} = Resistance_{spacer}
\end{aligned}
$$

which implies that the gas gap behaves as an insulator in the lower range of the voltage applied and the slope in the lower range of voltage indiates the conductance of the spacers used.

At high value of the voltage applied

$$
\begin{aligned}
&Resistance_{gap} = 0 \\
&\frac{dV}{dI} = Resistance_{plate}
\end{aligned}
$$

indicating that at high volatge the gas gap behaves as a conducting medium and the slope at this range of high voltage refers to the conductance of the gas gap. As calculated from the figure the resistivity of the spacers is around $2.66 \times 10^{13}\Omega$ cm. and that of the Bakelite is around $9 \times 10^{12}\Omega$ cm. An efficiency plateau of $\sim 90\%$ was obtained for the detector from a voltage of 13.5 kV and above, as depicted by Figure 3.16(b).

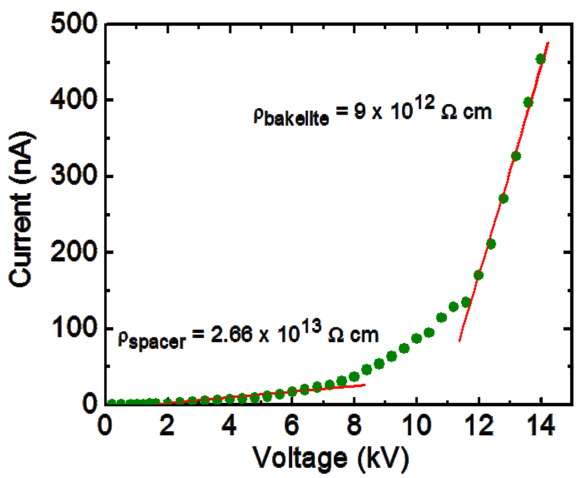

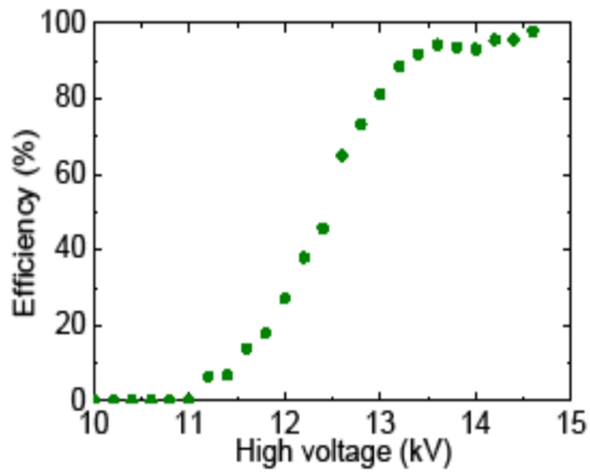

Figure 3.16: For two-gap MRPC (a) Current versus High Voltage (b) Efficiency versus High Voltage

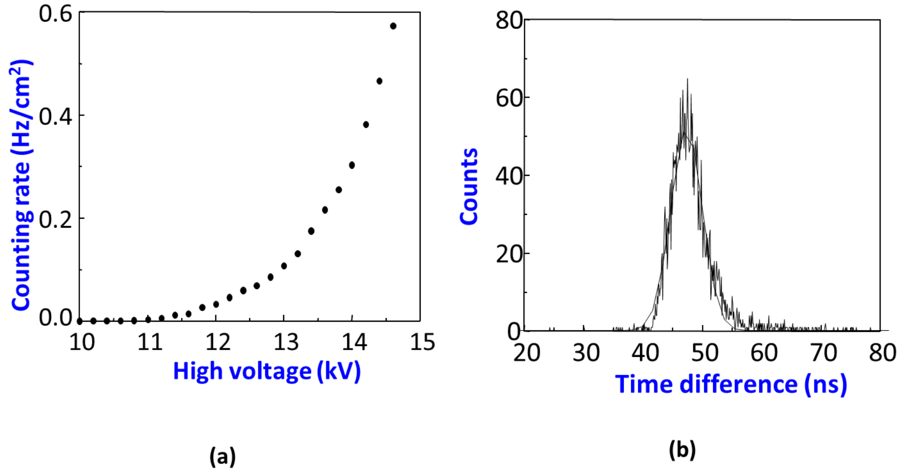

Figure 3.17: For two-gap MRPC (a) Count Rate High Voltage (b) Time spectrum of the detector

In Figure 3.17(a), the variation of counting rate vs high voltage is shown, which as expected to be increasing with the voltage. A typical time spectrum is also shown in Figure 3.17(b).

Time resolution σ is the combination of time resolution of the scintillator and the MRPC. From this value the intrinsic time resolution of the MRPC is calculated by the formula

$$\sigma^2 = \sigma_{sc}^2 + \sigma_{MRPC}^2 \tag{3.4}$$

where σ_{sc} is the intrinsic time resolution of the scintillator used and σ_{MRPC} is that of the MRPC.

In Figure 3.18 time resolution (Full Width at Half Maximum or FWHM) and time delay as calculated from the experiment is plotted against high voltage for the two-gap detector. At around 14.5 kV the time resolution(σ) had been measured to be $\sim$ 2 ns.

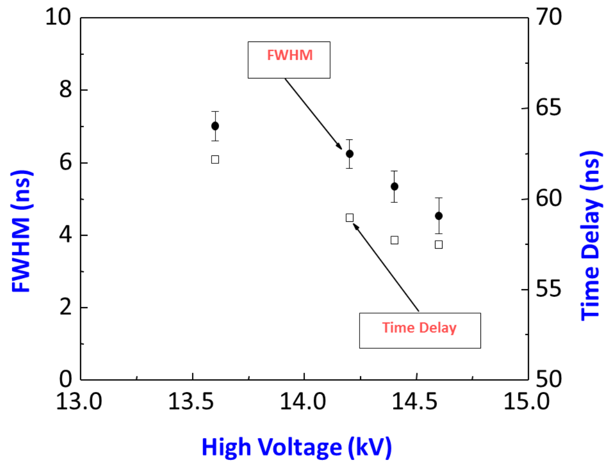

Figure 3.18: Time resolution (FWHM) and time delay versus High Voltage for two-gap MRPC

3.6.1.2 Four-Gap MRPC

A typical signal as obtained during the experiment is shown in Figure 3.19.

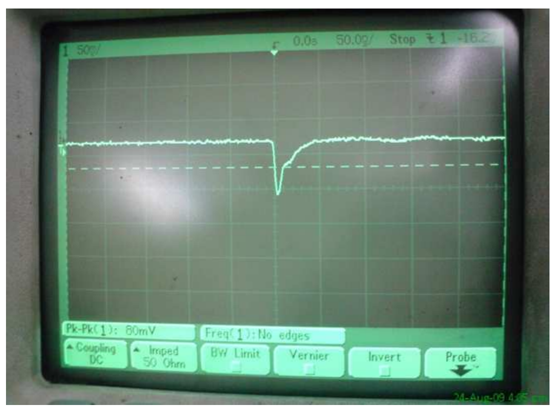

Figure 3.19: Signal from the Four-gap Bakelite-based MRPC(∼50 mV after using threshold)

Figure 3.20(a) shows the current and Figure 3.20(b) efficiency as a function of high voltage as obtained in the experiment.

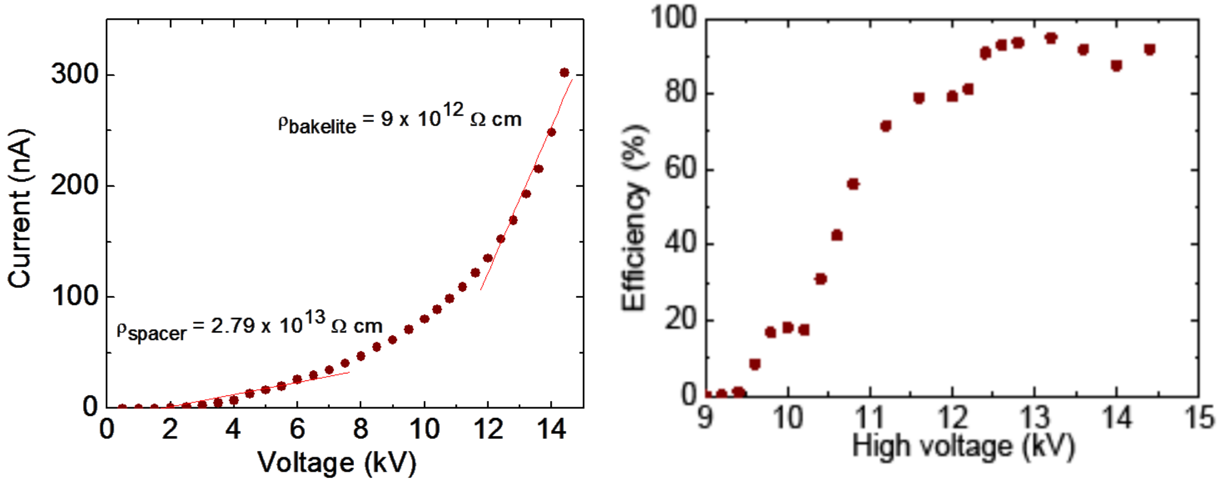

Figure 3.20: For four-gap MRPC (a) Current vs. HV (b) Efficiency vs. HV

The resistivity of the Bakelite material and spacers are 9×10^{12} Ω-cm and 2.66×10^{13} Ω-cm respectively. A maximum efficiency of 90% is obtained for a high voltage of 12.5 kV,as depicted in Figure 3.20(b).

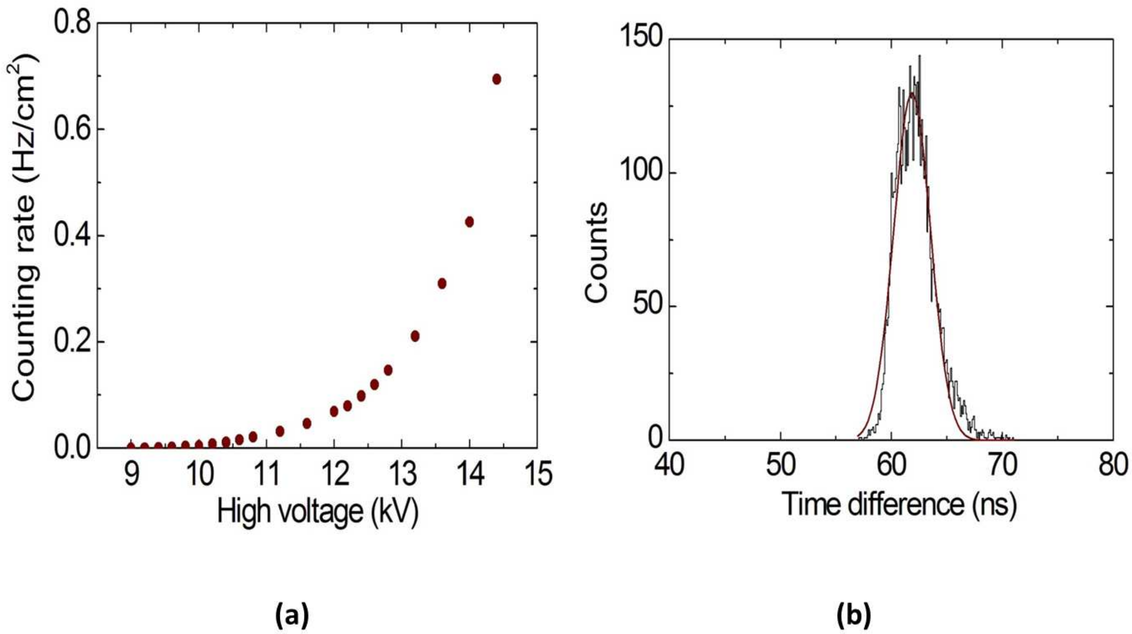

Figure 3.21: For four-gap MRPC (a) Count rate vs. HV (b) Histogram for time difference

Figure 3.21(a) shows the counting rate of the detector versus the high voltage applied to it, and Figure 3.21(b) shows the distribution of the time difference as obtained in the experiment.

In Figure 3.22 we have plotted the FWHM and time delay measured by the detector as a function of high voltage. It is clearly seen from the figure that a minimum time resolution of 2 ns (FWHM) or σ= 850 ps can be achieved at a high voltage value of 13 kV.

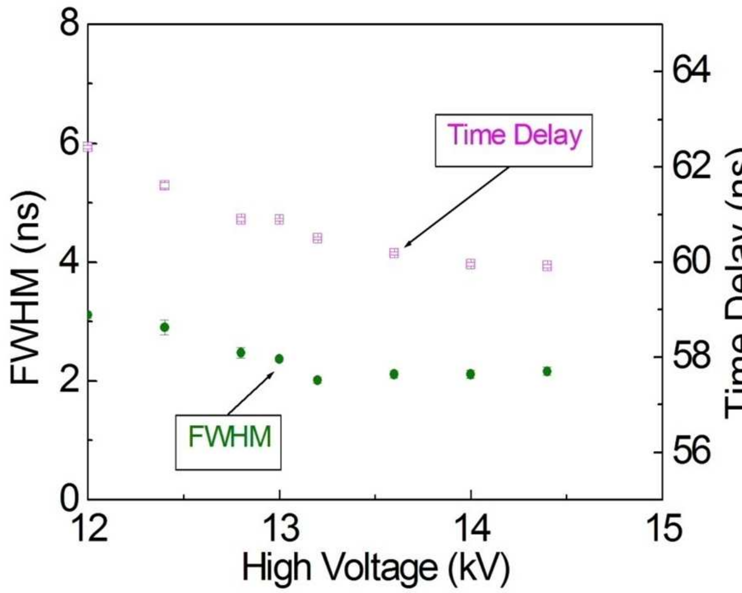

Figure 3.22: FWHM and time delay as a function of high voltage for four-gap MRPC

3.6.2 Glass based MRPC

3.6.2.1 Six gap MRPC

In Figure 3.23 the variation of leakage current against high voltage is plotted. It is found that there is a smooth increase in current with respect to voltage. Such a variation may be observed because of the increase in the gas gap number. It is concluded from the figure that the resistivity of the glass material, procured from Germany, seems to be $1.68 \times 10^{13}\Omega$ -cm. It is to be understood that the current does not saturate at any voltage.

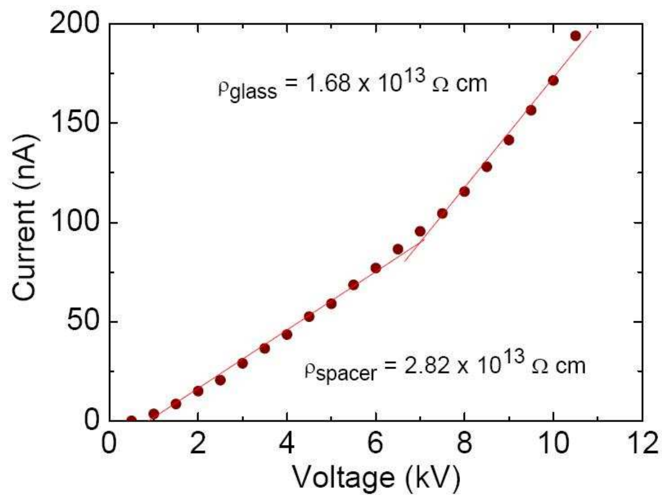

Figure 3.23: Variation of leakage current as a function of High Voltage for six-gap MRPC

If we compare Figure 3.20(a) and Figure 3.23, we can conclude that the surface resistivity of glass material is one order higher than that of the Bakelite.

In Figure 3.24 we have shown the variation of count rate and efficiency as a function of threshold applied. The plot shows that both the parameters decrease as threshold is increased.

In Figure 3.25(a) we have shown the distribution of charge deposition by cosmic rays as obtained in the experiment. It is best fitted with **Polya** distribution for which the parameters are shown

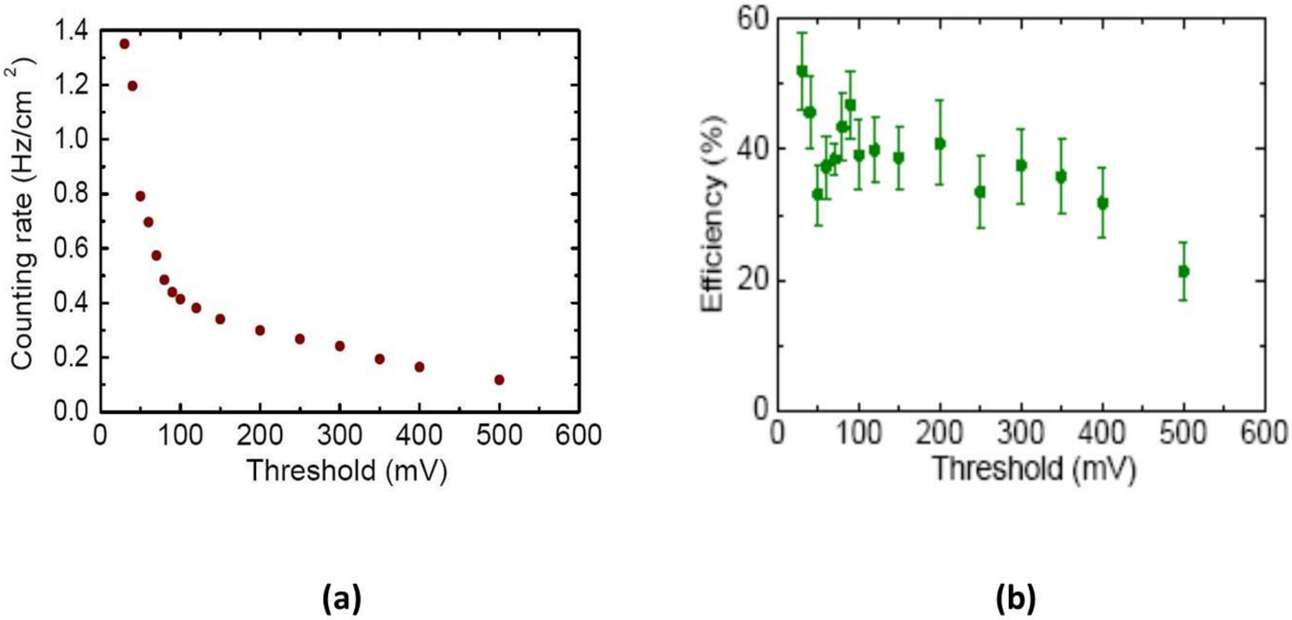

Figure 3.24: Variation of (a) counting rate and (b) efficiency as a function of threshold for six-gap MRPC

in the figure. The mean of the charge spectrum is found to be around 6 pC. In Figure 3.25 (b) the variation of mean charge as a function of high voltage is shown.

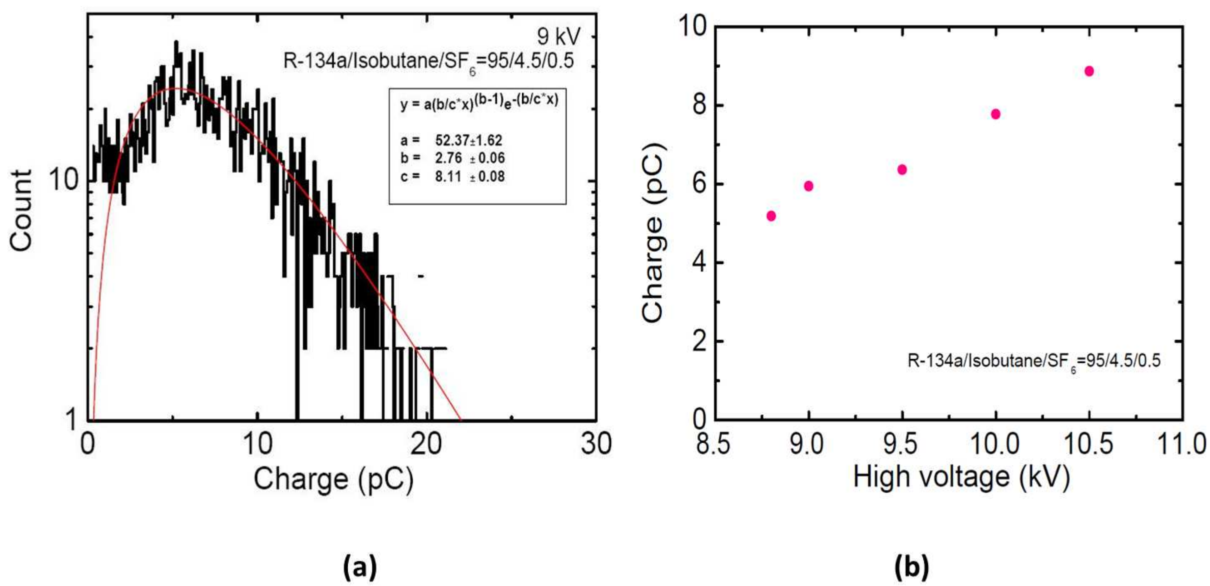

Figure 3.25: (a) Charge spectrum (b) Variation of charge as a function of High Voltage for six-gap MRPC

In Figure 3.26 a typical plot of time distribution is shown. For calculating the intrinsic time resolution of the detector again the formula given in Equation 3.3 had been used and the time resolution (σ) is found to be around 410 ps.

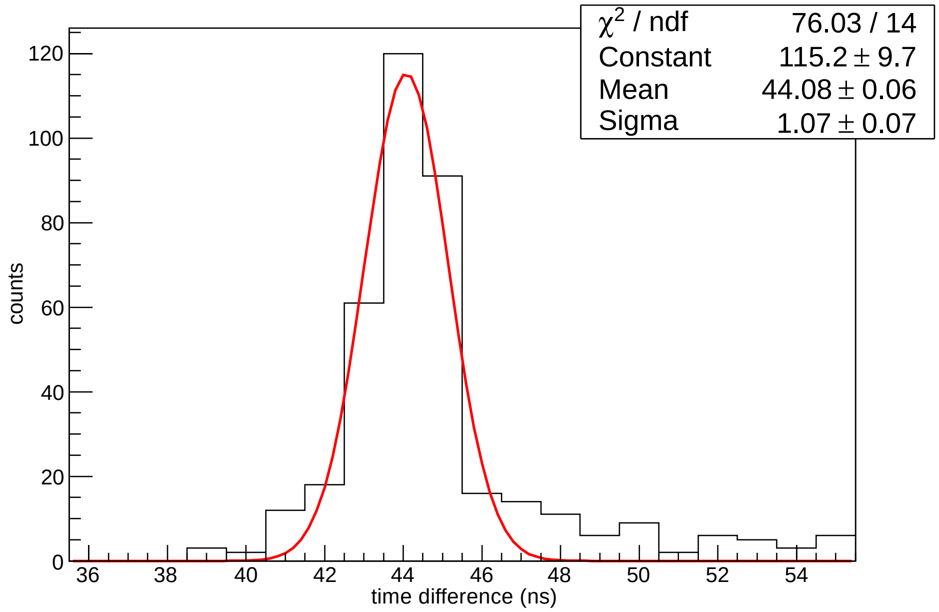

Figure 3.26: Time distribution as obtained for six gap glass MRPC

In Figure 3.27 (a) the time resolution (σ) as a function of high voltage has been plotted, which shows a typical value of 410 ps as the time resolution of the detector within statistical error bars. In Figure 3.27 the time delay measured by the detector is shown as a function of high voltage, which clearly shows the consistency of the results with respect to high voltage.

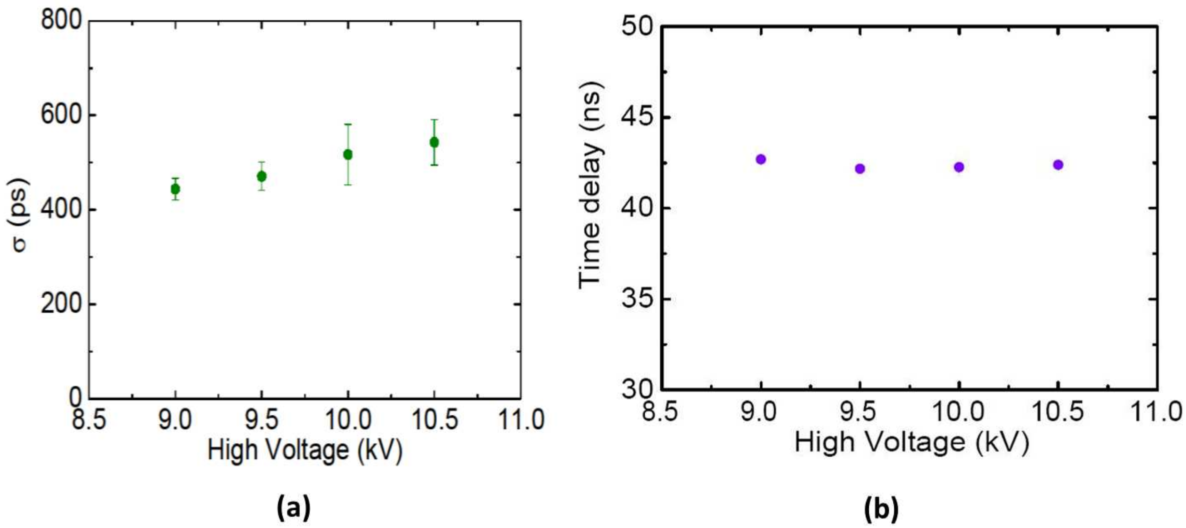

Figure 3.27: For six-gap MRPC (a) Time resolution vs. high voltage (b) Time delay vs. high voltage

3.6.3 A feasibility study of the glass-based six-gap MRPC as a probable detector for PET imaging

For the measurement of the efficiency of detection of photon-pairs for $e^+ - e^-$ annihilation, a feasibility study had been performed. As shown in Fig 3.28 a ^{22}Na source having activity of 10 μCurie and emitting two almost back-to- back 511 keV photons had been placed in between a plastic scintillator of dimension 5 cm $\times$ 1.2 cm and the MRPC.

An important discussion regarding the ^{22}Na source is worth mentioning at this stage. ^{22}Na source of such activity is also able to emit 1.2 MeV photons. During this study of photon detection efficiency by the detector the contribution from 1.2 MeV photons had not been rejected explicitly. Although it is important to mention that the efficiency obtained during this study should be reduced to 25% of the present value obtained after correcting the effect of 1.2 MeV photons [50].

For coincidence measurement the signals from the scintillator and the MRPC strips were used with and without the ^{22}Na source. A sharp increase of coincidence count rate with the applied high voltage was observed and the effect of the source is clearly seen from Figure 3.29.

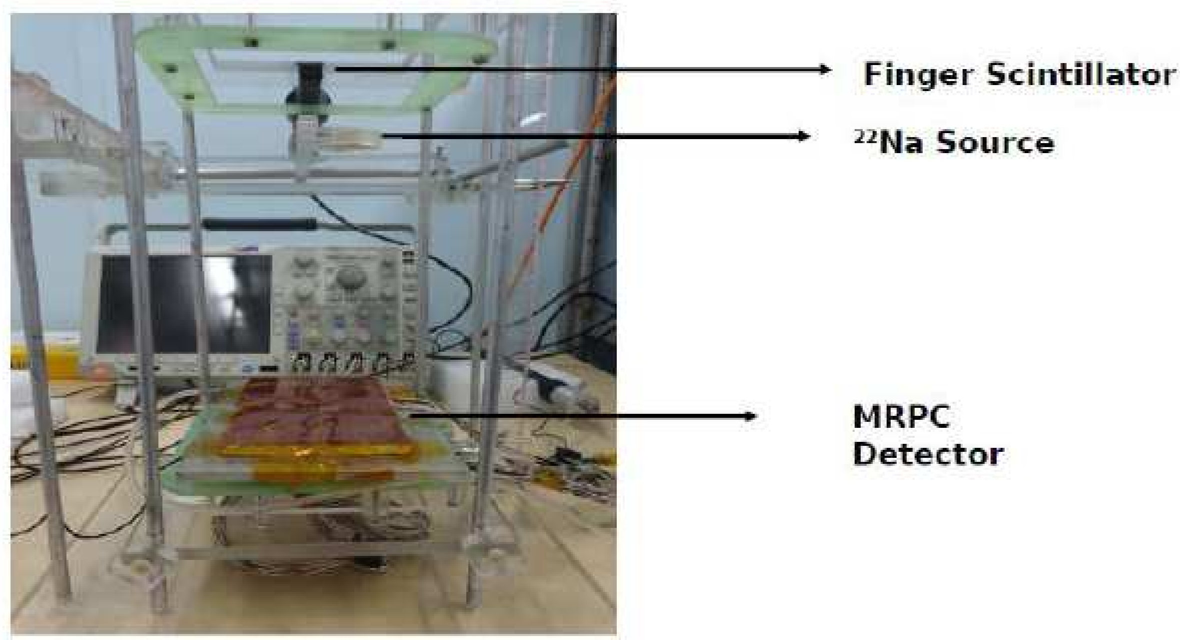

Figure 3.28: Experimental set-up for annihilating photon pair detection efficiency

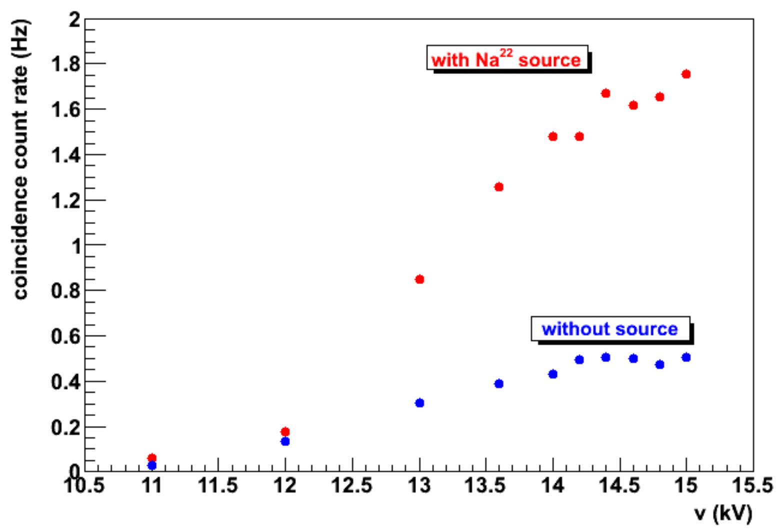

Figure 3.29: Coincidence count rate vs. high voltage

The photon-pair detection efficiency is defined as the ratio of the two fold coincidence counts between the scintillator signal and the MRPC signal to the number of photons counted by the scintillator only. From Figure 3.30 it is clearly seen that the efficiency increases with high voltage. The pair-detection efficiency of 0.9% has been obtained for an applied voltage of 15 kV after the corrections for geometry.

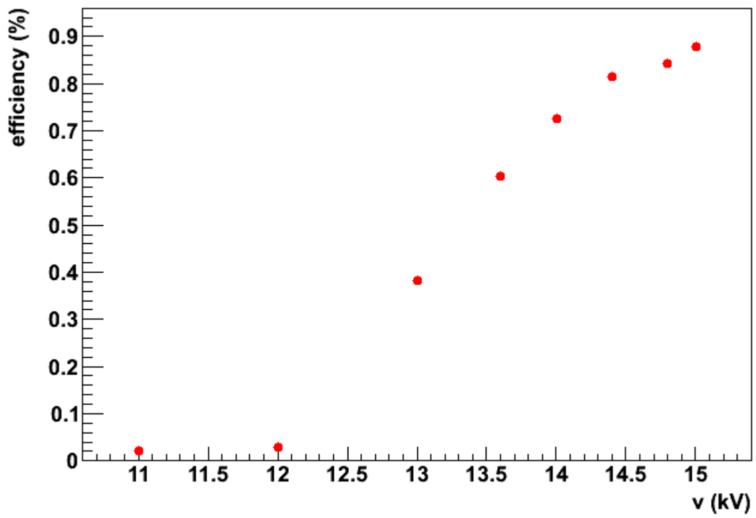

Figure 3.30: Efficiency rate vs. high voltage

To locate the position of the source, the time difference between the signals on the scintillator and the MRPC was measured. The start and the stop signals have been obtained from the scintillator and the MRPC respectively. The distance between the scintillator and the MRPC has been fixed at 44.5 cm. The distance of the source has been measured from the MRPC. The time difference has been calculated as distance/30 - (44.5-distance/30), where the velocity of the photons has been taken as 30cm/nsec.

In Figure 3.31 the time difference spectrum for the different positions of the source has been shown. From this figure the time resolution of the detctor has been extracted for different positions. The spectra are plotted after subtracting the delay applied to the electronics (123 ns in this case).

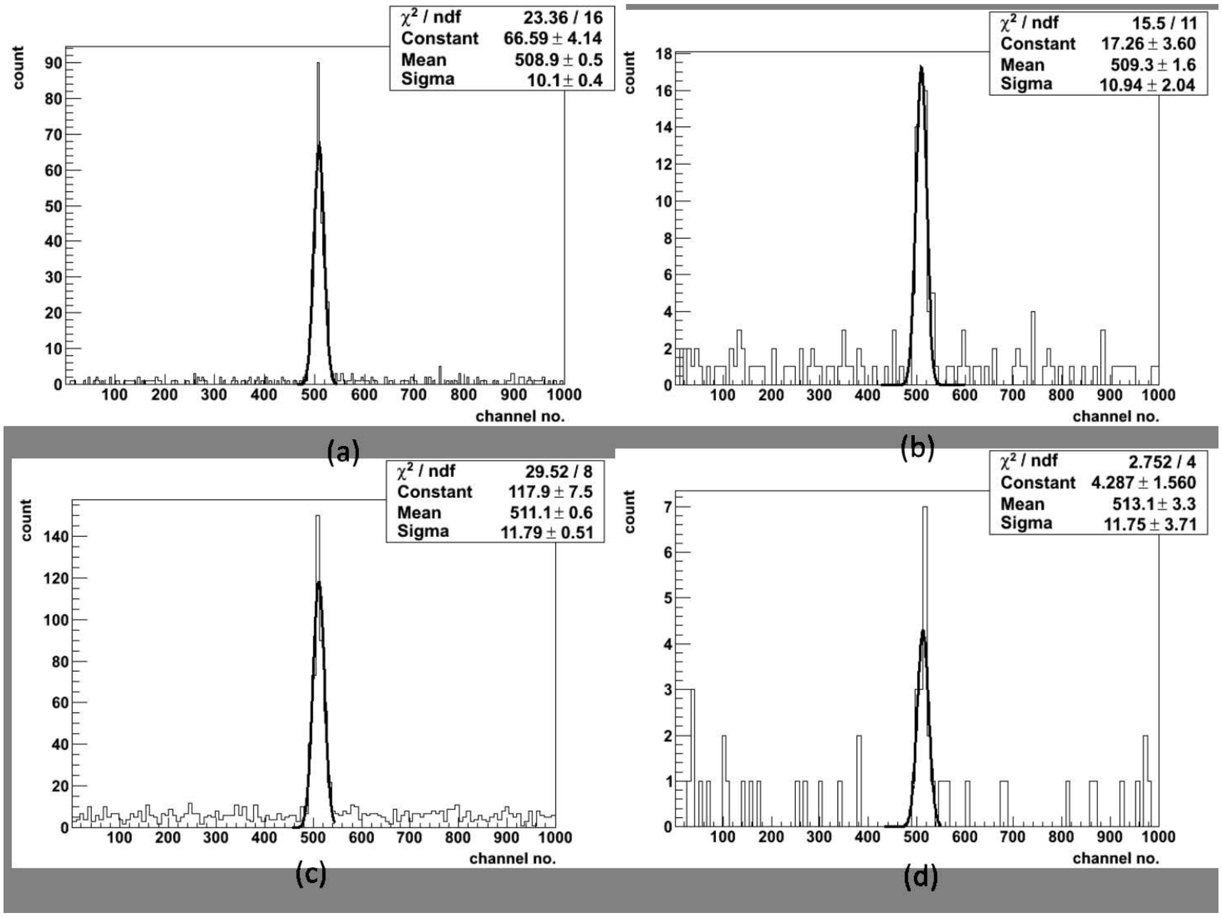

Figure 3.31: Time difference spectrum as obtained by shifting the source positions ; (a) source at 34.5 cm, (b) source at 37.4 cm, (c) source at 41 cm, (d) source at 41.5 cm

It is seen from Figure 3.32, that given the large error bars, by varying the source position, the time difference between the signals from the trigger scintillator and the MRPC is changing in an expected direction. The expected time difference from the measured distance has also been shown in Figure 3.32 by red dots.

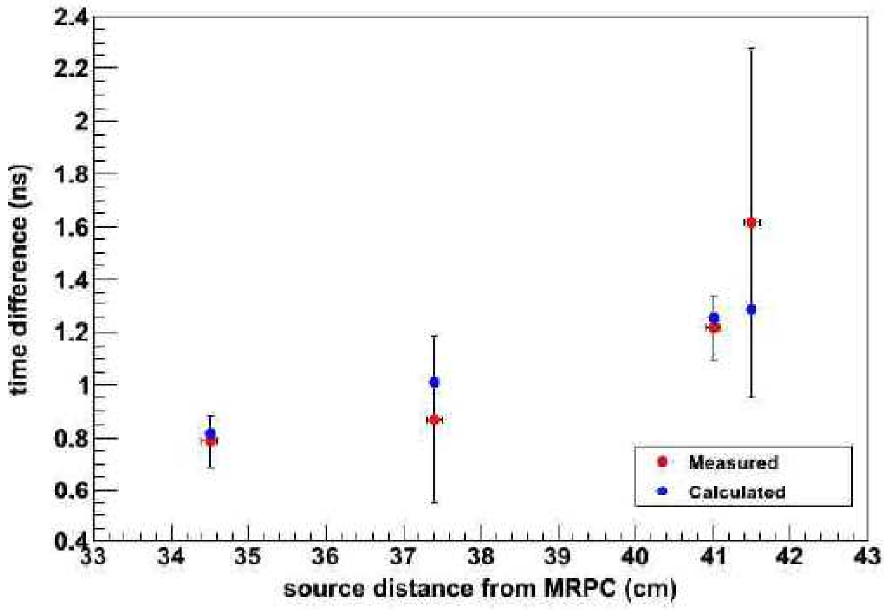

Figure 3.32: Time difference as a function of source distance

3.7 Summary

In this chapter the detailed simulation and performance of several MRPC system has been discussed which concludes that MRPC-based TOF-PET system is potentially an attractive alternative to the expensive scintillator-based system. In performed simulation for the detection of photon pairs by a converter-based layered RPC system the photon conversion efficiency was increased up to a saturated value of 30% for a 120 gap configuration. The simulated time resolution for the pair detection had been obtained to be 19 ps, which is considerably better that reported experimentally. The non-inclusion of several effects in simulation like, readout electronics, back-scattered electrons among others might be the reason of such a good time resolution. A six gap glass-based MRPC has been tested with photon pairs from ^{22}Na source. A clear signal of photon pairs above background in presence of source as detected by a scintillator and MRPC coincidence had been observed.

Chapter 4

Application in High Energy Physics: STAR Muon Telescope Detector (MTD)

4.1 Heavy Ion Collision

As depicted in Figure 4.1, in a convensional model of reltivistic heavy ion collision, travelling at 99.95% the speed of light, the saturated partonic matter appears flat, instead of spherical, due to Lorentz contraction which occur at such speeds. Then the matters collide, smashing into one other and then passing through each other to form highly dense gluonic states at intial step. This inital stage evolves through a stage of strongly correlated Quark Gluon Plasma (sQGP) state, followed by a transition to hadronic matter and finally the generation of new particles.

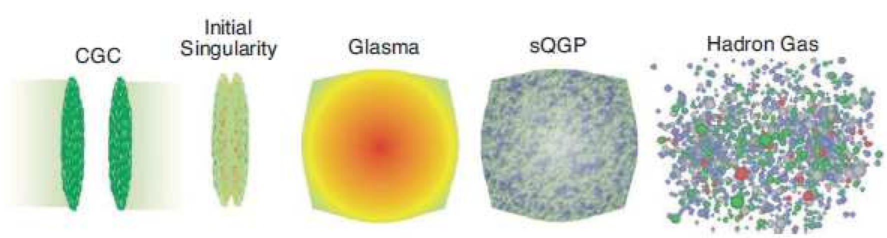

Figure 4.1: Schematic of heavy ion collision, a figure by S. Bass

If conditions are right, the collision "melts" the protons and the neutrons and for a brief instant, liberates the quark and the gluons. Just after the collision, thousands more particles form as the area cools off. Each of the particles provides a clue as to what occurred inside the collision zone.

The most important stage of the evolution is the phase transition from QGP state to hadronic matter state. The hadronic matter expands till the expansion rate exceeds the scattering rate of the different constituent particles. Finally these constituents can flow freely in 4π directions to the detectors.

4.2 Quark Gluon Plasma(QGP)

The quark-gluon plasma contains quarks and gluons, just as normal baryonic matter does. The difference between these two phases of QCD is that in normal matter each quark either pairs up with an anti-quark to form a meson or joins with two other quarks to form a baryon (such as the proton and the neutron). In the QGP, by contrast, these mesons and baryons lose their identities and dissolve into a fluid of quarks and gluons, creating a deconfied systems of quarks and gluons. As a result of colour confinement, this system of quarks and gluons cool down and undergo a phase transition to the hadronic matter system. The phase transition from QGP to hadronic matter is associated with spontaneous breaking of chiral symmetry. The spontaneous breakdown of chiral symmetry generates mass at the Quantum Chromodynamics (QCD) scale. In QGP phase where the chiral symmetry is restored, the quarks get melted and the QCD masses of the light quarks disappear. Lattice QCD calculations show that for vanishing baryon densities such transition is a crossover within a temperature range of $T_c \sim$ 150-200 for physical quark masses [51]. Again the QCD based models [52, 53] predict the transition at high baryonic densities to be of first order. The end point of such a first order phase transition is known as QCD critical point (CP). Both different theories [54] and experiments like heavy ion collision at Relativistic Heavy Ion Collision (RHIC) at STAR or Large Hadron Collider (LHC) experimnt are trying to establish the existance and the location of QCD CP. These phenomena will give rise to a phase diagram as depicted by Figure 4.2.

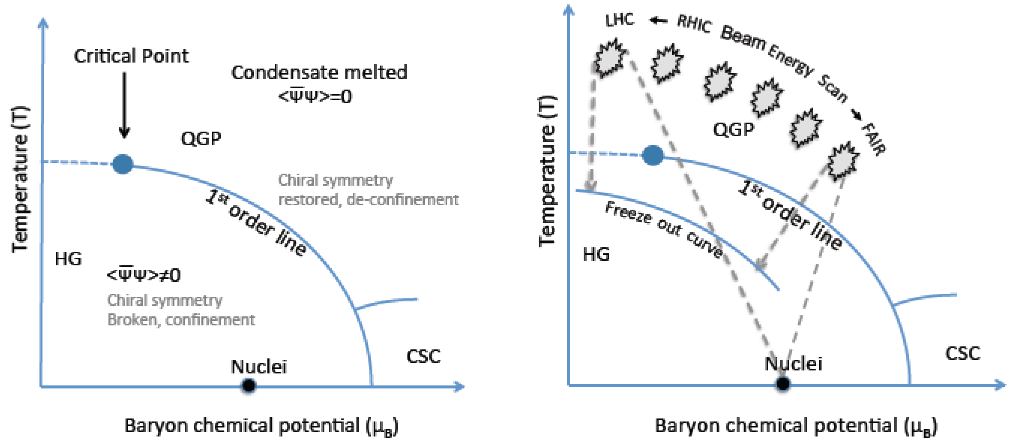

Figure 4.2: Proposed schematic of the QCD phase diagram, left figure shows theoretical predictions and right figure shows the trajectories of heavy ion collisions.

The QCD phase diagrams are plotter generally in terms of two thermodynamic variables: temperature (T) and the baryonic chemical potemtial (μ_B). The left part of Figure 4.2 shows the theoritically proposed phases, the lines of phase transitions. The right part of Figure 4.2 shws the possible trajectories of the matter in heavy ion collision experiments for different colliding energies. According to the diagram it is important to mention that the higher collision energies correspond to higher temperature and lower chemical potential. The chiral phase transition line is shown by a blue curve which is a first order line at large μ_B that ends with a critical point (CP) for physical quark masses. Beyond the CP at very low μ_B, the cross over between the QGP phase and the Hadronic Matter is represented by a dotted line.

Although the experimental high temperatures and densities predicted as producing a quark-gluon plasma have been realized in the laboratory, the resulting matter does not behave as a quasi-ideal state of free quarks and gluons, but rather, as an almost perfect dense fluid. Actually the fact that the quark-gluon plasma will not yet be "free" at temperatures realized at present accelerators had been predicted already in 1984 as a consequence of the remnant effects of confinement.

A plasma is a matter in which charges are screened due to the presence of other mobile charges; for example - Coulomb's law is modified to yield a distance dependent charge. In a QGP, the colour charge of the quarks and the gluons is screened. The QGP has another analogy with a normal plasma. There are also dissimilarities because the colour charge is non-abelian, whereas the electric charges are abelian. Outside a finite volume of QGP the colour electric field is not screened, so that the volume of QGP must still be colour-natural. It will therefore, like a nucleus, have integer electric charge.

4.3 STAR Detector

The detector layout is shown in Figure 4.3. In the following sub-sections a brief description of the major components of STAR will be discussed.

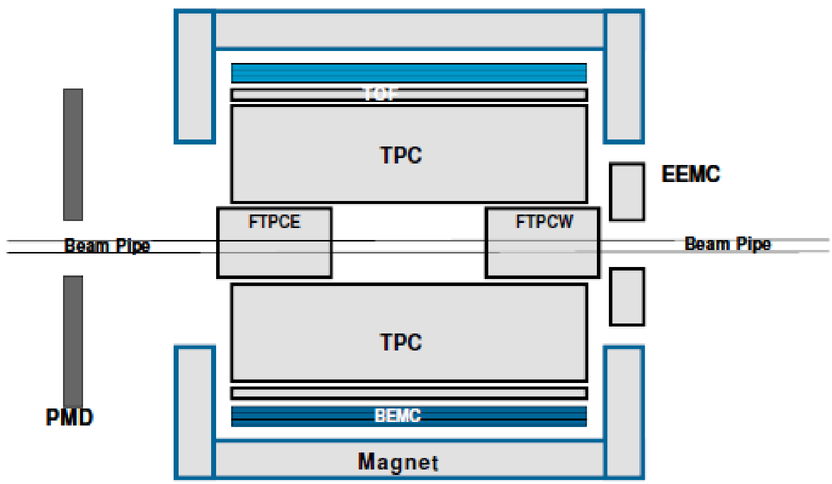

Figure 4.3: Schematic view of the STAR detector.

4.3.1 Time Projection Chamber

The main tracking device is the Time Projection Chamber (TPC) [55], whose inner and outer field cages are located at radial distances of 50 and 200 cm respectively from the beam axis. The TPC covers a pseudorapidity range $|\eta| < 1.8$ and 2π in azimuth. The gas mixture used in this detector is CH_4:Ar = 10%:90% at 2 mbar pressure [56]. This 4.2 meter long TPC sits inside the large solenoidal STAR magnet which produces 0.5 T magnetic field [57]. The read out pads of TPC are made of Multi Wire Proportional Chambers (MWPC) and placed at end cap of the chamber on both sides. The ionization energy loss (dE/dx) is used for particle identification [58],[59],[60]. A more detail descripction of TPC can be found in Reference [61].

4.3.2 Time of Flight Detector

The Time of ight (TOF) detector system at STAR is made of two subsystems, one called the pseudo-vertex position detector (pVPD) and Time of Flight Patch (TOFp). pVPD provides the start time and TOFp provides the stop time for the particle time of ight measurements. There are two pVPDs which are positioned very close to the beam pipe on both side of the collision point outside the STAR magnet. Along with the start time of TOF, the two VPDs also provide the z-component of the vertex position of a collision. A TOF detector based on Multi-gap Resistive Plate Chambers (MRPC) [62] was fully installed in STAR in 2009, covering 2π in azimuth and -1< η <1 in pseudorapidity at a radius of about 220 cm. It will extend particle identification up to p_T of about 3 GeV/c for p and $\bar{p}$ [63]. A detailed description of TOF can be found in Reference [64].

4.3.3 Electromagnetic Calorimeter

The full barrel electromagnetic calorimeter (BEMC) is installed outside the TOF radius and uniformly covers -1< η <1 in pseudorapidity and 2π in azimuth [65]. The TPC is centered in a solenoidal magnetic field provided by the surrounding magnetic coils. The return flux path for the field is provided by the magnet steel [66], which is roughly cylindrical in geometry and consists of 30 flux return bars, four end rings, and two pole tips. The 6.85 m long flux return bars are trapezoidal in cross-section and 60 cm thick with a 363 cm outer radius. The width at the outer radius of the return bar is 57 cm. Details of electromagnetic calorimeter can be found in Reference [67, 68].

4.3.4 Photon Multiplicity Detector

Photon Multiplicity Detector (PMD) is a pre-shower detector designed to measure event-byevent photon multiplicity in the pseudorapidity region of -3.7 < η < -2.3. It is located 5.4 meter away from the collision point along the beam axis outside the STAR magnet. PMD consists of a highly granular (41,472 cells in each plane) pre-shower plane placed behind a lead converter of 3 radiation length thickness. A second detector plane called the charged particle veto (CPV) identical in granularity and dimension with the pre-shower is placed before the lead plate. They work on the principle of gas proportional counters with a sensitive medium of Ar and CO2 in a weight ratio of 70:30. Detailed description of the PMD can be found in Reference [69].

4.4 Muon Telescope Detector(MTD)

As documented by the data taken over several experiments [70], Relativistic Heavy Ion Collision (RHIC) is able to create dense as well as rapidly thermalizing matter which can be characterized by a) initial energy densities far above the critical values predicted by lattice QCD for formation of QGP b) opacity to jets and c) nearly ideal fluid flow. One of the many important properties of this partonic matter created at RHIC is the colour screening. Due to colour screening, different quarkonium states will dissociate, and the dissociation temperatures will be different due to different binding energies. The measurement of transverse momenta of quarkonia for different centralities, collision systems, and energies will behave as a thermometer of the QGP. A large-area Muon Telescope Detector (MTD) at mid-rapidity collisions has been built in STAR for advancing the knowledge of QGP properties. Since muons do not participate in strong interactions, they provide penetrating probes for the strongly interacting QGP. A large area detector identifying muons with momentum of a few GeV/c at mid-rapidity allows for the detection of di-muon pairs from QGP thermal radiation, quarkonia, light vector mesons, possible correlations of quarks and gluons as resonances in the QGP and Drell-Yan production, as well as the measurement of heavy flavor hadrons through their semi-leptonic decays into single muons [71, 72]. In addition, electron-muon correlations can be used to distinguish between lepton pair production and heavy quark decays ($c+\bar{c} \rightarrow e+\mu(e), B \rightarrow e(\mu)+c \rightarrow e+\mu(e)$) and also muons are less affected by Bremsstrahlung radiation energy loss in the detector material than electrons, thus providing excellent mass resolution of vector mesons and quarkonia. This is essential for separating the ground state (1S) of the Υ from its excited states (2S+3S). They are predicted to melt at very different temperatures.

Unlike other conventional muon detecors which are based on particle tracking, the MTD is able to identify muons of momentum of a few GeV/c [73] using its intrinsic time resolution of < 100 ps and spatial resolution of ~ 1 cm. Multi-gap Reistive Plate Chamber with large modules, long strips and double-ended readout (LMRPC) is used as MTD detector.

A thorough Monte Carlo simulation study had been performed for the identification of muons by MTD detectors and for finalizing the detector structure. The simulation involves full HIJING central Au+Au collision with full STAR geomentry, as shown in Figure 4.4.

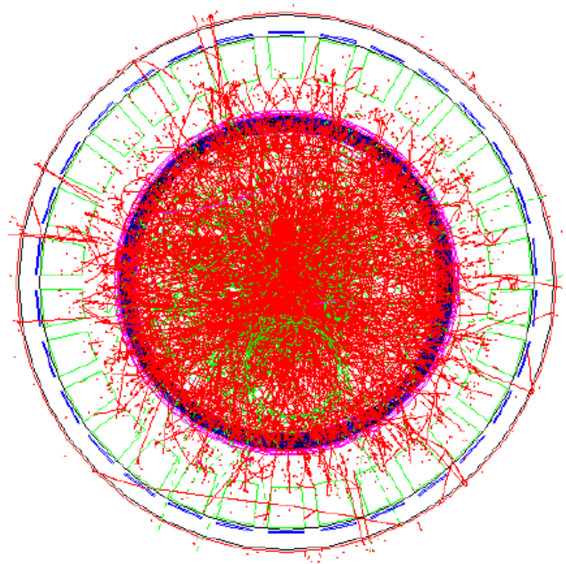

Figure 4.4: A full HIJING central Au+Au collisions simulated in STAR

For the simulation the muon detectors (in blue colour in Figure 4.4) have been considered to cover the full return bars (in green colour in Figure 4.4) within $|\eta| < 0.8$ and to uncover the gaps between the return bars. The detctors have also been considered to have an acceptance of 56% of 2π in azimuth. As seen in Figure 4.4, most of the particles are stopped before the BEMC and the few primary or secondary particles mainly come through the gaps between the return bars. In the simulation, the charged tracks that were reconstructed in the TPC have been extrapolated to the MTD, and were required to match the hit position and the time-of-flight from MTD measurements. It has been repoted [74] in the simulation that for a muon with

$p_T > 2$ GeV/c generated at the center of TPC, the detection efficiency of the MTD detctors is 40-50%, while for pions the efficiency is reported to be around 0.5-1%.

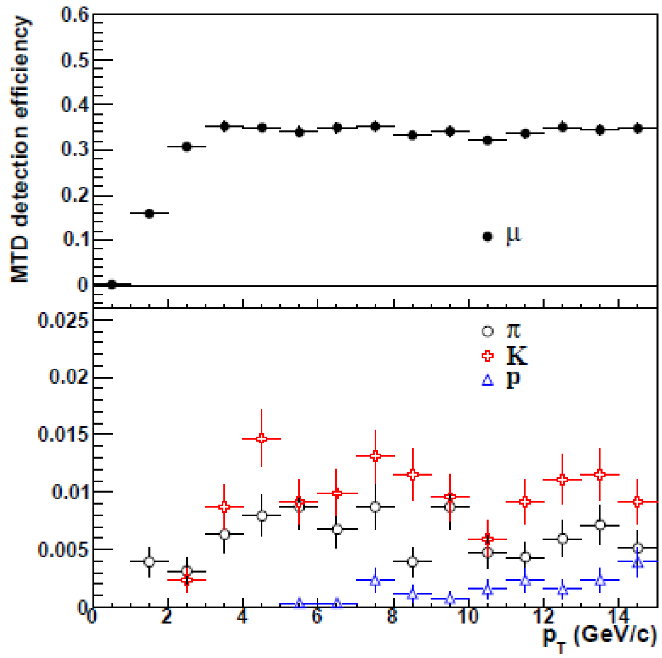

Figure 4.5: The efficiency for muons (top panel) and misidentification probabilities of pions, kaons, and protons (bottom panel) at $|y| < 0.5$

In Figure 4.5 the combined acceptance and efficiency of the MTD detectors is shown for primary muons, pions, kaons and protons. It can be seen form the figure that MTD detectors are efficienct to detect the primary muons of $p_T \gtrsim 2$ GeV/c at a level of 36% while less that 1% for overall hadrons, which clearly indicates the hadron rejection efficiency by the MTD detectors. A hadron rejection factor of 50-100 has been reported based on the simulations with an efficient trigger of around >80% for muons.

The final structure of the MTD MRPC detectors has been reported in Reference [75]. The MTD MRPC detector has been considered to be single-stack, five-gap detector having dimensions of $91.5 \times 58.0 \times 3\ cm^3$. Each MRPC has twelve $87 \times 3.8\ cm^2$ strips with 0.6 cm gaps between each strip and read out at both ends by STAR TOF electronics.A total number of 117 detectors has been installed in the full system. The arrangement of MTD trays on outside of STAR is shown in Figure 4.6.

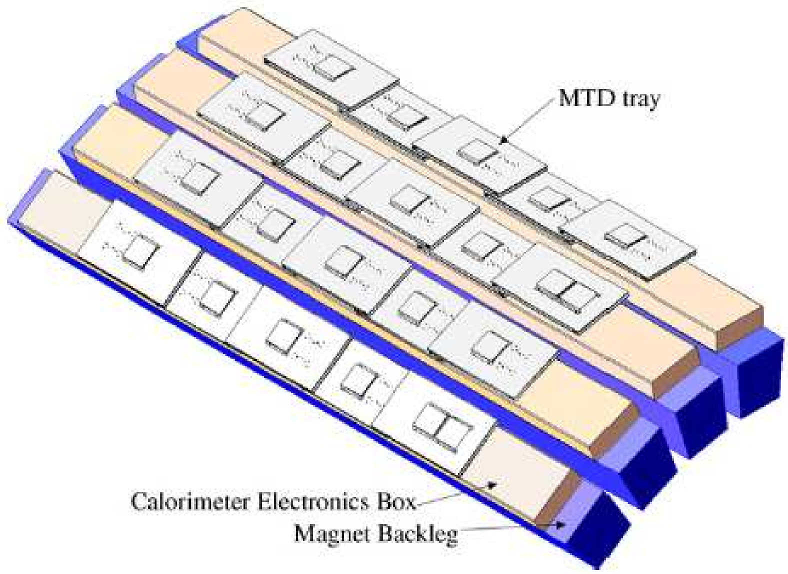

Figure 4.6: The arrangement of MTD trays on the outside of STAR

4.4.1 Physical Processes

The main aim of this section is to elaborate a few of the physical processes that led the installation of MTD in STAR.

4.4.1.1 Quarkonium Dissociation at high p_T

Suppression of the $c\bar{c}$ bound state (J/ψ meson) produced in relativistic heavy-ion collisions is a key signature of QGP formation [76]. In the measurements at $\sqrt{s_{NN}}$= 17.3 GeV at the CERN-SPS a strong suppression of J/ψ production in heavy-ion collisions has been reeported [77], although the magnitude of the suppression has been reported to decreas with increasing J/ψ p_T. At higher beam energy ($\sqrt{s_{NN}}$ = 200 GeV), the PHENIX collaboration at RHIC has measured J/ψ suppression for $p_T < 5$ GeV/c in central Au+Au and Cu+Cu collisions [78] that is similar in magnitude to that observed at the CERN-SPS. This similarity is surprising in light of the expectation that the energy density at RHIC is significantly higher at larger collision energy. It may be due to the cold nuclear absorption and the counterbalancing of larger dissociation with recombination of unassociated c and $\bar{c}$ in the medium, which are more abundant at higher energy [79].

The nuclear modification factor $R_{AA}(p_T)$ [80], defined as the ratio of the inclusive hadron yield in nuclear collisions to that in p+p collisions scaled by the underlying number of binary nucleon-nucleon collisions, measures medium-induced effects on inclusive particle production. In the absence of such effects, R_{AA} is unity for hard processes. Figure 4.7 shows

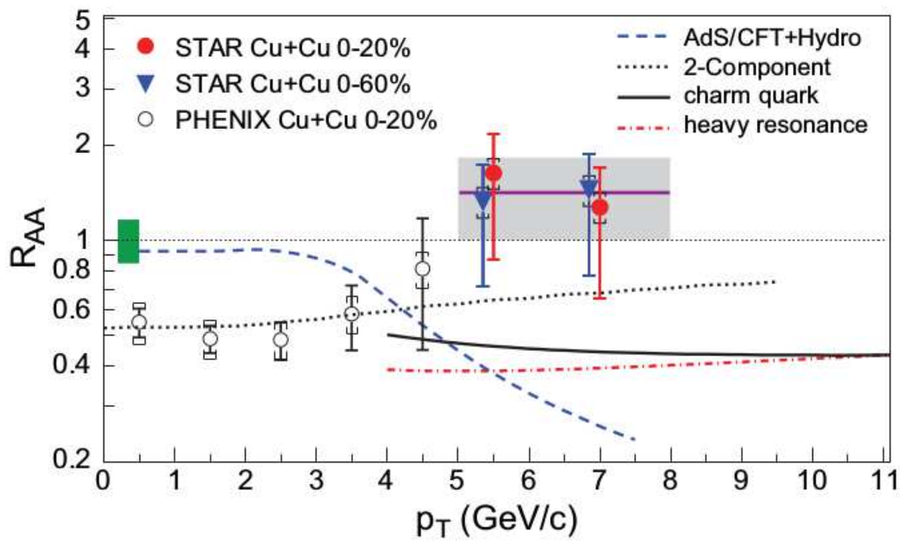

Figure 4.7: J/ψ R_{AA} vs. p_T.

R_{AA} versus p_T for J/ψas was available in 2010 run, in the 0-20% most central Cu+Cu collisions from PHENIX [81] and STAR, and the 0-60% most central Cu+Cu collisions from STAR. STAR data points have statistical (bars) and systematic (caps) uncertainties. The box about unity on the left shows R_{AA} normalization uncertainty, which is the quadrature sum of p+p normalization and binary collision scaling uncertainties. The solid line and band show the average and uncertainty of the two 0-20% data points. The average of the two STAR 0-20% data points at high-p_T is $R_{AA} = 1.4 \pm 0.4$ (stat.) $\pm$ 0.2 (syst.). Utilizing the STAR Cu+Cu and p+p data reported here and PHENIX Cu+Cu data at high-p_T [81] gives $R_{AA} = 1.1 \pm 0.3$ (stat.) $\pm$ 0.2 (syst.) for $p_T > 5$ GeV/c. Both results are consistent with unity and differ by two standard deviations from a PHENIX measurement at lower p_T ($R_{AA} = 0.52 \pm 0.05$ [81]).

Table 4.1: Quarkonium dissociation temperatures

State	J/ψ(1S)	χ_c(1P)	ψ'(2S)	γ(1S)	χ_b(1P)	γ(2S)	χ_b(2P)	γ(3S)
T_d/T_c	2.10	1.16	1.12	> 4.10	< 1.76	1.60	1.19	1.17

The p+p data presented here enable the measurement of R_{AA} at substantially higher p_T than that accessible from previous data [82]. A value of $R_{AA} < 0.6$ for $p_T > 5$ GeV/c is excluded at the 97% confidence level. The enhanced p_T range from our data allows comparison to a calculation based on AdS/CFT+hydrodynamics [83], whose prediction is excluded at the 99% confidence level. A notable conclusion from these data is that J/ψ is the only hadron measured in RHIC heavy-ion collisions that does not exhibit significant high p_T suppression.

4.4.1.2 Dissociation of Υ states

In the following Table 4.1 there is a list of the available quarkonia and their dissociation temperatures [84]. The γ states are ideal tools for the study of the effect of color screening in hot and dense QCD matter since its ground states and excited states melt at different temperatures and all of them decay to dileptons. Furthermore, since the b$\bar{b}$ cross section at RHIC energy is expected to be much smaller compared to c$\bar{c}$ cross section, the recombination contribution from QGP phase might be negligible to bottomonia production. A sufficient statistical experimental data make the Υ even a better probe for studying the color screening effect in QGP.

4.4.1.3 Physics aspects with full coverage of MTD

Having the optimized MTD coverage without impacting the operation and maintenance of the BEMC, the above-said physics cases will illustrate the capability of MTD for online triggering and improvement of momentum resolution to achieve the physics goals of the elliptic flow of measuring J/ψ and R_{AA} at high p_T and resolving the ground state Υ from its excited states. In addition, electron-muon correlations can be used to distinguish lepton pair production from heavy quark decays $(c + \bar{c} \rightarrow e + \mu(e), B \rightarrow e(\mu) + c \rightarrow e + \mu(e))$.

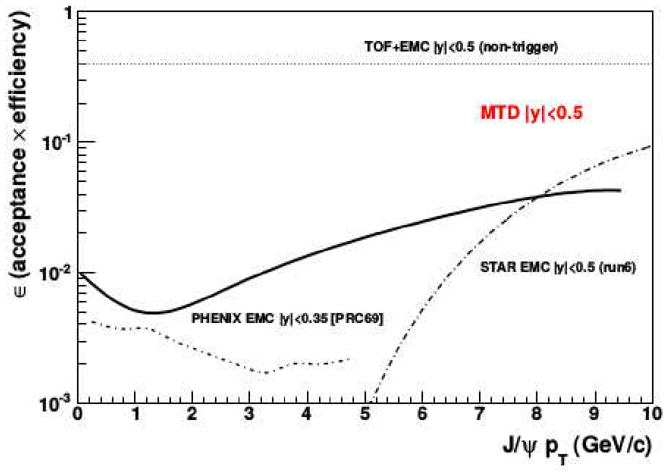

Figure 4.8: The J/ψ efficiency as a function of p_T.

In Figure 4.8 the simulated efficiencies for J/ψ at mid-rapidity at RHIC have been shown. As the trigger device, both PHENIX and STAR are able to detect the J/ψ at mid-rapidity through J/$\psi \rightarrow e^+e^-$ with electromagnetic calorimeters (EMC) and electron identifiers. However, this is limited by the capability to trigger on electrons at low momentum in STAR and relatively lower efficiency times acceptance (Υ) in PHENIX [85]. STAR can sample the total luminosity delivered at RHIC with a more selective trigger on the interesting events with J/ψ candidates by BEMC towers with a high-energy deposit. However, the efficiency is reduced significantly at low to intermediate p_T range. The MTD detecting J/$\psi \rightarrow \mu^+\mu^-$ is to have much higher trigger rejection power than the STAR BEMC and TOF combination and have a larger acceptance than the PHENIX configuration. This results in much larger J/ψ samples than the currently available RHIC experimental setups.

Shown at the top of Figure 4.9 is the J/$\psi \rightarrow \mu^+\mu^-$ with a signal-to-background ratio of 6:1 [74]. The background di-muon pairs are simulated from the inclusive muon yields obtained from studies. At the bottom of Figure 4.9 is the invariant mass distribution of di-muons from Upsilon decays simulated in the STAR geometry. Clearly, the different Upsilon states (Υ(1S), Υ(2S), and Υ(3S)) can be separated through the di-muon decay channel while Bremsstrahlung energy losses of electrons present a challenge for the separation due to the detector material, including future inner tracker upgrades at STAR.

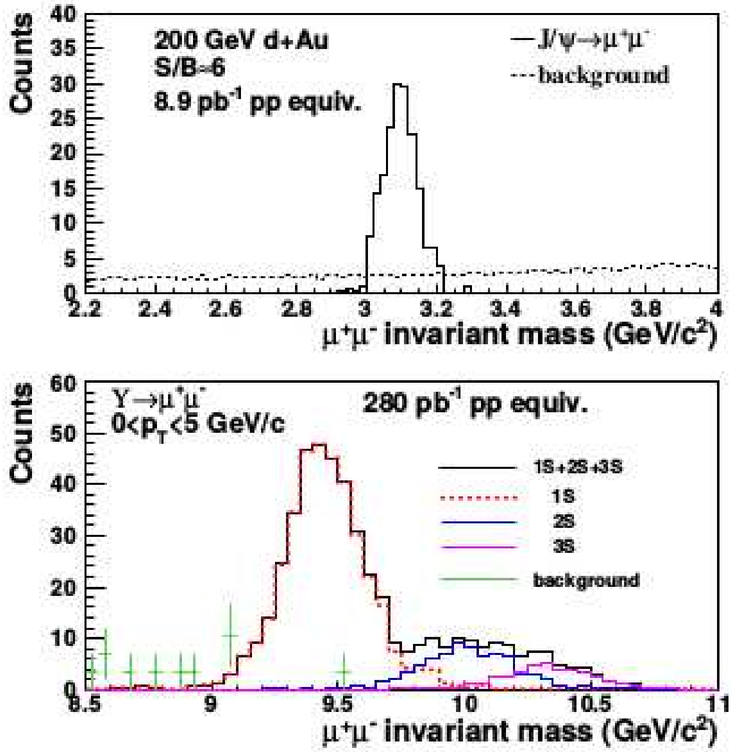

Figure 4.9: The simulated invariant mass of $\mu^+\mu^-$ distribution from j/ψ and background in d+Au collisions (top panel); the invariant mass distribution of dimuon decayed from Υ at 0< p_T <5 GeV/c (bottom panel).

4.4.2 Detector Configuration

To satisfy the physics aspects discussed in the previous section the MTD MRPC detectors have to measure time intervals using the information on the track momenta and positions determined by the TPC and projected to the MTD. For fulfilling the purpose the MTD detectors has been placed at a radius of 400 cm from the centre of the TPC where the interaction occurs. As depicted by Figure 4.10 the MTD MRPC detectors have been placed on top of the BEMC boxes outside the steel backlegs.

For maintaing the full operation of the BEMC detectors the MTD boxes have been placed on the top of the BEMC boxes. For the bottom 9 backlegs, there will be 3 trays in each backleg. For other 18 backlegs, there will be 5 trays in each backleg except 3 backlegs at 3 o'clock and

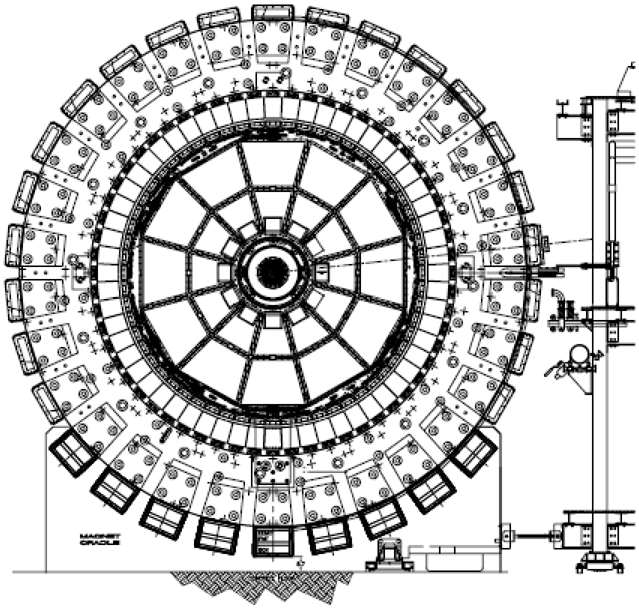

Figure 4.10: A beam's eye view of STAR. The MTD system is attached to the PMT HV boxes.

9 o'clock direction. In total, there will be 117 trays. In each tray, there will be one MRPC module. The active region of each MRPC will be 89 cm in length (along the beam direction), and 52 cm in width (azimuthally). A list of system constraints and the other reuirements can be found in Reference [74].

4.4.3 Module Structure

A schematic view of the MRPC module is shown in Figure 4.11. The module has six 250 mm wide gaps, which are defined by a stack of float glass plates separated by nylon fishing line. The inner and outer glass plates are 0.7 mm and 1.1 mm thick respectively. The volume resistivity of the glass plates is about $10^{12} \sim 10^{13}\Omega$cm. The high voltage cathode and anode are a coating of colloidal graphite paint on the external surfaces of the outer glass plates. The graphite painted electrode has a surface resistivity of the order of 5 M$\Omega/\Box$. High voltage is applied to the electrodes via 10 mm wide and 800 mm long pieces of copper tape applied to the long edges of the painted electrodes. The active area of the module is 52 cm$\times$ 90 cm. Twelve pairs of strips above and below the inner glass stack pick up the signals, which are each 3.8 cm wide and 90 cm long with 0.6 cm intervals between the strips. Mylar sheets of 0.18 mm thickness are placed between the graphite paint and the printed circuit boards with the read-out strips to electrically insulate the HV electrodes and the read-out strips. Fiberglass-reinforced honeycomb plates are used to keep the device rigid.

Such a detector system technology was fist developed by CERN ALICE group [86]. In recent years, such technology has been successfully implemented at TOF systems in both STAR and PHENIX experiments. The technology has been proved to be inexpensive, easily constructable, and capable of the necessary timing resolution.

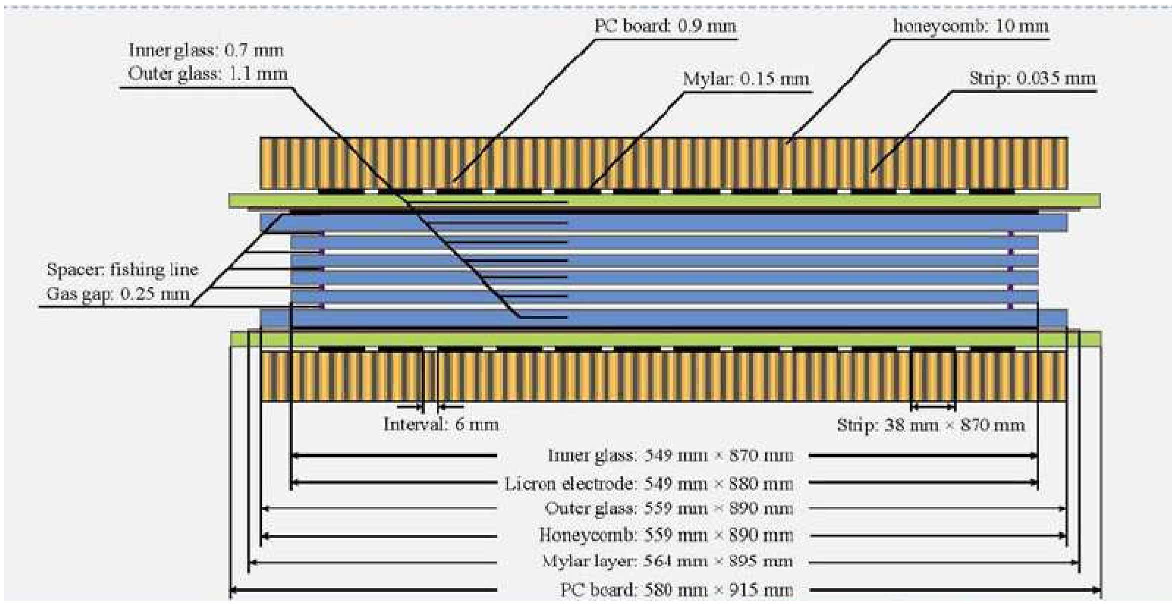

Figure 4.11: Schematic of the detector module

In Table 4.2 the details of the detector module structure is summarized.

Table 4.2: Summary of the layout of a module

HV electrode	Colloidal Graphite (Resistivity $\sim 5\mathrm{M}\omega/\square$)
Readout Strip	870 mm $\times$ 38 mm (Total Number 12)
Interval between strips	6 mm
Glass Type	Float Glass
Glass Thickness	0.7 mm (inner), 1.1 mm (outer)
Gas Gap	0.25 mm (Total Number 5)

4.4.4 Construction and Testing of the module

The job of production of 117 modules were divided among the collaboating institutes , i.e., BNL, RICE, Texas, Austin, UC Davis, UC Berkeley, Tsinghua University (China), USTC (China), VECC (India). VECC had the responsibility of building ∼10% of the modules, i.e., 12 modules in total. Details of the construction and the testing of the modules have been discussed here.

For the construction of the detector modules the inner glass plates were obtained from Tsinghua University, China and the outer glass plates were procured by Bose Institute, Kolkata. Also for maintaining proper uniform gas gaps fishing were used that were procured from GSI, Germany.

Figure 4.12 schematically shows the different steps of the fabrication of the detector modules.

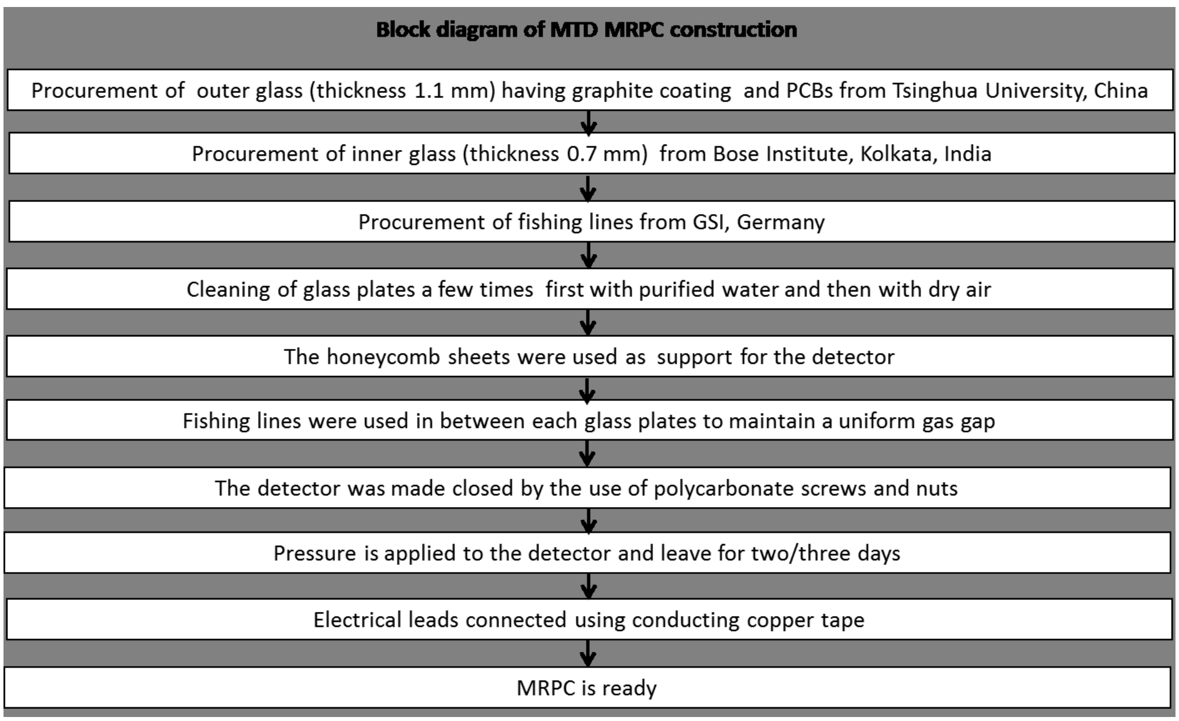

Figure 4.12: Fabrication procedures of MTD MRPC detector modules

In the left panel of Figure 4.13 shows the photograph of PCB based pick-up strips having dimension of 87 cm × 3.8 cm, whereas the right panel shows the photograph of the fishing lines implemented on a typical layer of the MTD MRPC.

Figure 4.13: Left panel: the photograph of the pick-up strips for the MTD modules; Right panel: the phtograph of the fishing lines used to maintain the constant gas gap of the modules

Figure 4.14 shows the photgraph of cross-sectional view of different layers of a typical MTD MRPC. As can be seen from the Figure 4.14, polycarbonate screws hold the fishing lines to maintain a uniform gas gap within the detector.

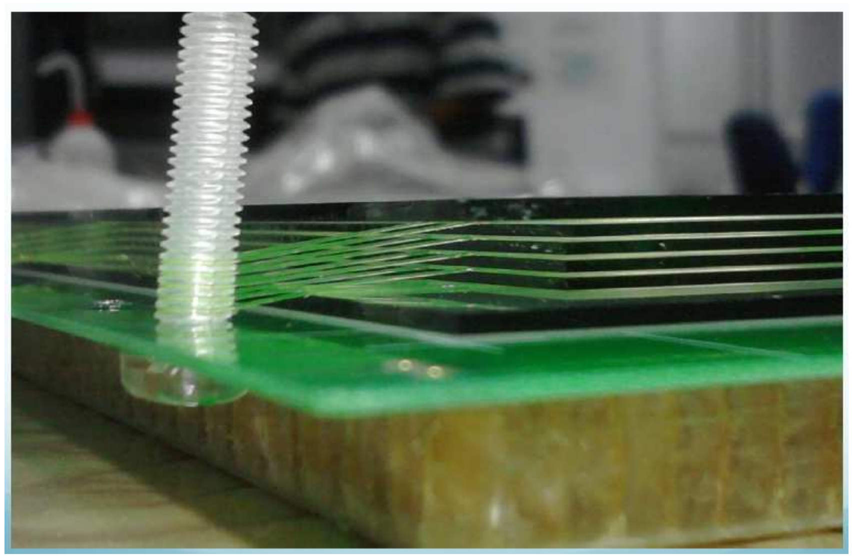

Figure 4.14: Cross-sectional view of a typical MTD MRPC detector module showing the gas gaps maintained by the fishing lines

In Figure 4.15 shows the completely assembled photograph of a MTD module after connecting the flat ribon cables with the pick-up strips. The module is put on a aluminium-made gas box, which served as a gas enclosure.

Figure 4.15: Completely assembled MTD module before the gas flow

In left panel of Figure 4.16 the gas connections applied to the MTD modules has been shown whereas at the right panel of Figure 4.16 the MFC-based gas mixing system used for the testing of the modules has been shown.

Before applying high voltage each of the modules was kept under a constant gas flow which was a mixture of Freon (R-134a) and iso-butane(C_4H_{10}) in a volumetric ratio of 95% : 5% for 48 hours. A constant gas flow rate of 20 ml/ min (20 SCCM) was maintained in each case, which implies a total of 1.3 of the total gas volume change in 48 hours. Each of the modules had been tested for claculating the leakage current through the surfaces of the electrodes. At

Figure 4.16: Left panel: The gas connection applied to the MTD molecules; Right panel: the MFC-based gas mixing system

this stage it is important to mention that some of the modules had shown high leakage current ($\sim$ 200-250 nA) while testing. The reason for such a high value of the current was found to be the humidity and the temperature of the experimental room. The problem had been solved using dehumidifier and maintaining the room temperature low. During the whole study of the MTD modules the humidity and the temprature had been maintained constant.

In Figure 4.17 the schematic representation of the Cosmic ray testing set-up has been shown. For the test, the trigger signal (3F) was defined as the coincidence from scintillator 1 (S1), scintillator 2 (S2) and the finger scintillator (FS), as shown in the Figure 4.17. A four-fold (4F) signal was defined as the coincidence from all the scintillators mentioned before along with the signal from any of the MRPC strips. The **efficiency** of the detector module was defined as the ratio between the four-fold (4F) and trigger (3F) counts at a given instance of time. In the set-up the noise rate of the individual strip was also measured. The **noise rate** discussed here was defined as the ratio of the single strip count and the product of the time for the count with the strip area,i.e., [(Single strip count)/(time in sec $\times$ 3.8 cm $\times$ 87 cm)].

In Table 4.3 the high voltage applied to different detectors in the setup along with the threshold voltages are mentioned.

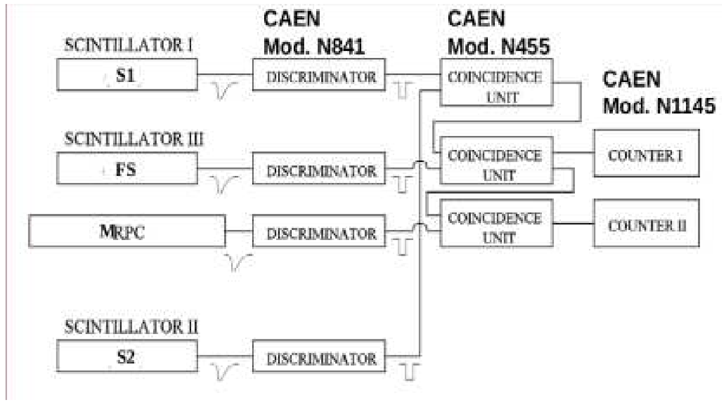

Figure 4.17: Schematic layout of the cosmic ray test setup of the MTD modules

Table 4.3: High Voltage and threshold configuration for cosmic test

Detector	HV	Threshold
Scintillator 1	-1400 V	-50 mV
Scintillator 2	-1400 V	-50 mV
Finger Scintillator	-1050 V	-50 V
MRPC		-50 mV

All the detector modules were thouroughly tested at VECC. The leakage current for all the modules were found to be within the range of 20-50 nA. Some of the modules initially showed high value of leakage current. The probable reason for the high values seemed to be the effect of humidity of the expermental room. The problem was solved by the use of a dehumidifier. Also the efficienies of the detector modules were examined and it was found that all the modules had an efficiency of 85% after using a threshold of 50 mV. Also the noise rate for the detector modules was found to be around 1 Hz/cm^2. The performances of the detector modules were as per the requirements of the STAR experiment.

After thourugh testing at VECC, the modules were sent to UT, Austin for further study before the installation to STAR. A typical study of detector module no. 9 has been shown in Figure 4.18. The left side of the Figure 4.18 shows the noise rate as obtianed for eah strip. The mean of the noise was found to be 11 Hz. The right side of Figure 4.18 shows the time over threshold (tot) plot for the detector module, which basically indicates the charege spectra. As shown in the figure, there are different peaks found in the plot. Although the exact origin of these multiple peak was not eaxtly known, it can be generated because of the dust particle within the detector or the bad fishing lines. The tot plot was used for the slewing correction of the efficiency measurement of the detector modules.

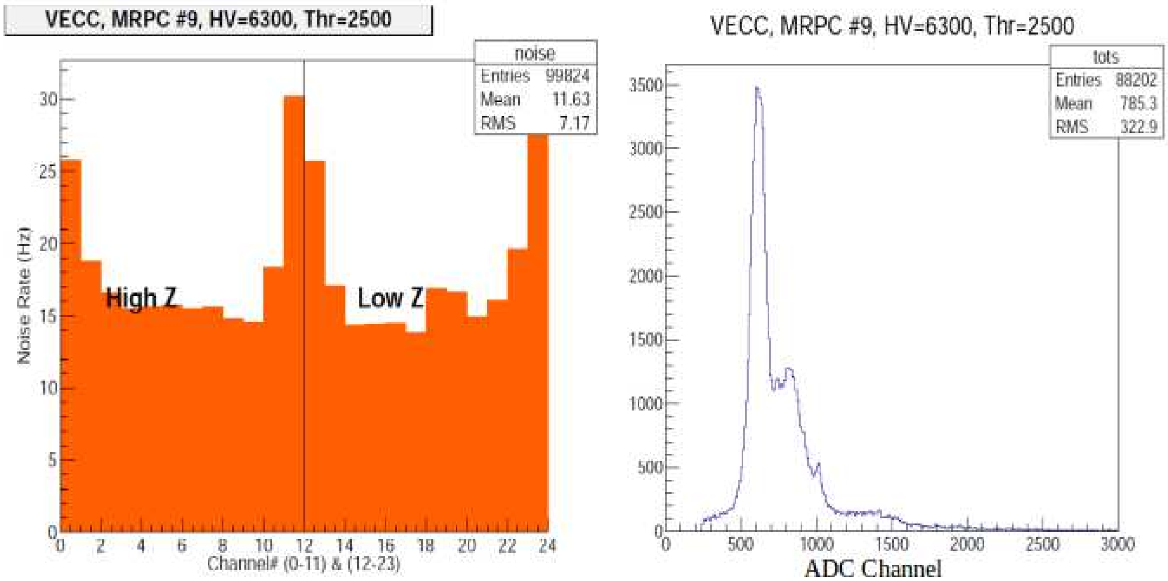

Figure 4.18: A typical test result of one of the MTD modules : Left panel - the noise rate for different pick-up channels; right panel - time over threshold plot used for slewing correction

Figure 4.19 shows the correlation plot between the different pick-up channels. One should expect to see 12 peaks on one side, correlating the two ends of each strip, and equal mirror images on the other, which is the same correlation of channels, just commuted (i.e., correlation of channels 1 and 13 should match correlation of channels 13 and 1). This plot is mainly used to find any damage of the readout channel.

All the modules were tested thoroughly at UT, Austin and were reported to work in good condition at STAR.

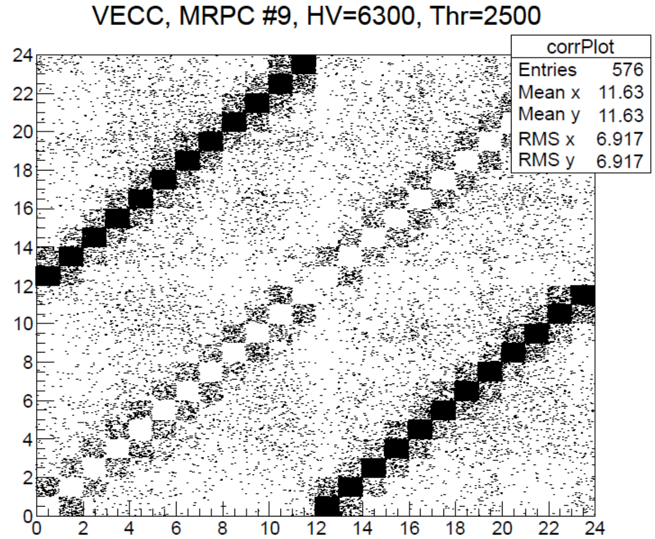

Figure 4.19: Correlation plot of diffrent pick-up strips as obtained for one of the MTD modules

4.5 Performance of MRPC in Cosmic Ray Test setup

MTD has been installed in phases with the completion in the year 2014. As MTD works in conjuction with TPC, the TPC tracks are extrapolated on to the MTD surface for the measurements of muons. We here discuss the procedure of calibration (both timeand position) of the determination of MTD hits using cosmic rays.

Figure 4.20 shows the Schematic of cosmic ray event in STAR.

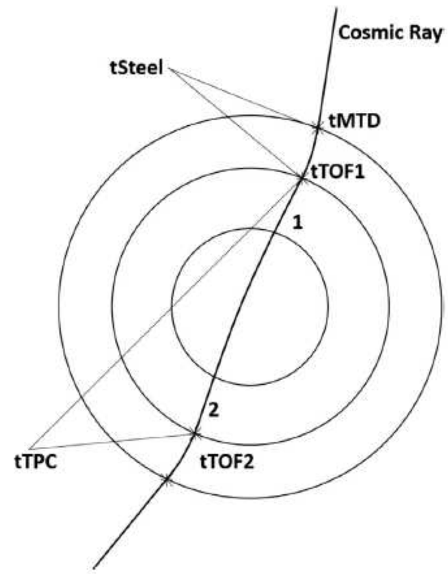

Figure 4.20: Schematic view of the cosmic test setup in STAR

As depicted by Figure 4.20 the cosmic ray crosses the MTD, return bars, BEMC, TOF and TPC detectors, producing a track in the TPC and two hits at MTD and TOF. The time measured by the two TOFs and MTD is indicted as tTOF1, tTOF2 and tMTD respectively. The time of flight between two TOFs is measured by using path length and momentum p measured by TPC and indicated as tTPC. The time of flight from the MTD and the first TOF detector is calculated by track's helix parameters, momentum p and the magnetic field used and is indicated by tSteel.

For muon identification cosmic ray muon tracks with momentum $p_T > 2$ GeV were selected. In the left of Figure 4.21, the p_T distribution of the muons is depicted, whereas in the right of Figure 4.21 the relative momentum difference Δp/p is shown. The average momentum is reported to be around 6 GeV, whereas the the average momentum resolution is reported to be around 10%.

Also the tracks reconstructed in the STAR TPC were extrapolated to the MTD radius,for the measurement of the spatial resolution of the MTD detecors in the Z direction (along the strips) and the azimuth, ϕ, direction (perpendicular to the strips). Figure 4.22 shows the spatial resolution in both the directions.

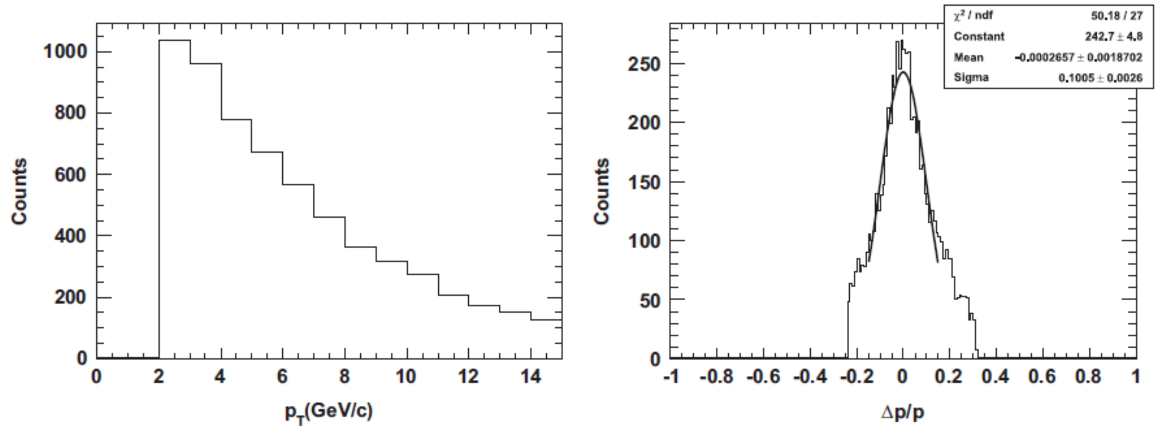

Figure 4.21: Left: The momentum distribution of cosmic ray muons for $p_T > 2$ GeV; Right: The relative momentum resolution distribution of the two tracks from one cosmic ray muon

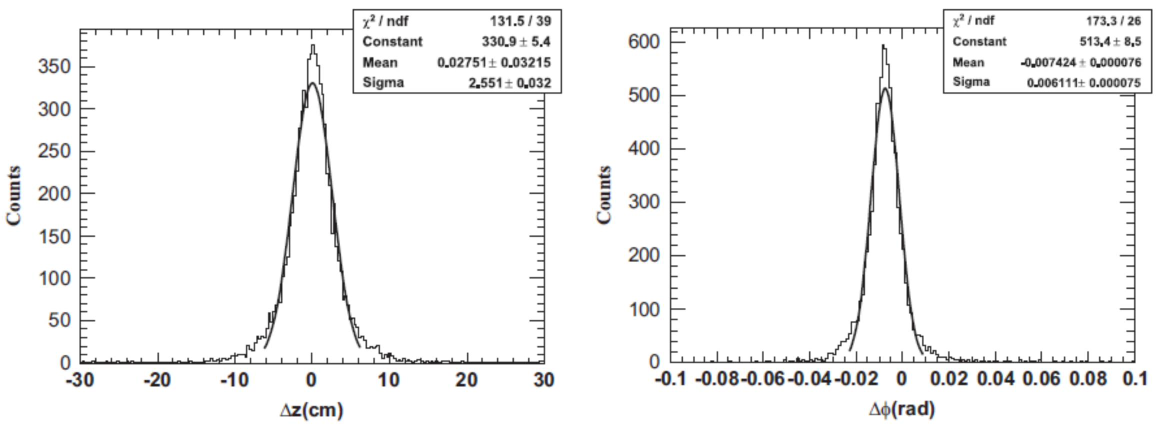

Figure 4.22: ΔZ and $\Delta\phi$ resolution for the TPC reconstructed tracks

For the measurements of the time resolutions of the detector the tracks having $\Delta Z < 6$ cm and $\Delta\phi$ <0.2 rad were selected. The times tTOF1 and tTOF2, measured by two TOF detectors were used to calculate the START time of each event. The time resolution is defined by the formula

$$\Delta T_0 = (tTOF2 - tTOF1) - tTPC$$

where (tTOF2-tTOF1) is the time of flight measured by the two TOF detectros and and tTPC is the time-of-flight that is expected for a muon with the trajectory and momentum as reconstructed in the TPC. Figure 4.23 shows the ΔT_0 distribution as measured by the detectors. The TOF single detector time resolution is reported to be [87] around 64 ps.

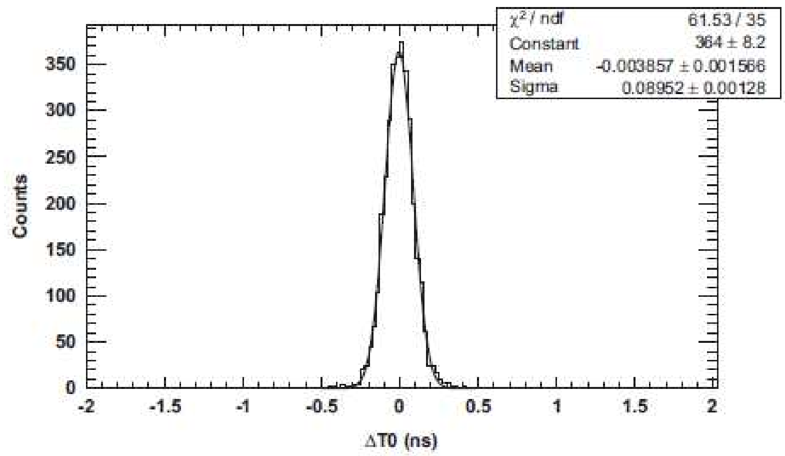

Figure 4.23: Time resolution for the TPC reconstructed tracks by MTD detectors

The final step to calculate the time resolution of the MTD detector involved the slewing correction. For the purpose, a quantity ΔT is defined as

$$\Delta T = (tTOF2 - tTPC + tTOF1)/2 - tMTD - tSteel$$

The ΔT distribution were recorded for each MRPC read-out strip seperately. A detailed procedure of calculating the timing resolution for the MTD can be found in Reference [87]. Afetr the proper slewing correction the final time resolution of the MTD detectors was reported to be 90 ps.

4.6 Summary

The time and spatial resolution of the STAR MTD system were obtained using cosmic-ray muons traversing the STAR detector. The relatively high momentum muons can be cleanly triggered upon. The detectors allow studies of the time and spatial resolutions with relatively small contributions from multiple scattering in the STAR detector materials. The MTD resolution values observed were 90ps for the timing resolution and 1-2 cm for the spatial resolution.

Chapter 5

Summary

For several decades, dedicated R&D are being performed to develop large area gaseous detectors giving good position and time resolution. Such kinds of detectors have been used for several decades in many high energy experiments like CMS, ALICE, LHC, STAR, NeuLAND all over the world.

In this thesis, works have been performed to develop a very specialized gaseous detector called Multi-Gap Resistive Plate Chamber (MRPC) which is found to be the appropriate candidate for Muon identification in the Solenoidal Tracker at RHIC(STAR) at Brookhaven National Laboratory, USA.

Apart from the high energy physics aspect, the MRPCs have been found to be a less expensive substitute for scintillator-based detectors usually used in the field of Nuclear medicine field, specially in PET.

The development along with the test results of the MRPCs for the use in Muon Telescope Detector (MTD) in STAR experiment and as a proof of principle for their uses in Time-of-Flight (TOF) PET system have been discussed in details in this thesis.

An overview of the detectors developed so far for uses in high energy and particle physics experiments is given in Chapter 1. It mainly consists of the major detector types, their behaviours and uses in different high energy physics experiments. An emphasis has been given on the discussion of the gas-based radiation detectors. A detail description of different gas ionization detectors like Geiger- M$\ddot{u}$ller counter, Proportional gas chamber, MWPC, TPC, GEM, RPC have been discussed in this chapter.

An elaborated discussion on the principle of operation and the development of MRPC have been done in chapter 2. The advantage of using MRPCs, having better time and position resolution over the conventional wide-gap and narrow-gap RPCs is also discussed in this chapter. Also the charateristic behaviour of MRPC on different parameters like temperature, pressure of the gas used and the high voltage is an important topic of this chapter. The chapter concludes by discussing uses of MRPC-based detector systems in different high energy experiments like LHCb muon system, the TOF detector in ALICE experiment, TOF detector in CBM experiment, neutron detector in NeuLAND experiment.

Chapter 3 presents an overview on the use of detectors in nuclear medicine field, specially on Positron Emission Tomography. A comparative study between different scanners used in medical field is also discussed in this chapter. The process of simulation for optimization of MRPC as a suitable TOF-PET detector has remained part of the discussion. The simulation has been performed in two stages - at the first stage GEANT4 has been used to simulate the conversion of the incident photons and secondly the electrons (positrons) obtained by photon conversion are considered to be the particles ionizing the MRPC gas. As the final step, the processes from ionization to signal generation have been implemented as another Monte Carlo (MC) procedure. For the simulation procedure a combination of lead converter, the electrode (Glass) and the gas gap of 0.25 mm were considered to form a layer. The simulation results show that a layered structure of 0.04 mm thin lead converter and 0.25 mm gas gap can be used to convert 511 keV photons such that the conversion electrons can reach the gas gap, resulting an efficiency of 30% for a system of 140 layers or above. Also the simulation predicts the intrinsic time resolution of such a structure to be around 19 ps. Apart from the simulation, the fabrication and testing of a number of MRPC modules have been discussed. Both types of electrodes , i.e., Bakelite and glass were used. A two-gap and a four-gap Bakelite-based MRPC were fabricated. The two-gap and the four-gap MRPCs were found to have an efficiency plateau of 90% at around 13.5 kV and 12.5 kV respectively. Also the time resolution (σ) of two-gap and four-gap MRPCs were found to be 2 ns and 0.85 ns respectively. Also a glass-based six gap MRPC were fabricated and tested and it was found the six-gap MRPC to have an intrinsic time resolution of 440 ps. As a feasibility study of MRPC as a probable candidate for TOF-PET imaging setup was made using ^{22}Na source capable of emitting two almost back-to-back 511 keV photons. The results discussed in the chapter clearly indicates that MRPC-based TOF-PET system is potentially an attractive alternative to the expensive scintillator-based system. The results of the feasibility study indicates that the time measured by the MRPC detector is sensitive to the change of the location of the annihilation point.

An overview on high energy heavy ion collision and QGP, followed by a brief description of the major detector components of STAR experiment has been given in chapter 4. The chapter mainly focuses on the discussion of STAR MTD - its physics motivation and its performance as a muon tracking detector in STAR. As a collaborating institute a total of 10% of the total 117 MTD modules have been fabricated at VECC. The test results at VECC include the leakage current measurement, the efficiency measurement and the noise rate measurement for individual detector modules. The modules were further tested at UT, Austin using cosmic rays and MTD electronics before installation in STAR. The procedure for the calibration of the modules and measurement of the time and position resolution using cosmic rays in STAR is also discussed.

MRPCs are being used extensively in high energy physics experiments worldwide for their excellent time and position resolution. In this thesis, simulation, production, testing and the application of MRPC in major areas, i.e., STAR muon detection and TOF-PET imaging have been discussed. The details of material characterization, module fabrication, testing procedure and results have been discussed.

It has been shown that both glass and Bakelite could be used as electrode material. However, the requirement of rate must decide the final selection of the electrode. In this work, both button spacers and fishing lines were used for maintaining the uniformity of the gas gaps in the modules. For technical constraints, the gap for button spacers is larger compared to that obtained in case of fishing lines.

As a part of the thesis work, an extensive R&D has been performed on MRPC of different sizes starting from 23 cm $\times$ 23 cm to 1 m $\times$ 0.5 m. The technical details vary with the size and the other specifications. The different MRPC detectors have been tested in two different modes of operation, i.e., streamer mode and avalanche mode using proper gas mixtures. Dedicated gas mixing systems were employed for the purpose. During the testing the lab has been maintained in an environment of relative humidity of $\sim$ 45% and temperature of $\sim$ 20^{0}C. A special gastight box made of aluminium (Al) was used to house each large MRPC for high voltage and cosmic ray testing. Even though STAR-specific Front End Electronics (FEE) were used for testing the MTD detector modules, for the testing of small MRPCs, conventional NIM and CAMAC-based electronics were used. While for running in avalanche mode, pre-amplifiers were used, for the streamer mode of operation, pre-amplifiers were not required. For small MRPC detectors, along with efficiency and time resolution measurements, the charge spectrum in avalanche mode has also been studied. The charge spectrum obtained in the experiment was found to be well described by Polya distribution.

A dedicated setup for the proof of principle of MRPC for the TOF-PET imaging system has been developed. A simulation for optimization of the experimental setup was performed and small glass-based MRPC was used to demonstrate using ^{22}Na source that the time resolution measured by the MRPC is sensitive to determine the location of the annihilation point.

Bibliography

[1] K. Arisaka, Nucl. Instrum. Methods A 442, (80), 2000

[2] K.K. Hamamatsu, Electron Tube Division, Photomultiplier Tubes: Basics and Applications, 3rd edition (2006);

[3] A. Braem et al., Nucl. Instrum. Methods A518, (574), 2004.

[4] P. Mangeot et al., Nucl. Instrum. Methods A216, (79), 1983.

[5] J.B. Birks, The Theory and Practice of Scintillation Counting, (Pergamon, London,1964).

[6] N. Akchurin et al., Nucl. Instrum. Methods A595, (359), 2008.

[7] A. Para, FERMILAB-CONF-11-519-CD; H. Wenzel et al., FERMILAB-PUB-11-531-CD-E.

[8] W. R. Leo: Techniques for Nuclear and Particle Physics Experiments, (2nd Edition, Springer-Verlag Berlin Heidelberg, 1994).

[9] LECTURES,ParticleDetectorSS12,L4,gasDetectors.pdf, garutti

[10] R. Santonico and R. Cardarelli. Development of resistive plate counters. Nucl. Instr. and Meth., 187:377380, 1981.

[11] R. Santonico and R. Cardarelli. Progress in resistive plate counters. Nucl. Instr. and Meth., A 263:2025, 1988.

[12] G. Bruno, Eur Phys. J. C 33 (2004) s1032.

[13] G. Charpak,R. Bouclier, T. Bressan,J. Favier and C. Zupancic: The use of Multiwire Proportional Counters to select and localize Charged Particles, Nuc. Instr. and Meth. 62, (262), 1968.

[14] F.E. Taylor,Nucl. Instr. and Meth., A 289,(283),1990.

[15] N. Koori et. al., Nucl. Instr. and Meth., A 307, (581), 1991.

[16] A GEM of a detector, CERN Courier, Nov 27, 1998.

[17] A COMPARISON OF THE WIDE GAP AND NARROW GAP RESISTIVE PLATE CHAMBER, E. Zeballos, et.al., CERN PRE/95-146

[18] E. Cerron Zeballos, et al., Nucl. Instr. and Meth. A 374 (1996) 132.

[19] The Wide Gap Resistive Plate Chamber, I.Crotty, E.Cerron Zeballos, J.Lamas Valverde, D. Hatzifotiadou, M.C.S.Williams and A.Zichichi, Nucl. Instr. and Meth. A 360 (1995) 512.

[20] THE MULTIGAP RESISTIVE PLATE CHAMBER, Zeballos, et. al., March 18, 1996.

[21] P. Camarri et al., Nucl. Instr. and Meth. A 409 (1998) 646.

[22] M. Abbrescia et al., Nucl. Instr. and Meth. A 359 (1995) 603.

[23] LHCb Technical Proposal, CERN/LHCC 98-4.

[24] Performance of a Multigap RPC prototype for the LHCb Muon system, Nucl. Instr. and Meth. A 456 (2000) 22-26

[25] ALICE Collaboration, Journal of Physics G: Nuclear and Particle Physics 30 (2004) 15-17

[26] A. Akindinov, et al., Nuclear Instruments and Methods in Physics Research Section A 615 (2010) 37.

[27] A. Akindinov, et al., European Physical Journal C68 (2010) 89.

[28] Letter of Intent for the CBM Experiment, Darmstadt, Germany, 2004.

[29] J. Wang et al., Nuclear Instruments and Methods in Physics Research A 661 (2012) S125S128.

[30] C. Caesar et al., Nuclear Instruments and Methods in Physics Research A 661(2012) S145S148.

[31] A. Sharma and F. Sauli, Nucl. Instr. and Meth. A 334(1993)420

[32] The MRPC-based ALICE time-of-flight detector : Status and performance, A. Alici, Nuclear Instruments and Methods in Physics Research A 706 (2013) 2932.

[33] G. Muehllehner, J.S. Karp, Phys. Med. Biol. 51 (2006) 117.

[34] MRPC-PET: A new technique for high precision time and position measurements, K. Doroud et al., Nucl. Instr. Meth. A 660, 73 (2011).

[35] J.S. Karp, snm(advancing molecular imaging and therapy), Volume 3, Issue 3

[36] A. Akindinov, et al., Nuclear Instruments and Methods A 602 (2009) 709.

[37] W.J. Llope, for the STAR Collaboration, Nuclear Instruments and Methods A 241 (2005) 306.

[38] A. Blanco, et al., Nuclear Instruments and Methods A 602 (2009) 780.

[39] A. Blanco et al., Development of large area and of position-sensitive timing RPCs, Nucl. Instrum. Meth. A 478 (2002) 170.

[40] Z. Weizheng et al., Monte Carlo Simulation of RPC-based PET with GEANT4, Chinese Phys. C 37 (2013) 010201 [arXiv:1402.4544].

[41] A. Tamborini, Time Of Flight measurement of 511 keV annihilation photons with Multigap RPCs, Dipartimento di Fisica, Universit'a di Pavia, Italy.

[42] A.Blanco et al., Perspectives for positron emission tomography with RPCs, Nucl. Instrum. Meth. A 508 (2003) 88.

[43] GEANT4 collaboration, S. Agostinelli et al., GEANT4: A Simulation toolkit, Nucl. Instrum. Meth. A 506 (2003) 250.

[44] C. Lippmann et al., Nucl. Instr. and Meth. A 602 (2009)735.

[45] W. Blum, L. Rolandi, Particle Detection with Drift Chambers, Springer, Berlin, 1993 ISBN3-540-56425-X.

[46] W. Riegler, C. Lippmann and R. Veenhof, Detector physics and simulation of resistive plate chambers, Nucl. Instrum. Meth. A 500 (2003) 144.

[47] A. Blanco et al., Development of large area and of position-sensitive timing RPCs, Nucl. Instrum. Meth. A 478 (2002) 170.

[48] S. Biswas, et al., Nucl. Instr. and Meth. A 604 (2009) 310.

[49] S. Biswas, et al., Nucl. Instr. and Meth. A 602 (2009) 784.

[50] Efficiency of RPC detectors for whole-body human TOF-PET, A. Blanco, et.al., NIM A 602 (2009) 780

[51] Y. Aoki, G. Endrodi, Z. Fodor, S. D. Katz and K. K. Szabo, Nature 443, 675 (2006).

[52] A. Barducci, R. Casalbuoni, S. De Curtis, R. Gatto and G. Pettini, Phys. Lett. B 231,463 (1989).

[53] A. Barducci, R. Casalbuoni, S. De Curtis, R. Gatto and G. Pettini, Phys. Rev. D 41, 1610 (1990).

[54] M. M. Aggarwal et al. (STAR Collaboration), arXiv:1007.2613v1 [nucl-ex].

[55] M. Anderson et al., Nucl. Instr. Meth. A 499, 659 (2003).

[56] L. Kotchenda et al., Nucl. Instrum. Meth. A 499 (2003) 703.

[57] C. Adler et al. [STAR Collaboration], Nucl. Instrum. Meth. A 499 (2003) 633.

[58] M. Shao et al., Nucl. Instr. Meth. A 558, 419 (2006).

[59] H. Bichsel, Nucl. Instr. Meth. A 562, 154 (2006).

[60] Y. Xu et al., 0807.4303.

[61] M. Anderson et al., Nucl. Instrum. Meth. A 499 (2003) 659.

[62] B. Bonner et al., Nucl. Instr. Meth. A 508, 181 (2003); M. Shao et al., Nucl. Instr. Meth. A 492, 344 (2002); J. Wu et al., Nucl. Instr. Meth. A 538, 243 (2005).

[63] J. Adams et al., Phys. Lett. B 616, 8 (2005).

[64] W.J. Llope et al., Nucl. Instrum. Meth. A 522 (2004) 252.

[65] M. Beddo et al., Nucl. Instr. Meth. A 499, 725 (2003).

[66] F. Bergsma et al., Nucl. Instr. Meth. A 499, 633 (2003).

[67] M. Beddo et al., Nucl. Instrum. Meth. A 499 (2003) 725.

[68] C. E. Allgower et al., Nucl. Instrum. Meth. A 499 (2003) 740.

[69] M. M. Aggarwal et al., Nucl. Instr. Meth. A 499, 751 (2003); M. M. Aggarwal et al., Nucl. Instr. Meth. A 488, 131 (2002).

[70] J. Adams et al., Nucl. Phys. A 757, 102 (2005).

[71] R. Rapp and J. Wambach, Adv. Nucl. Phys. 25 (2000) 1.

[72] Electromagnetic Probes at RHIC II (Working Group Report), G. David, R. Rapp and Z. Xu, Phys. Rept. 462, 176 (2008).

[73] Z. Xu, BNL LDRD project 07-007; Beam Test Experiment (T963) at FermiLab.

[74] Proposal of a Midrapidity Dimuon Program at STAR : A Novel and Compact Muon Telescope Detector.

[75] Multigap RPCs in the STAR experiment at RHIC, W.J.Llope, Nucl. Instr. Meth. A 661 (2012) S110S113.

[76] T. Matsui and H. Satz, Phys. Lett. B178, 416 (1986).

[77] M. C. Abreu et al., Phys. Lett. B499, 85 (2001).

[78] A. Adare et al., Phys. Rev. Lett. 98, 232301 (2007a).

[79] A. D. Frawley, T. Ullrich and R. Vogt, Phys. Rept. 462, 125 (2008).

[80] C. Adler et al., Phys. Rev. Lett. 89, 202301 (2002).

[81] A. Adare et al., Phys. Rev. Lett. 101, 122301 (2008).

[82] A. Adare et al., Phys. Rev. Lett. 98, 232002 (2007c).

[83] T. Gunji et al., J. Phys.G: Nucl. Part. Phys. 35, 104137 (2008).

[84] H. Satz, J. Phys. G 32, R25 (2006).

[85] S.S. Adler et al., Phys. Rev. C 69, 014901 (2004).

[86] E. Cerron Zeballos et al., Nucl. Instr. Meth. A 374, 132 (1996); M.C.S. Williams et al., Nucl. Instr. Meth. A 478, 183 (2002).

[87] C. Yang et al., Nuclear Instruments and Methods in Physics Research A 762 (2014) 16.